

# Measurement of the inclusive $ep$ scattering cross section at low $Q^2$ and $x$ at HERA

The H1 Collaboration

F.D. Aaron<sup>6,i</sup>, C. Alexa<sup>6</sup>, V. Andreev<sup>26</sup>, B. Antunovic<sup>12</sup>, S. Aplin<sup>12</sup>, A. Asmone<sup>34</sup>, A. Astvatsatourov<sup>4,5</sup>, S. Backovic<sup>31</sup>, A. Baghdasaryan<sup>39</sup>, E. Barrelet<sup>30</sup>, W. Bartel<sup>12</sup>, K. Begzsuren<sup>36</sup>, O. Behnke<sup>15</sup>, O. Behrendt<sup>9</sup>, A. Belousov<sup>26</sup>, J.C. Bizot<sup>28</sup>, V. Boudry<sup>29</sup>, I. Bozovic-Jelisavcic<sup>2</sup>, J. Bracinik<sup>3</sup>, G. Brandt<sup>12</sup>, M. Brinkmann<sup>12</sup>, V. Brisson<sup>28</sup>, D. Bruncko<sup>17</sup>, A. Bunyatyan<sup>14,39</sup>, G. Buschhorn<sup>27</sup>, L. Bystritskaya<sup>25</sup>, A.J. Campbell<sup>12</sup>, K.B. Cantun Avila<sup>23</sup>, F. Cassol-Brunner<sup>22</sup>, K. Cerny<sup>33</sup>, V. Cerny<sup>17,g</sup>, V. Chekelian<sup>27</sup>, A. Cholewa<sup>12</sup>, J.G. Contreras<sup>23</sup>, J.A. Coughlan<sup>7</sup>, G. Cozzika<sup>11</sup>, J. Cvach<sup>32</sup>, J.B. Dainton<sup>19</sup>, K. Daum<sup>38,c</sup>, M. Deák<sup>12</sup>, Y. de Boer<sup>12</sup>, B. Delcourt<sup>28</sup>, M. Del Degan<sup>41</sup>, J. Delvax<sup>4,5</sup>, A. De Roeck<sup>12,e</sup>, E.A. De Wolf<sup>4,5</sup>, C. Diaconu<sup>22</sup>, V. Dodonov<sup>14</sup>, A. Dossanov<sup>27</sup>, A. Dubak<sup>31,f</sup>, G. Eckerlin<sup>12</sup>, D. Eckstein<sup>40</sup>, V. Efremenko<sup>25</sup>, S. Egli<sup>37</sup>, A. Eliseev<sup>26</sup>, E. Elsen<sup>12</sup>, A. Falkiewicz<sup>8</sup>, P.J.W. Faulkner<sup>3</sup>, L. Favart<sup>4,5</sup>, A. Fedotov<sup>25</sup>, R. Felst<sup>12</sup>, J. Feltse<sup>11,h</sup>, J. Ferencei<sup>17</sup>, D.-J. Fischer<sup>12</sup>, M. Fleischer<sup>12</sup>, A. Fomenko<sup>26</sup>, E. Gabathuler<sup>19</sup>, J. Gayler<sup>12</sup>, S. Ghazaryan<sup>39</sup>, A. Glazov<sup>12</sup>, I. Glushkov<sup>40</sup>, L. Goerlich<sup>8</sup>, N. Gogitidze<sup>26</sup>, M. Gouzevitch<sup>29</sup>, C. Grab<sup>41</sup>, T. Greenshaw<sup>19</sup>, B.R. Grell<sup>12</sup>, G. Grindhammer<sup>27</sup>, S. Habib<sup>13,j</sup>, D. Haidt<sup>12</sup>, M. Hansson<sup>21</sup>, C. Helebrant<sup>12</sup>, R.C.W. Henderson<sup>18</sup>, E. Hennekemper<sup>16</sup>, H. Henschel<sup>40</sup>, M. Herbst<sup>16</sup>, G. Herrera<sup>24</sup>, M. Hildebrandt<sup>37</sup>, K.H. Hiller<sup>40</sup>, D. Hoffmann<sup>22</sup>, R. Horisberger<sup>37</sup>, T. Hreus<sup>4,5,d</sup>, M. Jacquet<sup>28</sup>, M.E. Janssen<sup>12</sup>, X. Janssen<sup>4,5</sup>, V. Jemanov<sup>13</sup>, L. Jönsson<sup>21</sup>, A.W. Jung<sup>16</sup>, H. Jung<sup>12</sup>, M. Kapichine<sup>10</sup>, J. Katzy<sup>12</sup>, I.R. Kenyon<sup>3</sup>, C. Kiesling<sup>27</sup>, M. Klein<sup>19</sup>, C. Kleinwort<sup>12</sup>, T. Kluge<sup>19</sup>, A. Knutsson<sup>12</sup>, R. Kogler<sup>27</sup>, V. Korbelt<sup>12</sup>, P. Kostka<sup>40</sup>, M. Kraemer<sup>12</sup>, K. Krastev<sup>12</sup>, J. Kretschmar<sup>19</sup>, A. Kropivnitskaya<sup>25</sup>, K. Krüger<sup>16</sup>, K. Kutak<sup>12</sup>, M.P.J. Landon<sup>20</sup>, W. Lange<sup>40</sup>, G. Laštovička-Medin<sup>31</sup>, P. Laycock<sup>19</sup>, T. Laštovička<sup>40</sup>, A. Lebedev<sup>26</sup>, G. Leibenguth<sup>41</sup>, V. Lendermann<sup>16</sup>, S. Levonian<sup>12</sup>, G. Li<sup>28</sup>, K. Lipka<sup>13</sup>, A. Liptaj<sup>27</sup>, B. List<sup>13</sup>, J. List<sup>12</sup>, E. Lobodzinska<sup>40</sup>, N. Loktionova<sup>26</sup>, R. Lopez-Fernandez<sup>24</sup>, V. Lubimov<sup>25</sup>, L. Lytkin<sup>14</sup>, A. Makankine<sup>10</sup>, E. Malinovski<sup>26</sup>, P. Marage<sup>4,5</sup>, Ll. Marti<sup>12</sup>, H.-U. Martyn<sup>1</sup>, S.J. Maxfield<sup>19</sup>, A. Mehta<sup>19</sup>, K. Meier<sup>16</sup>, A.B. Meyer<sup>12</sup>, H. Meyer<sup>12</sup>, H. Meyer<sup>38</sup>, J. Meyer<sup>12</sup>, V. Michels<sup>12</sup>, S. Mikocki<sup>8</sup>, I. Milcewicz-Mika<sup>8</sup>, F. Moreau<sup>29</sup>, A. Morozov<sup>10</sup>, J.V. Morris<sup>7</sup>, M.U. Mozer<sup>4,5</sup>, M. Mudrinic<sup>2</sup>, K. Müller<sup>42</sup>, P. Murín<sup>17,d</sup>, B. Naroska<sup>13,i</sup>, Th. Naumann<sup>40</sup>, P.R. Newman<sup>3</sup>, C. Niebuhr<sup>12</sup>, A. Nikiforov<sup>12</sup>, G. Nowak<sup>8</sup>, K. Nowak<sup>42</sup>, M. Nozicka<sup>12</sup>, B. Olivier<sup>27</sup>, J.E. Olsson<sup>12</sup>, S. Osman<sup>21</sup>, D. Ozerov<sup>25</sup>, V. Palichik<sup>10</sup>, I. Panagoulas<sup>12,b,x</sup>, M. Pandurovic<sup>2</sup>, Th. Papadopoulou<sup>12,b,x</sup>, C. Pascaud<sup>28</sup>, G.D. Patel<sup>19</sup>, O. Pejchal<sup>33</sup>, E. Perez<sup>11,e</sup>, A. Petrukhin<sup>25</sup>, I. Picuric<sup>31</sup>, S. Piec<sup>40</sup>, D. Pitzl<sup>12</sup>, R. Plačákytė<sup>12</sup>, R. Polifka<sup>33</sup>, B. Povh<sup>14</sup>, T. Preda<sup>6</sup>, V. Radescu<sup>12</sup>, A.J. Rahmat<sup>19</sup>, N. Raicevic<sup>31</sup>, A. Raspigareza<sup>27</sup>, T. Ravdandorj<sup>36</sup>, P. Reimer<sup>32</sup>, E. Rizvi<sup>20</sup>, P. Robmann<sup>42</sup>, B. Roland<sup>4,5</sup>, R. Roosen<sup>4,5</sup>, A. Rostovtsev<sup>25</sup>, M. Rotaru<sup>6</sup>, J.E. Ruiz Tabasco<sup>23</sup>, Z. Rurikova<sup>12</sup>, S. Rusakov<sup>26</sup>, D. Šálek<sup>33</sup>, D.P.C. Sankey<sup>7</sup>, M. Sauter<sup>41</sup>, E. Sauvan<sup>22</sup>, S. Schmitt<sup>12,a</sup>, C. Schmitz<sup>42</sup>, L. Schoeffel<sup>11</sup>, A. Schöning<sup>12,42</sup>, H.-C. Schultz-Coulon<sup>16</sup>, F. Sefkow<sup>12</sup>, R.N. Shaw-West<sup>3</sup>, I. Sheviakov<sup>26</sup>, L.N. Shtarkov<sup>26</sup>, S. Shushkevich<sup>27</sup>, T. Sloan<sup>18</sup>, I. Smiljanic<sup>2</sup>, Y. Soloviev<sup>26</sup>, P. Sopicki<sup>8</sup>, D. South<sup>9</sup>, V. Spaskov<sup>10</sup>, A. Specka<sup>29</sup>, Z. Staykova<sup>12</sup>, M. Steder<sup>12</sup>, B. Stella<sup>34</sup>, G. Stoicea<sup>6</sup>, U. Straumann<sup>42</sup>, D. Sunar<sup>4,5</sup>, T. Sykora<sup>4,5</sup>, V. Tchoulakov<sup>10</sup>, G. Thompson<sup>20</sup>, P.D. Thompson<sup>3</sup>, T. Toll<sup>12</sup>, F. Tomasz<sup>17</sup>, T.H. Tran<sup>28</sup>, D. Traynor<sup>20</sup>, T.N. Trinh<sup>22</sup>, P. Truöl<sup>42</sup>, I. Tsakov<sup>35</sup>, B. Tseepeldorj<sup>36,k</sup>, J. Turnau<sup>8</sup>, K. Urban<sup>16</sup>, A. Valkárová<sup>33</sup>, C. Vallée<sup>22</sup>, P. Van Mechelen<sup>4,5</sup>, A. Vargas Trevino<sup>12</sup>, Y. Vazdik<sup>26</sup>, S. Vinokurova<sup>12</sup>, V. Volchinski<sup>39</sup>, M. von den Driesch<sup>12</sup>, D. Wegener<sup>9</sup>, Ch. Wissing<sup>12</sup>, E. Wunsch<sup>12</sup>, J. Žáček<sup>33</sup>, J. Zálešák<sup>32</sup>, Z. Zhang<sup>28</sup>, A. Zhokin<sup>25</sup>, T. Zimmermann<sup>41</sup>, H. Zohrabyan<sup>39</sup>, F. Zomer<sup>28</sup>

<sup>1</sup>I. Physikalisches Institut der RWTH, Aachen, Germany<sup>m</sup>

<sup>2</sup>Vinca Institute of Nuclear Sciences, Belgrade, Serbia

<sup>3</sup>School of Physics and Astronomy, University of Birmingham, Birmingham, UK<sup>n</sup>

<sup>4</sup>Inter-University Institute for High Energies ULB-VUB, Brussels, Belgium

<sup>5</sup>Universiteit Antwerpen, Antwerpen, Belgium<sup>o</sup>

<sup>6</sup>National Institute for Physics and Nuclear Engineering (NIPNE), Bucharest, Romania

<sup>7</sup>Rutherford Appleton Laboratory, Chilton, Didcot, UK<sup>n</sup>

<sup>8</sup>Institute for Nuclear Physics, Cracow, Poland<sup>p</sup>

<sup>9</sup>Institut für Physik, TU Dortmund, Dortmund, Germany<sup>m</sup>

- <sup>10</sup>Joint Institute for Nuclear Research, Dubna, Russia  
<sup>11</sup>CEA, DSM/Irfu, CE-Saclay, Gif-sur-Yvette, France  
<sup>12</sup>DESY, Hamburg, Germany  
<sup>13</sup>Institut für Experimentalphysik, Universität Hamburg, Hamburg, Germany<sup>m</sup>  
<sup>14</sup>Max-Planck-Institut für Kernphysik, Heidelberg, Germany  
<sup>15</sup>Physikalisches Institut, Universität Heidelberg, Heidelberg, Germany<sup>m</sup>  
<sup>16</sup>Kirchhoff-Institut für Physik, Universität Heidelberg, Heidelberg, Germany<sup>m</sup>  
<sup>17</sup>Institute of Experimental Physics, Slovak Academy of Sciences, Košice, Slovak Republic<sup>f</sup>  
<sup>18</sup>Department of Physics, University of Lancaster, Lancaster, UK<sup>n</sup>  
<sup>19</sup>Department of Physics, University of Liverpool, Liverpool, UK<sup>n</sup>  
<sup>20</sup>Queen Mary and Westfield College, London, UK<sup>n</sup>  
<sup>21</sup>Physics Department, University of Lund, Lund, Sweden<sup>s</sup>  
<sup>22</sup>CPPM, CNRS/IN2P3, Univ. Mediterranee, Marseille, France  
<sup>23</sup>Departamento de Física Aplicada, CINVESTAV, Mérida, Yucatán, México<sup>v</sup>  
<sup>24</sup>Departamento de Física, CINVESTAV, Mérida, México<sup>v</sup>  
<sup>25</sup>Institute for Theoretical and Experimental Physics, Moscow, Russia<sup>w</sup>  
<sup>26</sup>Lebedev Physical Institute, Moscow, Russia<sup>q</sup>  
<sup>27</sup>Max-Planck-Institut für Physik, München, Germany  
<sup>28</sup>LAL, Univ Paris-Sud, CNRS/IN2P3, Orsay, France  
<sup>29</sup>LLR, Ecole Polytechnique, IN2P3-CNRS, Palaiseau, France  
<sup>30</sup>LPNHE, Universités Paris VI and VII, IN2P3-CNRS, Paris, France  
<sup>31</sup>Faculty of Science, University of Montenegro, Podgorica, Montenegro<sup>q</sup>  
<sup>32</sup>Institute of Physics, Academy of Sciences of the Czech Republic, Praha, Czech Republic<sup>t</sup>  
<sup>33</sup>Faculty of Mathematics and Physics, Charles University, Praha, Czech Republic<sup>t</sup>  
<sup>34</sup>Dipartimento di Fisica, Università di Roma Tre and INFN Roma 3, Roma, Italy  
<sup>35</sup>Institute for Nuclear Research and Nuclear Energy, Sofia, Bulgaria<sup>q</sup>  
<sup>36</sup>Institute of Physics and Technology of the Mongolian Academy of Sciences, Ulaanbaatar, Mongolia  
<sup>37</sup>Paul Scherrer Institut, Villigen, Switzerland  
<sup>38</sup>Fachbereich C, Universität Wuppertal, Wuppertal, Germany  
<sup>39</sup>Yerevan Physics Institute, Yerevan, Armenia  
<sup>40</sup>DESY, Zeuthen, Germany  
<sup>41</sup>Institut für Teilchenphysik, ETH, Zürich, Switzerland<sup>u</sup>  
<sup>42</sup>Physik-Institut der Universität Zürich, Zürich, Switzerland<sup>u</sup>

Received: 7 April 2009 / Revised: 20 July 2009 / Published online: 12 September 2009  
 © Springer-Verlag / Società Italiana di Fisica 2009

<sup>a</sup>e-mail: [sschmitt@mail.desy.de](mailto:sschmitt@mail.desy.de)

<sup>b</sup>Also at Physics Department, National Technical University, Zografou Campus, 15773 Athens, Greece.

<sup>c</sup>Also at Rechenzentrum, Universität Wuppertal, Wuppertal, Germany.

<sup>d</sup>Also at University of P.J. Šafárik, Košice, Slovak Republic.

<sup>e</sup>Also at CERN, Geneva, Switzerland.

<sup>f</sup>Also at Max-Planck-Institut für Physik, München, Germany.

<sup>g</sup>Also at Comenius University, Bratislava, Slovak Republic.

<sup>h</sup>Also at DESY and University Hamburg, Helmholtz Humboldt Research Award.

<sup>i</sup>Also at Faculty of Physics, University of Bucharest, Bucharest, Romania.

<sup>j</sup>Supported by a scholarship of the World Laboratory Björn Wiik Research Project.

<sup>k</sup>Also at Ulaanbaatar University, Ulaanbaatar, Mongolia.

<sup>l</sup>Deceased.

<sup>m</sup>Supported by the Bundesministerium für Bildung und Forschung, FRG, under contract numbers 05 H1 1GUA /1, 05 H1 1PAA /1, 05 H1 1PAB /9, 05 H1 1PEA /6, 05 H1 1VHA /7 and 05 H1 1VHB /5.

<sup>n</sup>Supported by the UK Science and Technology Facilities Council, and formerly by the UK Particle Physics and Astronomy Research Council.

**Abstract** A measurement of the inclusive  $ep$  scattering cross section is presented in the region of low momentum transfers,  $0.2 \text{ GeV}^2 \leq Q^2 \leq 12 \text{ GeV}^2$ , and low Bjorken  $x$ ,  $5 \cdot 10^{-6} \leq x \leq 0.02$ . The result is based on two data sets collected in dedicated runs by the H1 Collaboration at HERA at

<sup>o</sup>Supported by FNRS-FWO-Vlaanderen, IISN-IKW and IWT and by Interuniversity Attraction Poles Programme, Belgian Science Policy.

<sup>p</sup>Partially Supported by Polish Ministry of Science and Higher Education, grant PBS/DESY/70/2006.

<sup>q</sup>Supported by the Deutsche Forschungsgemeinschaft.

<sup>r</sup>Supported by VEGA SR grant no. 2/7062/ 27.

<sup>s</sup>Supported by the Swedish Natural Science Research Council.

<sup>t</sup>Supported by the Ministry of Education of the Czech Republic under the projects LC527, INGO-1P05LA259 and MSM0021620859.

<sup>u</sup>Supported by the Swiss National Science Foundation.

<sup>v</sup>Supported by CONACYT, México, grant 48778-F.

<sup>w</sup>Russian Foundation for Basic Research (RFBR), grant no 1329.2008.2.

<sup>x</sup>Project co-funded by the European Social Fund (75%) and National Resources (25%)—(EPEAEK II)—PYTHAGORAS II.

beam energies of 27.6 GeV and 920 GeV for positrons and protons, respectively. A combination with data previously published by H1 leads to a cross section measurement of a few percent accuracy. A kinematic reconstruction method exploiting radiative  $ep$  events extends the measurement to lower  $Q^2$  and larger  $x$ . The data are compared with theoretical models which apply to the transition region from photo-production to deep inelastic scattering.

## 1 Introduction

Deep inelastic lepton-hadron scattering (DIS) is pivotal for the understanding of the structure of the nucleon and of the dynamics of parton interactions. Since the discovery of Bjorken scaling [1] and its violation [2] at fixed target experiments, DIS measurements have made essential contributions to the development of the theory of strong interactions, Quantum Chromodynamics (QCD). Major progress in the exploration of strong interactions has been achieved at the electron<sup>1</sup>-proton collider HERA, operating at the energy frontier. Measurements performed at HERA are essential for predictions of the physics at the forthcoming proton-proton collider, the Large Hadron Collider (LHC).

The high centre-of-mass energy of the  $ep$  scattering at HERA leads to a wide kinematic range extending to large values of the modulus of the four-momentum transfer squared, denoted  $Q^2$ , and to very small values of the Bjorken  $x$  variable. At the HERA beam energies of  $E_e = 27.6$  GeV for the electron and  $E_p = 920$  GeV for the proton, Bjorken  $x$  values as small as  $10^{-4}$  ( $10^{-6}$ ) are accessible for  $Q^2$  of  $10 \text{ GeV}^2$  ( $0.1 \text{ GeV}^2$ ).

A salient feature of the structure function  $F_2(x, Q^2)$ , discovered by the H1 [3] and ZEUS [4] collaborations with the very first HERA data, is its strong rise for  $x \rightarrow 0$ . In terms of parton distribution functions, this can be directly interpreted as a strong rise of the sea quark density towards small  $x$ . Similarly the increase of  $F_2(x, Q^2)$  with  $Q^2$  at fixed small  $x$  reveals a strongly rising behaviour of the gluon density towards low  $x$ . This is obtained in perturbative QCD (pQCD) analyses of DIS data [5–8] using the derivative  $\partial F_2 / \partial \ln Q^2$ , which is related to the gluon and quark densities as prescribed by the DGLAP evolution equations [9–13].

The DGLAP approach, in which only  $\alpha_s \ln Q^2$  terms are summed, may not apply at lowest  $x$  values as terms involving powers of  $\alpha_s \ln(1/x)$  become large. The parton dynamics at low  $x$  may be better approximated by different evolution equations, such as BFKL [14–16], CCFM [17–20] or non-linear equations [21–28]. The non-linear effects, arising

due to the large gluon density and corresponding for example to gluon-gluon recombination, could tame the rise of  $F_2$  at low  $x$ . Further clarification of low  $x$  parton dynamics requires data of the highest precision, in a wide range of  $x$  and  $Q^2$ .

For  $Q^2 \lesssim 2 \text{ GeV}^2$ , as the strong coupling constant  $\alpha_s(Q^2)$  increases, the higher order corrections to the perturbative expansion become large and lead to the breakdown of the pQCD calculations. Measurements at low  $Q^2$  and low  $x$  thus probe this transition in which quarks and gluons cease to be relevant degrees of freedom. This onset of soft hadron physics is described by phenomenological, often QCD-inspired models (see [29] for a review).

An attractive view of virtual photon-proton scattering has been developed with the colour dipole model [30]. It originated from the observation that in the proton rest frame, at low  $x$  the photon may fluctuate into a quark-antiquark pair with a lifetime  $\propto 1/x$ , long before the interaction with the proton [31, 32]. Therefore the cross sections can be expressed as a product of the square of the wavefunction of the  $q\bar{q}$  pair with a universal dipole-proton cross section. Another phenomenological model, used here, describes  $F_2(x, Q^2)$  based on the idea of self-similarity of the proton substructure at small  $x$  [33].

Access to the smallest  $x$  implies an extension of the measurements to high values of the inelasticity  $y$  where the cross section becomes sensitive to the longitudinal structure function  $F_L(x, Q^2)$ . This function completes the description of inclusive virtual photon-proton scattering, which involves transverse and longitudinal photon polarisation states. In the naive quark-parton model (QPM),  $F_L$  is zero, while in QCD it provides independent information [34] on the gluon distribution and may become correspondingly large at low  $x$ .

This paper presents new measurements of the inclusive  $ep$  cross section in the range  $0.2 \leq Q^2 \leq 12 \text{ GeV}^2$  and  $5 \cdot 10^{-6} \leq x \leq 0.02$ . The data were collected with the H1 detector in two  $e^+p$  running periods with dedicated settings of the inclusive electron triggers. One data set (termed nominal vertex, “NVX”) was collected in the year 1999 and corresponds to an integrated luminosity of  $2.1 \text{ pb}^{-1}$ . The other was collected in the year 2000, with the interaction region shifted along the proton beam direction by 70 cm (termed shifted vertex, “SVX”), and corresponds to  $505 \text{ nb}^{-1}$ .

Shifting the interaction region allows detection of the scattered electron at larger polar angles<sup>2</sup> which otherwise cannot be accessed in the main H1 apparatus and thus provides acceptance in the region  $Q^2 \lesssim 2 \text{ GeV}^2$ . In comparison to the previous H1 measurement with a shifted vertex [35],

<sup>1</sup>Unless explicitly stated, the generic name “electron” is used throughout this paper to denote both electron and positron.

<sup>2</sup>In the H1 coordinate system the  $z$  axis points along the outgoing proton beam direction termed forward direction. Therefore large electron polar angles  $\theta_e$  close to  $180^\circ$  correspond to very small angles with respect to the incoming electron direction. The coordinate system is right-handed. The  $x$  ( $y$ ) axis is directed horizontally (vertically).

an increased precision is reached using the higher luminosity of the new data and employing, in addition to the previous backward instrumentation of the H1 detector, an upgraded Backward Silicon Tracker (BST). The vertex reconstruction using the electron track in the BST allows the kinematic range to be extended at low  $Q^2$  and low  $y$ .

The measurement region is further extended towards lower  $Q^2$  and higher  $x$  values by exploiting events with hard photons emitted collinearly to the electron beam (Initial State Radiation or ISR). Such events are treated as  $ep$  events at an effectively reduced centre-of-mass energy. Unlike in the previous H1 ISR analysis [36], the emitted photons are not explicitly detected, but the missing momentum is determined using momentum conservation. For this method the BST charged particle validation of the scattered electron is important to reduce the physics background from photoproduction events, in which the scattered electron escapes undetected in the electron beam direction.

The measurement presented here is combined with previously published data [35, 37] taken at  $E_p = 820$  GeV in the region  $Q^2 \geq 1.5$  GeV<sup>2</sup> (NVX97) and in the region  $Q^2 \geq 0.35$  GeV<sup>2</sup> employing a shifted vertex technique (SVX95). The data sets are combined taking into account their systematic error correlations. The resulting accuracy reaches two percent precision in the bulk region of the measurement providing the most precise measurement in this kinematic domain.

Data on  $F_2$  extending to low  $Q^2$  were published by the ZEUS Collaboration using a detector mounted near the beam pipe [38]. For  $Q^2 \gtrsim 2$  GeV<sup>2</sup>, ZEUS data [39] from the 820 GeV operation of HERA are also available.

The paper is organised as follows: In Sect. 2 basic definitions are given. In Sect. 3 models are introduced which are subsequently compared to the data. In Sect. 4 the methods to determine the DIS event kinematics and the principle of the cross section measurement are presented. In Sect. 5 the H1 apparatus is described with emphasis on the components of key importance for the present measurement. Section 6 presents the event selection and reconstruction, followed by Sect. 7 on the Monte Carlo (MC) simulation of events. In Sect. 8 a detailed account of the analysis techniques and uncertainties of the measurement is given, and the cross sections obtained from the 1999 and 2000 data are presented. In Sect. 9 the data averaging method and the combination of the new data with the previous H1 data taken at  $E_p = 820$  GeV are presented. Section 10 is devoted to a phenomenological analysis of the  $x$  dependence of  $F_2$  and to extractions of the longitudinal structure function  $F_L$  and in Sect. 11 the data are compared to phenomenological models. A summary is given in Sect. 12.

## 2 Definitions

In the low  $Q^2$  kinematic range of the present measurement, contributions from  $Z$  boson exchange to neutral current deep inelastic scattering can be neglected. In the one-photon exchange approximation, the double differential cross section for neutral current DIS is given, in its reduced form  $\sigma_r$ , by

$$\begin{aligned}\sigma_r &= \frac{Q^4 x}{2\pi\alpha^2[1 + (1 - y)^2]} \cdot \frac{d^2\sigma}{dx dQ^2} \\ &= F_2(x, Q^2) - f(y) \cdot F_L(x, Q^2)\end{aligned}\quad (1)$$

with the fine structure constant denoted  $\alpha$  and  $f(y) = y^2/[1 + (1 - y)^2]$ . The inelasticity  $y$  is related to  $Q^2$ ,  $x$  and the centre-of-mass energy squared,  $s = 4E_e E_p$ , by  $y = Q^2/sx$ . In the quark-parton model (QPM),  $x$  denotes the fraction of the proton momentum carried by the parton coupling to the exchanged boson.

The DIS cross section, see (1), is determined by two structure functions,  $F_2$  and  $F_L$ . These are related to the cross sections for the scattering of longitudinally and transversely polarised photons off protons,  $\sigma_L$  and  $\sigma_T$ . At low  $x$ , the relationships

$$F_L = \frac{Q^2}{4\pi^2\alpha}(1 - x) \cdot \sigma_L, \quad (2)$$

$$F_2 = \frac{Q^2}{4\pi^2\alpha}(1 - x) \cdot (\sigma_L + \sigma_T), \quad (3)$$

hold to very good approximation. Positivity of the longitudinal and transverse scattering cross sections imposes the restriction  $0 \leq F_L \leq F_2$ . Using the ratio  $R(x, Q^2)$

$$R = \frac{\sigma_L}{\sigma_T} = \frac{F_L}{F_2 - F_L}, \quad (4)$$

the reduced cross section in (1) can be written as

$$\sigma_r = F_2(x, Q^2) \cdot \left[ 1 - f(y) \cdot \frac{R}{1 + R} \right]. \quad (5)$$

For most of the kinematic domain, the reduced DIS neutral current scattering cross section is well approximated by the  $F_2$  structure function, since  $F_L$  leads to a sizeable effect only for large inelasticity values  $y$ .

The reduced cross section  $\sigma_r$  can be re-expressed as

$$\sigma_r = \frac{Q^2(1 - x)}{4\pi^2\alpha} \sigma_{\gamma^*p}^{\text{eff}}, \quad (6)$$

with the effective virtual photon-proton cross section

$$\sigma_{\gamma^*p}^{\text{eff}} = \sigma_T + [1 - f(y)]\sigma_L. \quad (7)$$

The sum  $\sigma_L + \sigma_T$  is referred to as the total virtual photon-proton cross section,  $\sigma_{\gamma^*p}^{\text{tot}}$ , which is often expressed as a

function of  $Q^2$  and of the invariant mass of the virtual photon-proton system,  $W$ . For small  $x$ ,  $W$  can be calculated as  $W = \sqrt{Q^2(1-x)/x}$ , such that  $W^2 \simeq sy$ . The total and the effective virtual photon-proton cross sections differ significantly only in the region of high  $y$ .

### 3 Models

The low  $x$  data presented here extend to low values of  $Q^2$  for which perturbative QCD is not applicable. The phenomenological models formulated for this transition region reproduce the  $W$  dependence of the  $\gamma^*p$  cross section, which is weak in the photoproduction region [40]. A steep increase towards large values of  $W$  develops in the perturbative region, which is equivalent to the rise of the proton structure function  $F_2$  towards low  $x$  at fixed  $Q^2$ .

In the context of the present measurement colour dipole models (e.g. [41–46]) are particularly interesting because  $F_L$  and  $F_T = F_2 - F_L$  are both described by a single characteristic dipole scattering cross section  $\hat{\sigma}$  combined with either the longitudinal or the transverse photon wavefunction. The squares of the wavefunctions of the  $q\bar{q}$  fluctuations of longitudinally and transversally polarised photons are [30]

$$W_L(z, r, Q^2) = \frac{6\alpha}{\pi^2} \sum_{i=1}^{n_f} e_i^2 Q^2 z^2 (1-z)^2 K_0(\epsilon r)^2,$$

$$W_T(z, r, Q^2) = \frac{3\alpha}{2\pi^2} \sum_{i=1}^{n_f} e_i^2 [(1-2z(1-z))\epsilon^2 K_1(\epsilon r) + m_i^2 K_0(\epsilon r)], \tag{8}$$

where  $\epsilon^2 = m_i^2 + z(1-z)Q^2$ ,  $m_i$  ( $e_i$ ) is the mass (charge) of quark  $i$ ,  $K_0(u)$  and  $K_1(u) = -\partial_u K_0$  are modified Bessel functions,  $r$  is the transverse separation of the  $q\bar{q}$  pair and  $z$  denotes the fractional energy sharing between  $q$  and  $\bar{q}$ . In this approach the cross sections  $\sigma_{T,L}$  are obtained from integrals over the impact parameter space as

$$\sigma_{L,T}(x, Q^2) = \int d^2r \int_0^1 dz W_{L,T}(z, r, Q^2) \hat{\sigma}(x, r^2). \tag{9}$$

Colour dipole models differ by the chosen expressions for the cross section  $\hat{\sigma}$ . With the measurement extending into the region of high  $y$  one can confront the predictions of such models for the two structure functions with the data. As an illustration, the data are compared in this paper to two versions of the colour dipole model, the original version by Golec-Biernat and Wüsthoff (GBW) [42] and a more recent model, based on the Colour Glass Condensate approach to the high parton density regime, by Iancu, Itakura and Munier (IIM) [45].

Two further models are used in this paper in order to parameterise  $F_2(x, Q^2)$ . The fractal model is based on the

observation that the proton structure at low  $x$  exhibits self-similar properties for different  $x$  and  $Q^2$  values. Two continuous, variable and correlated fractal dimensions are chosen to describe the self-similarity in  $x$  and  $Q^2$  [33]. In a more phenomenological approach  $F_2$  is parameterised as  $x^{-\lambda(Q^2)}$ . These two models are also compared with the reduced cross section,  $\sigma_r$ , after making assumptions on  $R$ .

### 4 Measurement of the DIS cross section

#### 4.1 Reconstruction of event kinematics

In the colliding beam experiments at HERA, the DIS event kinematics can be reconstructed using the measurements of the scattered lepton, the hadronic final state, or a combination of the two. This complementarity enlarges the kinematic coverage and provides an additional control of the systematic uncertainties.

The energy of the scattered positron  $E'_e$  and its polar angle  $\theta_e$  are used in the “electron method” to determine the kinematics via

$$y_e = \frac{2E_e - E'_e(1 - \cos\theta_e)}{2E_e} \equiv \frac{2E_e - \Sigma_e}{2E_e}, \tag{10}$$

$$Q_e^2 = \frac{E_e'^2 \sin^2\theta_e}{1 - y_e}, \quad x_e = \frac{Q_e^2}{4E_p E_e y_e}. \tag{11}$$

Using energy-momentum conservation, the event kinematics can also be determined from the hadronic final state. An important quantity is the difference between the total energy and the total longitudinal momentum

$$E - P_z \equiv E'_e(1 - \cos\theta_e) + \sum_i (E_i - P_{z,i}) \equiv \Sigma_e + \Sigma_h, \tag{12}$$

where  $E_i$  ( $P_{z,i}$ ) is the reconstructed energy (longitudinal component of the momentum) of a particle  $i$  from the hadronic final state. In the reconstruction, masses are neglected for both the positron and the hadronic final state particles. The measured  $E - P_z$  is insensitive to losses in the proton beam direction and is thus only weakly affected by the incomplete reconstruction of the proton remnant. For non-radiative events, the relation  $E - P_z \simeq 2E_e$  holds. This allows  $2E_e - \Sigma_e$  in (10) to be replaced by  $\Sigma_h$  and leads to the introduction of the  $y_h$  variable [47]

$$y_h = \frac{\Sigma_h}{2E_e}. \tag{13}$$

For events, in which a photon is emitted collinearly to the incoming positron, the radiated photon is not reconstructed in the sub-detectors used to calculate  $E - P_z$ . In this case  $(E - P_z)/2$  is equal to an “effective” incident positron beam energy, reduced relatively to the nominal beam energy by

the momentum carried by the radiated photon. This is employed in the  $\Sigma$  method, for which  $2E_e$  in (13) is substituted by the measured  $E - P_z$  [48]

$$y_\Sigma = \frac{\Sigma_h}{E - P_z}. \quad (14)$$

For this method,  $Q^2$  is calculated by replacing  $y_e$  in (11) by  $y_\Sigma$ , and Bjorken  $x$  is calculated by substituting  $y_e$ ,  $Q_e^2$  and  $2E_e$  by  $y_\Sigma$ ,  $Q_\Sigma^2$  and  $E - P_z$ , respectively<sup>3</sup>

$$Q_\Sigma^2 = \frac{E_e'^2 \sin^2 \theta_e}{1 - y_\Sigma}, \quad x_\Sigma = \frac{Q_\Sigma^2}{2E_p y_\Sigma} \cdot \frac{1}{E - P_z}. \quad (15)$$

By using a consistent set of the variables  $x_\Sigma$ ,  $y_\Sigma$  and  $Q_\Sigma^2$ , the measurement also correctly reconstructs the kinematics for events with initial state QED radiation. Therefore, the method covers lower  $Q^2$  and higher  $x$  values, which become accessible due to the reduced centre-of-mass energy for these events.

The total transverse momentum of the hadronic final state is

$$P_T^h = \left| \sum_i \mathbf{P}_{T,i} \right| \quad (16)$$

where  $\mathbf{P}_{T,i}$  is the transverse momentum vector of the particle  $i$  and the sum runs over all particles.  $P_T^h$  is rather insensitive to particle losses collinear to the beam for a wide range of  $y$ . The combination of  $P_T^h$  and  $\Sigma_h$  defines the hadronic scattering angle

$$\tan \frac{\theta_h}{2} = \frac{\Sigma_h}{P_T^h}, \quad (17)$$

which, within the QPM, follows the direction of the struck quark.

In this analysis, both the electron and the  $\Sigma$  methods are used for the cross section measurement. The electron method provides the better resolution in  $x$  for large inelasticities  $y > 0.1$ , but the resolution degrades as  $1/y$ . Use of the  $\Sigma$  method extends the measurement down to  $y \sim 0.002$ . Below this  $y$  value, losses along the proton beam direction become important and are difficult to estimate. The  $\Sigma$  method as is used here noticeably increases the kinematic coverage towards low  $Q^2$  and high Bjorken  $x$  due to initial state QED radiation.

#### 4.2 Determination of the DIS cross section

The measurement of the double differential cross section is performed in bins of  $x$  and  $Q^2$ , or  $y$  and  $Q^2$ , depending on

<sup>3</sup>Note that in previous H1 publications the nominal positron beam energy was used instead of  $(E - P_z)/2$  in the calculation of  $x_\Sigma$ . The method of  $x$  calculation used here is called the  $I\Sigma$  method in [48].

the region in the kinematic phase space, as shown in Fig. 1. The bin sizes and shapes as well as methods used for the kinematic reconstruction are chosen based on the following prescription:

- In  $Q^2$ , a binning equidistant in  $\log_{10} Q^2$  is chosen with eight bins per decade, as in previous H1 publications [37]. This binning reflects the good  $Q^2$  resolution of the H1 detector.
- The  $x$  and  $Q^2$  values at which the measured double differential cross section is quoted, also referred to as bin centres, are placed at an approximately logarithmic average value within the bin boundaries for the  $x$  and  $Q^2$  binning, and at the linear average for the  $y$  binning.
- For high  $y > 0.6$ , the electron method has an excellent kinematic resolution. In this region, the measured cross section is sensitive to the longitudinal structure function  $F_L$ , which leads to a rapidly changing shape of the reduced cross section as a function of  $y$ . Therefore a fine binning, linear in  $y$ , is chosen for  $y > 0.6$ : two  $y$  bins are used for each  $Q^2$  interval with boundaries at  $y = 0.85$ ,  $0.75$  and  $0.6$ .
- For  $y < 0.6$  the binning is defined in  $x$ . The default  $x$  binning is equidistant in  $\log_{10} x$  with five bins per decade, as chosen previously [37]. The transition between the  $x$  and  $y$  binning is defined by the  $y$  value of the nominal bin centre,  $y_c$ , for the transition bins: for  $y_c > 0.6$ , the bin is combined with the nearest  $y$  bin and for  $y_c \leq 0.6$  it is combined with the nearest  $x$  bin.

The resolution in each bin is checked using a Monte Carlo simulation. Two variables are calculated for this purpose, the purity  $P = N_{\text{rec,gen}}/N_{\text{rec}}$  and the stability  $S = N_{\text{rec,gen}}/N_{\text{gen}}$ , where  $N_{\text{rec}}$  ( $N_{\text{gen}}$ ) is the total number of reconstructed (generated) Monte Carlo events in the bin and  $N_{\text{rec,gen}}$  is the number of events which are both generated and reconstructed in the same bin. The purity and stability are calculated for both the electron and the  $\Sigma$  methods. For the cross section measurement the method with the higher purity is used. The choices are illustrated in Fig. 1. The purity and stability typically exceed 50%. If either the purity or the stability is below 25% in a bin for the chosen reconstruction method, the bin is combined with an adjacent bin. Bins with larger sizes can thus be created at the acceptance edges as shown in Fig. 1.

The  $\theta_e = 176.5^\circ$  and  $\theta_e = 178^\circ$  lines in Fig. 1 indicate the approximate angular acceptance limits of the H1 detector for the nominal and the shifted vertex positions, respectively. In each plot measurement bins below  $\theta_e$  lines are visible. The measurement in these bins becomes possible using the  $\Sigma$  method for events with initial state photon radiation which effectively reduces the centre-of-mass energy. These bins are further referred to as ISR bins. The  $\Sigma$  method cannot be used at high  $y$ , where its resolution is poor, lead-

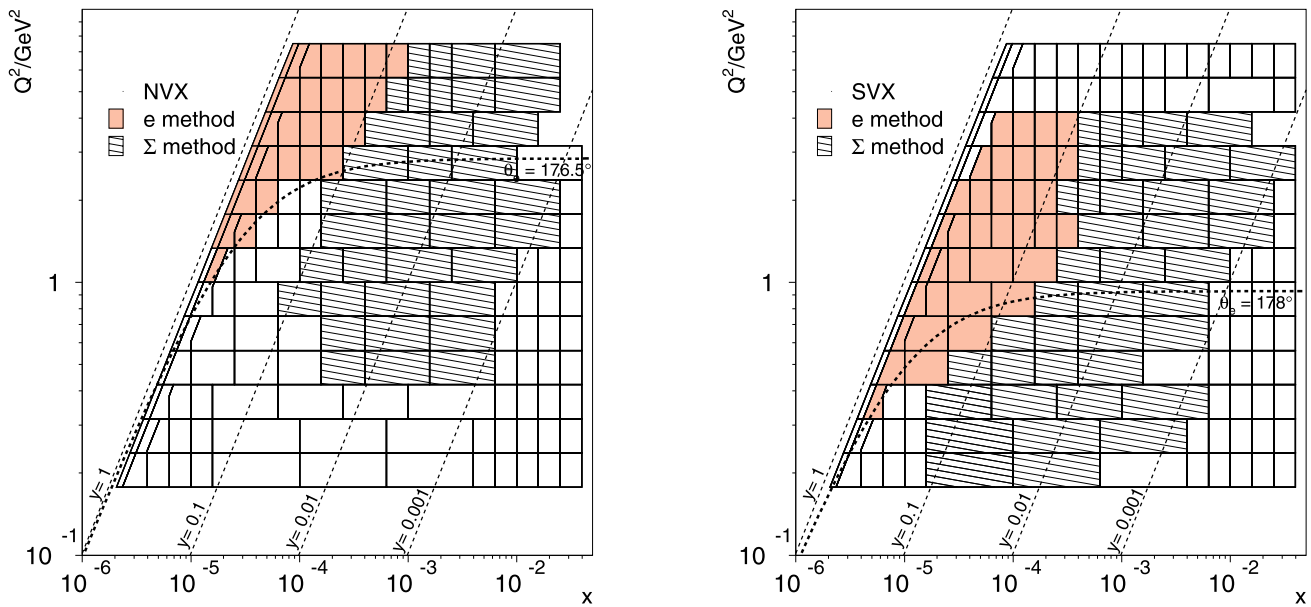


**Fig. 1** Illustration of the bins used for the cross section measurement in the NVX (left) and SVX (right) analyses. Dashed lines of constant  $\theta_e$  indicate approximate angular acceptance for both measurements. The dark (light) shaded area corresponds to the bins where the elec-

tron ( $\Sigma$ ) method is used for the measurement of the cross section. The measurement in the bins outside the angular acceptance range employ the  $\Sigma$  method for ISR events

ing to large migrations of nominal energy events into the ISR bins and thus to purities below the accepted value. This causes the gap between the ISR and electron method bins at high  $y$ .

The calculation of the reduced double differential  $ep$  cross section is performed by correcting the data using the MC simulations. The following formula is applied to each analysis bin

$$\sigma_r(x_c, Q_c^2) = \frac{N_{\text{data}} - N_{\text{bg}}}{A\epsilon\mathcal{L}_{\text{data}}} \frac{c_{\text{bc}}}{1 + \delta_{\text{rc}}}. \tag{18}$$

Here,  $(x_c, Q_c^2)$  is the bin centre,  $N_{\text{data}}$  is the number of data events,  $N_{\text{bg}}$  is the number of background events, estimated using MC simulations,  $A$  and  $\epsilon$  are the detector acceptance and efficiency,  $\mathcal{L}_{\text{data}}$  is the integrated luminosity,  $\delta_{\text{rc}}$  are QED radiative corrections, and  $c_{\text{bc}}$  are the corrections for finite bin size effects. The radiative and bin centre corrections can be determined using the Monte Carlo simulation. In this case, (18) becomes

$$\sigma_r(x_c, Q_c^2) = \frac{N_{\text{data}} - N_{\text{bg}}}{N_{\text{MC}}} \frac{\mathcal{L}_{\text{MC}}}{\mathcal{L}_{\text{data}}} \sigma_r^{\text{MC}}(x_c, Q_c^2), \tag{19}$$

where  $N_{\text{MC}}$  is the number of signal MC events and  $\mathcal{L}_{\text{MC}} = N_{\text{gen}}/\sigma_{\text{gen}}$  is the Monte Carlo luminosity. Here  $N_{\text{gen}}$  denotes the total number of generated MC events and  $\sigma_{\text{gen}}$  is the total integrated cross section for the MC generation. The quantity  $\sigma_r^{\text{MC}}(x_c, Q_c^2)$  is the reduced double differential cross

section at the bin centre calculated at the Born level with the same structure functions as are used in the MC generation.

The correction for the detector acceptance using Monte Carlo modelling requires the cross section model used in the simulation to be sufficiently close to the data, such that migrations between the bins are well reproduced. The cross section model should also describe the kinematic region outside the measurement range, in particular at low  $y$  and low  $Q^2$ , to account for radiative corrections and long range migrations. In practice, this is achieved using an iterative MC event reweighting procedure which converges after one iteration for the measurement region. First, the double differential cross section is measured following (19) using an initial approximation for the MC input cross section. Next, the measured double differential cross section is fitted with a new parameterisation using the fractal model and the analysis of the Monte Carlo events is repeated with an additional weight factor, equal to the ratio of the new to the initial double differential cross sections in each simulated event. For the reweighting, the event kinematics are calculated using the generated  $x$  and  $Q^2$  variables at the hadronic vertex, such that corrections due to radiation from the lepton line are properly accounted for. This reweighting procedure is used for the measurement region. For the high  $x > 0.02$  domain, which lies outside the measurement region, the ALLM parameterisation [49] is used.

## 5 H1 detector

### 5.1 Overview

A complete description of the H1 detector is given in [50, 51]. Here the components used for the present measurement are discussed. In Sect. 5.2 the detectors for the scattered electron measurement are described in detail. A schematic view of the H1 detector is given in Fig. 2, in which a typical low  $Q^2$  event is shown.

Around the interaction region a set of tracking chambers, surrounded by electromagnetic and hadronic calorimeters, operates in a solenoidal magnetic field of 1.16 T. The tracking system is subdivided into forward, central and backward tracking devices. The nominal interaction point of the electron and proton beams lies about in the middle of the Central Tracker, at the origin of the coordinate system. The interaction vertex positions have an approximately Gaussian distribution in  $z$  with  $\sigma_z \approx 10$  cm. The calorimetry system consists of the Liquid Argon calorimeter (LAr) covering the central and forward directions and the lead-scintillator spaghetti calorimeter (SpaCal) [52–55] measuring particles scattered backwards.

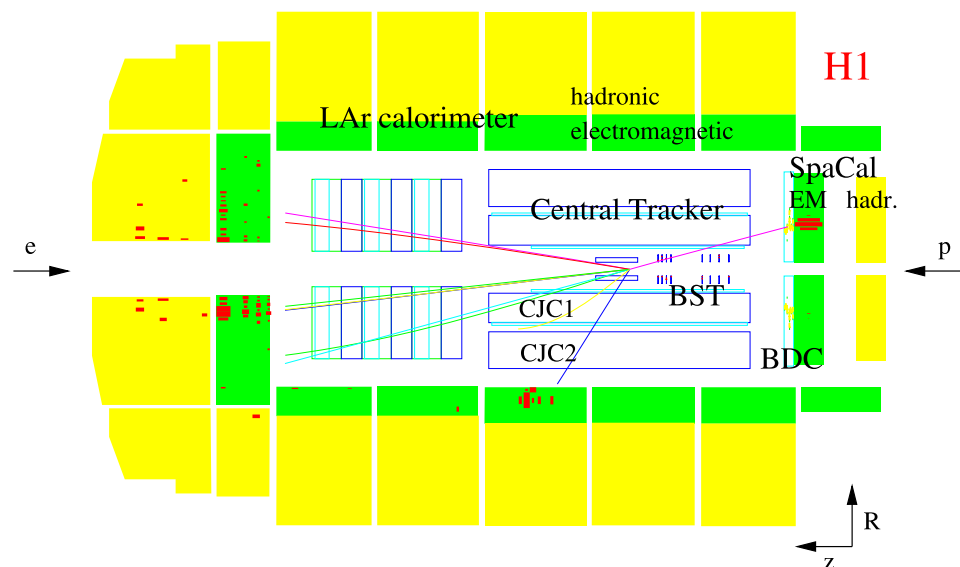
The Central Tracker consists of four drift chambers, two multi-wire proportional chambers (MWPCs) and a silicon tracking device. The largest tracker components are the two concentric drift chambers, CJC1 and CJC2, which have sense wires strung parallel to the beam axis with the drift cells inclined at about  $30^\circ$  with respect to the radial direction, such that the drift direction of ionisation electrons is approximately perpendicular to the wire plane. The charge deposits are read out from both ends of each wire, providing particle identification via ionisation energy loss and an approximate determination of the  $z$  coordinate via the charge asymmetry between the two wire end signals (“charge division”).

Tracks found in the CJC are linked to the hits found in two chambers equipped with wires strung around the beam axis, following polygonal support structures, dedicated to the precise measurement of  $z$  coordinates. The inner  $z$  chamber (CIZ) is located inside CJC1 and the outer  $z$  chamber (COZ) lies between CJC1 and CJC2. To reduce the number of acceptable combinations with the CJC, the  $z$  chambers also determine a  $\phi$  coordinate using the charge division measurement. The tracks are further constrained by linking to hits in the central silicon tracker (CST) [56]. The CST consists of two layers of double-sided silicon strip detectors surrounding the beam pipe, covering an angular range of  $30^\circ < \theta < 150^\circ$  for tracks passing through both layers.

The two cylindrical proportional chambers, the CIP mounted inside CIZ, and the COP located between the COZ and CJC2, are used together to identify tracks pointing to the interaction vertex and thus to reduce background at the trigger level. A combined CIP-COP signal is used in coincidence with the SpaCal to trigger events with low  $E'_e$  (see Sect. 6.1).

The LAr calorimeter [57], mounted in a large cryostat, is used in this analysis for the measurement of the hadronic energy. The angular coverage of the calorimeter is  $4^\circ < \theta < 154^\circ$  for an interaction vertex at  $z = 0$ . The calorimeter consists of an electromagnetic section with lead absorbers (20–30 radiation lengths) and a hadronic section with steel absorbers. The total depth is between 4.5 and 8 hadronic interaction lengths. The LAr calorimeter is divided along the  $z$  direction into wheels. The electromagnetic section has eight wheels while the hadronic section has seven. The calorimeter has a high degree of spatial segmentation with a total of about 45000 cells. Its hadronic energy resolution, as determined in test beam measurements [58], is  $\sigma_E/E \approx 50\%/\sqrt{E/\text{GeV}} \oplus 2\%$ .

**Fig. 2** A low  $Q^2$  event as reconstructed in the H1 detector. The electron is scattered into the backward region. The electron trajectory is reconstructed in the Backward Silicon Tracker (BST) and in the Backward Drift Chamber (BDC). The electron energy is determined using the SpaCal calorimeter. The hadronic final state is detected in the central and forward tracking detectors, and in the LAr calorimeter





Two electromagnetic crystal calorimeters, a photon tagger (PT) and an electron tagger (ET), located at  $z = -103.1$  m and  $z = -33$  m, respectively, are used to monitor the luminosity via the measurement of the Bethe-Heitler process  $ep \rightarrow \gamma ep$ . The luminosity corresponding to the main interaction region can be separated from the additional (“satellite”) interaction regions using information from the scintillator hodoscopes of the time-of-flight system (TOF) and from the HERA proton pick-up (PPU) monitor, a 34 cm long stripline device located at  $-3$  m from the interaction point. The ET can be used to measure the scattered electron in photoproduction processes, with  $Q^2 \leq 10^{-2} \text{ GeV}^2$  and  $0.2 < y < 0.7$ . The PT detects photons radiated collinearly to the incoming electron direction.

## 5.2 Backward detectors

The measurement of the inelastic  $ep$  scattering cross section at low  $Q^2$  relies on the identification of the scattered electron in the backward part of the H1 apparatus. The energy of the scattered electron is measured in the SpaCal calorimeter. For the low  $Q^2$  region under study,  $\theta_e$  lies outside the angular acceptance of the Central Tracker. The polar angle of the scattered electron can, however, be measured either by the Backward Silicon Tracker (BST), based solely on the electron track, or by a combination of the less precise Backward Drift Chamber (BDC) signal with the hadronic final state vertex, as reconstructed using the Central Tracker. The redundancy of the angular measurements provides additional cross checks over a large angular range, whilst the BDC extends the polar angle coverage to larger  $\theta_e$ .

### 5.2.1 Backward silicon tracker

The BST in the configuration installed in 1999 [59] is schematically shown in Fig. 3. It consists of eight planes

(disks) and 16 azimuthal sectors. The planes are mounted perpendicularly to the beam axis and are arranged in two modules, BST1 and BST2, of four planes each. A first version of the BST with four planes is described in [60].

Each BST plane is equipped with 16 wedge shaped, single sided, double metal, silicon strip sensors of  $250 \mu\text{m}$  thickness. Each sensor contains 640 sensitive  $p$  strips which are concentric around the beam axis with a pitch of  $96 \mu\text{m}$ . The signals are amplified and temporarily stored by five on-detector front-end chips, called Analogue Pipeline Chips [61] (APCs), until a readout instruction is received [62]. Using these “ $r$  sensors” (Fig. 4a) the track polar angle can be determined. The acceptance range of the BST for the nominal vertex position is  $164^\circ < \theta_e < 176^\circ$ .

In addition to the  $r$  sensors, each plane contains one single sided, single metal, silicon strip sensor, in the azimuthal sector  $45^\circ < \phi < 67.5^\circ$  mounted behind the  $r$  sensor. This “ $u$  sensor” has 640 sensitive strips parallel to the reference edge of the sensor with a pitch of  $75 \mu\text{m}$  (Fig. 4b). It thus measures hits in  $u$  coordinate space defined by  $u = r \sin \phi_u$ , where  $\phi_u$  is the azimuthal angle with respect to the reference edge of the sensor. Combining the information from  $r$  and  $u$  sensors, it is possible to measure the transverse momentum and determine the charge of a track in the BST. This feature is used in this analysis to cross check the simulation of photoproduction background.

During data taking an online hit finding is performed. This takes into account individual pedestals of each channel, which are dynamically updated. Coherent shifts in the amplitude of groups of strips, so called “common mode”, are also corrected for. For reconstructed tracks, the most probable signal-to-noise values for the hits is about 15 for the  $r$  sensors and 30 for the  $u$  sensors. The single hit resolution is  $20$  ( $15$ )  $\mu\text{m}$  for the  $r$  ( $u$ ) coordinate.

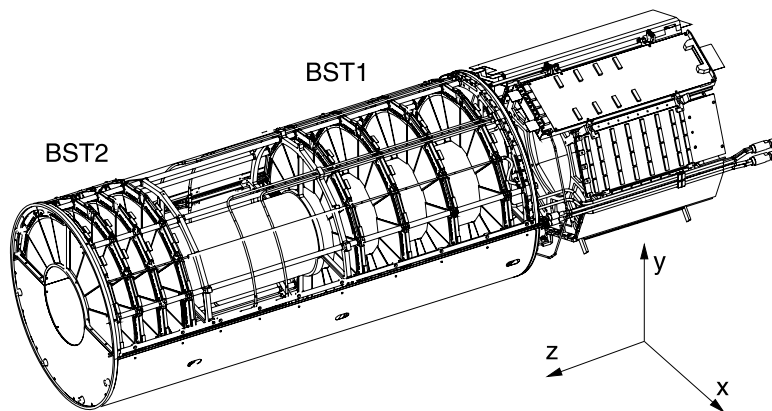
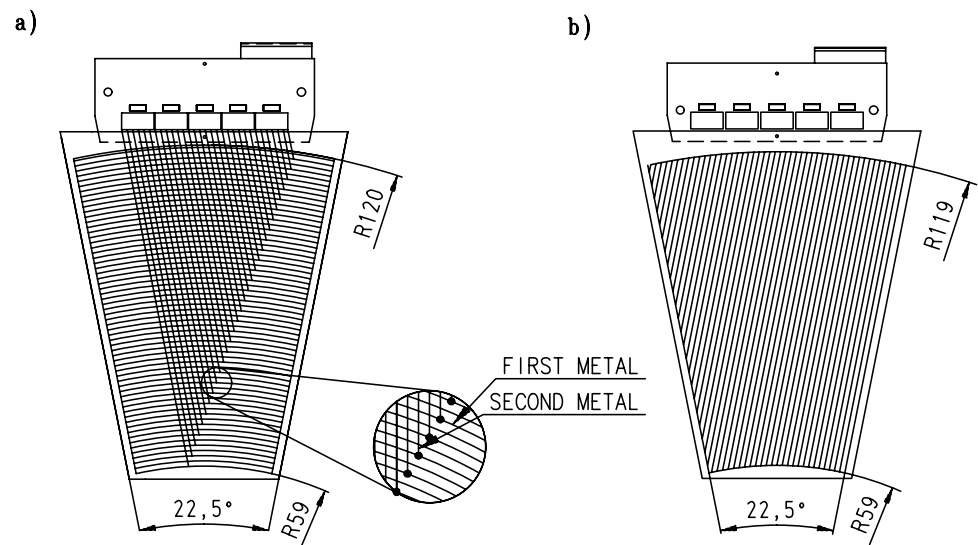


**Fig. 3** Schematic layout of the H1 Backward Silicon Tracker (BST). The active area is composed of eight wheels subdivided into two modules, BST1 and BST2, of four wheels each. One wheel is made of 16  $r$  sensors and one  $u$  sensor (mounted on the back side, not shown here).

Eight consecutive sensors in  $1/16$  of azimuth build a BST sector. In  $z$  the module BST1 extends from  $-73.2$  to  $-95.7$  cm, BST2 from  $-35.9$  to  $-46.9$  cm. Readout boards are placed in the rear section. Also indicated are the electric shielding and the water cooling pipes

**Fig. 4** The two types of silicon sensors used in the BST: (a)  $r$  sensor, (b)  $u$  sensor, each with 640 readout strips. The  $r$  sensor has a double metal structure for the readout lines to reach the top (outer radius) part where the five amplifiers are mounted on the hybrid, as sketched



### 5.2.2 SpaCal and BDC

The SpaCal calorimeter covers the polar angle range of  $153^\circ < \theta < 177^\circ$  as measured from the nominal  $z$  vertex position. It consists of an electromagnetic section [53–55] with 1192 cells of size  $4.05 \times 4.05 \times 25 \text{ cm}^3$  in front of a hadronic section with 136 cells of size  $11.9 \times 11.9 \times 25 \text{ cm}^3$ . The total amount of passive material traversed by particles from the interaction vertex up to the SpaCal is of the order of one radiation length. The electromagnetic section comprises 27.5 radiation lengths and provides an electromagnetic energy resolution of  $\sigma_E/E = 7\%/\sqrt{E/\text{GeV}} \oplus 1\%$ . The hadronic section [52] is used for a coarse hadronic energy measurement and to distinguish hadronic from electromagnetic showers. The whole calorimeter comprises 2 hadronic interaction lengths. The energy resolution for hadrons amounts to  $\sigma_E/E \sim 60\%/\sqrt{E/\text{GeV}}$ .

The SpaCal cells consist of lead sheets with embedded scintillating fibres. The fibres from each cell are bundled together and attached via light mixers to photomultiplier tubes (PMTs). The stability of the PMT gain can be checked using a dedicated LED system.

The backward drift chamber [63] is mounted in front of the SpaCal and has the same angular acceptance. It consists of four double layers, each of them divided azimuthally into eight sectors. A three dimensional view of a section of the BDC is given in Fig. 5. The sense wires are strung perpendicularly to the beam axis and are fixed at the sector edges leading to an octagonal geometry with almost radial drift directions. The drift cells are 1 cm wide in the inner region and 3 cm wide in the outer. At the transition from the inner to the outer region a special cell is introduced with 0.5 cm drift distance at the inner side and 1.5 cm drift distance at the outer. The cells within one double layer are shifted by half a drift cell in the radial direction to solve the inner-outer hit assignment ambiguity. The double layers are rotated by

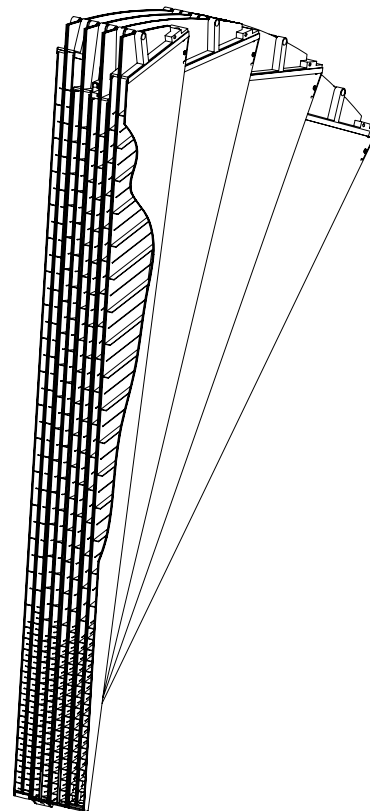


**Fig. 5** Three-dimensional view of a section of the BDC illustrating the layer structure and the drift cell geometry. The chamber has a radial coverage from 6 cm to 71 cm. At a radius of about 22 cm the segmentation is changed and a transition drift cell is introduced

$11.25^\circ$  with respect to each other to allow for reconstruction of the azimuthal coordinate. In addition, this reduces the efficiency losses at the sector edges. The radial resolution for minimum ionising particles is  $400 \mu\text{m}$ . The resolution in the azimuthal direction is about 2 mm.

## 6 Data collection and reconstruction

The H1 detector uses a multi-level trigger system for data collection in which two hardware trigger levels are followed by a software filter farm. After improvements of the detector calibration and the reconstruction code, the data are reprocessed offline. This section describes the first analysis stages, including the online data selection and the reconstruction algorithms.

### 6.1 Online event selection

The online trigger conditions used in this analysis (Table 1) are based primarily on a localised energy deposition in the electromagnetic section of the SpaCal (inclusive electron trigger). Three different energy thresholds are used. The trigger condition based on the lowest energy threshold (S9) collects events at the highest  $y$ . Since a significant background contamination is present at low energies and radii, the inner SpaCal region is excluded from S9. To maintain an acceptable trigger rate, S9 contains an extra condition requiring the pattern of hit pads in the CIP-COP proportional chambers to be consistent with at least one vertex pointing track. This condition is similar to the requirement of a reconstructed track from the hadronic final state in the Central Tracker.

### 6.2 Track and vertex reconstruction in the central tracker

The track reconstruction in the Central Tracker is initiated from the CJC hit measurements. Initially, candidate trajectories are found in the  $xy$  plane using a fast circle fit algorithm [64]. The  $z$  coordinate is added to the tracks based on charge division information. A linear fit in  $S$ - $z$  space is performed where the  $S$  coordinate measures an arc length of the track in the  $xy$  projection. Next, the tracks are fitted to a common vertex in the  $xy$  plane. At this stage detailed corrections are applied for multiple scattering in the detector material and for magnetic field non-uniformity. For the tracks which are determined by the fit to originate from a common  $xy$  vertex, a combined  $S$ - $z$  fit is performed to determine an initial approximation of the vertex  $z$  position and of the track polar angles.

**Table 1** Overview of the main trigger conditions used for the NVX and SVX analyses.  $r_{\text{sp}}$  is the radial coordinate of the SpaCal cluster

Trigger name	Energy threshold	Effective $r_{\text{sp}}$ cut	Tracking condition
S3	12.0 GeV	10 cm	–
S0	6.5 GeV	12 cm	–
S9	2.0 GeV	15 cm	CIP-COP track

The vertex-fitted CJC tracks are then combined with hits found in the  $z$  chambers, employing a robust global minimisation technique [65]. This link improves the  $z$  vertex resolution from about 1 cm to 1 mm. The track  $\theta$  resolution is correspondingly improved from approximately 10 mrad to 1 mrad. For the NVX sample, where the  $z$  coordinate of the interaction vertex is around zero, the CJC tracks are also combined with hits found in the CST resulting in a vertex resolution of about 0.1 mm. CST hits are not used for the SVX sample since the interaction vertex position is outside the CST acceptance.

### 6.3 Reconstruction of the electron kinematics

#### 6.3.1 Energy reconstruction in the SpaCal calorimeter

The reconstruction of the scattered electron kinematics is based on the measurement of a deposition of energy, termed a cluster, found in the electromagnetic SpaCal. The clustering algorithm searches for a cell with a local maximum in energy. The cluster is then built around this seed cell by adding neighbouring cells with energies above the noise threshold. The centre-of-gravity of the cluster is determined based on all associated cells using a logarithmic energy weighting. To suppress background from hadrons and from decays of  $\pi^0 \rightarrow \gamma\gamma$  with the photons reconstructed in a single cluster, a cluster radius estimator,  $R_{\text{log}}$ , is used based on logarithmic energy weighting. The background from hadronic particles is further suppressed using a cut on the energy deposit,  $E_{\text{had}}$ , in the hadronic section of the SpaCal behind the electromagnetic cluster.

The electron candidate cluster is required to be associated to a track in one of the backward trackers, BDC or BST, in order to reduce background from backward photons and to measure the polar angle  $\theta_e$  accurately. For the determination of  $\theta_e$ , the trajectory of the scattered electron is assumed to be a straight line in  $r$ - $z$  coordinate space.

#### 6.3.2 Track reconstruction in the BDC

The BDC reconstruction of the electron scattering angle  $\theta_e$  starts from the line connecting the SpaCal cluster and the Central Tracker vertex as an initial approximation. The scattered electron azimuthal angle  $\phi_e$  is taken from the SpaCal cluster centre-of-gravity. Only the BDC hits in the octant containing  $\phi_e$  are used for the  $\theta_e$  reconstruction.

The  $\theta_e$  determination follows from a minimisation procedure. A least squares track fit combines the Central Tracker vertex, the SpaCal cluster centre-of-gravity energy, and all BDC measurements in a corridor of variable size  $\Delta r$  around the current best estimate of the track direction. Initially, the corridor has a size of 5 cm. It is gradually reduced with improved track parameters to about five times the BDC resolution. The SpaCal cluster is considered to be linked to the

BDC track segment if there are at least four hits from the eight layers remaining at the final iteration and if the radial distance between the track projected to the SpaCal  $z$  coordinate and the SpaCal cluster is less than 2.5 cm.

### 6.3.3 Track reconstruction in the BST

The reconstruction of the electron track in the BST uses the azimuthal location of the SpaCal cluster. The three adjacent sectors which in azimuth are closest to  $\phi_e$  are selected. The  $r$  coordinates of all BST hits in the selected sectors are projected along the line defined by the hit and the SpaCal cluster to the BST plane closest to the SpaCal. A clustering of the projected hits in this plane is then performed using a histogram technique. The line connecting the position corresponding to the peak in the histogram and the SpaCal cluster is used as an initial approximation for the track.

The track finding then proceeds using an iterative minimisation technique with robust rejection of outliers, similar to the BDC reconstruction. All hits in the selected sectors are included into a least squares minimisation. The contribution of each hit is weighted with an exponential suppression factor, which depends on the distance from the hit to the track, and on an additional parameter, which defines the width of an effective corridor around the track. For the first iteration, the width of the corridor is equal to the SpaCal spatial resolution. For further iterations the width is gradually reduced until it reaches five times the BST spatial resolution. The event vertex  $z$  coordinate is given by the distance of closest approach of the BST track to the beam line.

For the sector equipped with the  $u$  strip detectors, the reconstruction of the azimuthal coordinate is also performed. At least three  $u$  hits associated to linked  $r$  hits are required. If multiple  $u$  hits per plane are found, all possible track combinations are formed and the one best matching the SpaCal cluster is selected. To determine the space points, the  $u$  hits are combined with the  $r$  hits extrapolated along the  $r$  track to the  $z$  position of the  $u$  sensor. Then the transformation  $(r, u) \Rightarrow (x, y)$  is performed. A circle fit including the position of the interaction vertex in  $(x, y)$  determined by the beam spot size of  $150\ \mu\text{m}$  in  $x$  and  $60\ \mu\text{m}$  in  $y$ , yields the curvature and therefore charge and the transverse momentum of the particle.

## 6.4 Reconstruction of the hadronic final state

The reconstruction of the hadronic final state uses information from the central tracker and the LAr and SpaCal calorimeters, excluding a cone in the SpaCal calorimeter around the electron candidate cluster. The cone axis is defined by the vertex position and the centre-of-gravity of the SpaCal cluster. The cone radius is 20 cm at the surface of the SpaCal electromagnetic section. The energy of the cells

inside the cone is excluded from the hadronic final state calculation for both the electromagnetic and hadronic sections of the SpaCal.

Tracks pointing to the backward part of the H1 detector are excluded from the hadronic final state. Instead, the reconstructed SpaCal clusters outside the electron isolation cone are used. In the central region, the Central Tracker and LAr signals are linked for each particle by matching the measurements in each detector. For energies below 2 GeV, the tracker information is used while for higher energies the calorimeter information is used, as it provides the better energy resolution.

The determination of  $\Sigma_h$  is affected by the presence of extra activity in the calorimeters. The bias is particularly strong for small  $\Sigma_h$  and thus small  $y_h$ . For the SpaCal, this extra activity can be induced by the scattered electron, with some energy leaking outside the isolation cone or by a radiated photon emitted at a large angle. The contribution of these sources of extra activity to  $\Sigma_h$  is proportional to  $\Sigma_e$  to good approximation. To reduce the influence of these effects, 10% of  $\Sigma_e$  is subtracted from the total SpaCal  $\Sigma_h$ . If the result is negative, the SpaCal contribution is set to zero. This procedure reduces the contribution of SpaCal to  $\Sigma_h$  to a negligible level for low  $y$  events, as is expected from the event kinematics.

Channels affected by electronic noise in the LAr are identified event by event using a dedicated topological algorithm. LAr cells with an energy below 0.4 GeV (0.8 GeV), which are separated from other cells by more than 40 cm (20 cm) in the central (forward) region of the calorimeter are classified as noise and excluded from the  $\Sigma_h$  and  $P_T^h$  calculations.

## 7 Monte Carlo simulations

In the simulation, DIS events are generated using the DJANGO 1.4 [66] event generator which includes leading order QED radiative effects as implemented in HERACLES [67]. For the event generation, leading order parton distribution functions define  $F_2$  while  $F_L$  is set to zero. The structure functions are subsequently reweighted to the fractal model parameterisation of  $F_2$  and to  $F_L$  following the procedure described in Sect. 4.2. The final state parton showers are simulated using the Colour Dipole Model [68, 69] as implemented in ARIADNE 4.1 [70]. Events with a very low mass of the hadronic final state ( $W < 5\ \text{GeV}$ ) are simulated using SOPHIA [71], which includes a detailed description of low mass final states, including the resonance region. The fragmentation into hadrons is performed with JETSET 7.4 [72]. Photoproduction background is generated with the PHOJET 1.6 [73, 74] program, which uses a two-component dual parton model [75] including diffractive processes and vector meson production.

The simulation of QED radiative corrections includes photon emission from the lepton. Radiation from quarks, which is estimated to be small for low  $x$ , is not simulated. The simulation of QED radiative corrections is checked using the analytical calculation package HECTOR [76]. An agreement to better than 0.5% is found in the kinematic range of this measurement.

The generated events are passed through a simulation of the H1 detector response based on the GEANT3 [77] package. Tracing of the particles in the trackers up to the calorimeters is based on a detailed description of the detector material. The response of the calorimeters to electromagnetic particles is simulated using a fast shower parameterisation technique [78], while the hadronic response is simulated using GHEISHA [79].

The level of noise and beam related background in the calorimeters is determined using events from dedicated runs with random triggers which are overlaid on the simulated events. Spurious hits in the BST are added to the simulation based on randomly triggered events.

The MC events are subjected to the same reconstruction and analysis procedure as the data. Also, for consistency of the analysis, the calibrations of the SpaCal and the LAr, as well as the BST and BDC alignments, are performed for the reconstructed MC events in the same way as for the data.

## 8 Data analysis

At low  $Q^2$  the DIS cross section is large, and for the available integrated luminosity for this analysis the statistical uncertainty of the measurement becomes smaller than the systematic uncertainty. For low inelasticities, corresponding to a large fraction of the measured phase space, the scattered electron energy is large and background contributions are negligible compared to the genuine DIS signal. In this region a set of selection criteria is imposed which is sufficient to reconstruct the event kinematics in the least biased way. Whenever possible the electron trajectory is reconstructed using the BST alone and only the SpaCal is used for triggering.

Events with the scattered electron outside the BST acceptance are reconstructed using the BDC and the Central Tracker vertex. The analysis is also extended to the highest accessible  $y$  values for which the precision is limited by the uncertainty of photoproduction background. In this region several additional electron identification criteria are imposed in order to minimise the systematic uncertainty.

For the two data samples, NVX and SVX, a total of four separate analyses is performed as summarised in Table 2. The analyses differ in the triggers and in the method employed for reconstructing  $\theta_e$ . The main kinematic region of the NVX-BST data set, with  $\theta_e$  measured in the BST, is

**Table 2** Inclusive analyses of DIS data. The trigger conditions used to collect the data sets are described in Sect. 6.1, Table 1

Analysis	Trigger	Description
NVX ( $z_{\text{vtx}} \sim 0$ cm)		
NVX-BST	S0	Main analysis
NVX-S9	S9	Extension to lower $E'_e$
SVX ( $z_{\text{vtx}} \sim 70$ cm)		
SVX-BST	S0	Main analysis
SVX-BDC	S0, S3	Extension to larger $\theta_e$

analysed based on the trigger S0. An extension to  $0.75 < y < 0.85$  is achieved using the trigger S9 (NVX-S9) and requiring signals in both tracking detectors, BDC and BST. For the SVX sample, the main region of the phase space is covered by a BST-based analysis with the trigger S0 (SVX-BST). An extension to  $\theta_e = 178^\circ$  is achieved by adding data collected with the trigger S3 and including events with  $\theta_e$  measured by a combination of the Central Tracker vertex and BDC information (SVX-BDC).

The measurement is verified by performing a number of cross check analyses exploiting the redundancy in the kinematic reconstruction and the large overlap of the kinematic regions of different data sets. The data reconstructed with the BST are compared with those reconstructed with the BDC. The results of the electron method are cross checked with those of the  $\Sigma$  method. Moreover, the measurement based on the shifted vertex sample is compared to that based on the nominal vertex sample.

In the following a detailed description of the different analyses is given. Further information can be found in [80–83].

### 8.1 Event selection

#### 8.1.1 Criteria

An overview of the selection criteria used in the different analyses is given in Table 3. The background from non- $ep$  interactions is suppressed by requiring the event vertex ( $z_{\text{vtx}}$ ) to be reconstructed within a distance of  $\pm 35$  cm from the average  $z$  position ( $z_{\text{nom}}$ ). In order to be identified with the scattered electron, the highest energy cluster in the electromagnetic SpaCal section<sup>4</sup> has to satisfy the following criteria: (i) the cluster centre-of-gravity lies in the region of high efficiency of the corresponding trigger; (ii) the transverse cluster radius is consistent with an electromagnetic particle,  $R_{\text{log}} < 4$  cm; (iii) the energy deposition in the hadronic

<sup>4</sup>For the S9 analysis (Table 2) the cluster with the maximum transverse momentum  $P_{\text{T}}^c$  is chosen instead of the highest energy cluster.

**Table 3** Selection criteria used in the analysis

Description	Cut
Common cuts	
Scattered electron energy	$E'_e > 7 \text{ GeV}; 4 \text{ GeV (NVX-S9)}$
Vertex $z$ position	$ z_{\text{VTX}} - z_{\text{nom}}  < 35 \text{ cm}$
SpaCal cluster radius	$R_{\text{log}} < 4 \text{ cm}$
Hadronic energy fraction	$E_{\text{had}}/E'_e < 0.15$
$P_{\text{T}}$ balance	$P_{\text{T}}^h/P_{\text{T}}^e > 0.3$
Electron method cuts	
$E-P_z$ balance	$E-P_z > 35 \text{ GeV}$
BST analysis cuts for NVX-S9, NVX-BST and SVX-BST	
BST validation	$N_{\text{link BST}} \geq 2 \text{ (NVX)}; 3 \text{ (SVX)}$
BST–SpaCal radial match	$ \Delta r_{\text{BST-SpaCal}}  < 1.5 \text{ cm}$
BST noise	$N_{\text{hit total}} < 120 \text{ (NVX)}; 200 \text{ (SVX)}$
BDC analysis cuts for SVX-BDC	
BDC validation	$N_{\text{link BDC}} \geq 4$
BDC–SpaCal radial match	$ \Delta r_{\text{BDC-SpaCal}}  < 2.5 \text{ cm}$
Central Tracker vertex	$N_{\text{track}} \geq 1$ $y_{\Sigma} \geq 0.03$
Additional NVX-S9 analysis cuts	
BST–BDC radial match	$ \Delta r_{\text{BST-BDC}}  < 0.75 \text{ cm}$
BST–CT $z_{\text{VTX}}$ match	$ z_{\text{VTX,BST}} - z_{\text{VTX,CT}} /\sigma < 5.0$
Central Tracker vertex	$N_{\text{track}} \geq 2$

SpaCal section behind the cluster is small,  $E_{\text{had}}/E'_e < 0.15$ ; (iv) depending on the analysis, the cluster is validated by a BST or a BDC track segment. If the highest energy cluster does not satisfy one of these cuts, the next highest energy cluster is used. This procedure is repeated for up to three clusters with energies above 7 GeV, or 4 GeV (NVX-S9).

The further event selection is based on a global balance between the hadronic final state and the electron. Events for which the hadronic final state is poorly reconstructed are rejected by demanding that the total hadronic transverse momentum  $P_{\text{T}}^h$  be at least 30% of the electron transverse momentum  $P_{\text{T}}^e$ . This efficiently removes migrations from very low  $y$ , which lie outside the measurement region. Events with large initial state radiation are excluded from the electron method measurement by requiring  $E-P_z > 35 \text{ GeV}$ . This condition is not used for the  $\Sigma$  method, which takes QED radiation properly into account.

The BST analyses include requirements on the minimum number of BST hits linked to the electron track ( $N_{\text{link BST}}$ ) and on the matching of the BST track extrapolated to the  $z$  position of the SpaCal cluster,  $\Delta r_{\text{BST-SpaCal}}$ . Similarly, for the BDC based analyses, a minimum number of linked BDC hits ( $N_{\text{link BDC}}$ ) and radial BDC–SpaCal matching ( $\Delta r_{\text{BDC-SpaCal}}$ ) are required. In addition, the BST analy-

ses require a low level of noise by cutting on the variable  $N_{\text{hit total}}$ , the total number of BST hits. The BDC analyses demand the presence of at least one central track ( $N_{\text{track}}$ ).

The S9 analysis extends the measurement to low  $E'_e$ , corresponding to high  $y$ , where the largest uncertainty stems from the large photoproduction background. To suppress this background, both the BST and BDC track segments are required to pass the same criteria as in the other analyses. In addition, a tight matching condition is applied for the two trackers using  $\Delta r_{\text{BST-BDC}}$ , the radial distance between the BDC and BST tracks calculated at the BDC plane, as well as  $|z_{\text{VTX,BST}} - z_{\text{VTX,CT}}|/\sigma$ , the distance in  $z$  between the BST vertex and the Central Tracker vertex position divided by the uncertainty of this difference. Finally, to ensure a high trigger efficiency for the analysed sample, at least two central tracks must be reconstructed.

### 8.1.2 Efficiency determination

The efficiencies of the triggers are determined using independently triggered data samples. For the SpaCal trigger conditions, most of the cells show a high (>99.5%) efficiency above the rather sharply defined threshold, see Fig. 6. A few cells are identified which show high thresholds. They are excluded from the analysis by applying geometrical cuts on the electron impact point reconstructed at the calorimeter surface, which is calculated using  $\theta_e$  and  $\phi_e$ . The efficiencies of the CIP-COP conditions employed in the S9 trigger (see Sect. 6.1) are studied as functions of  $E'_e$  and the track multiplicity. Since the average reconstructed track multiplicity increases with  $Q^2$ , the inefficiency diminishes from 3% at  $Q^2 = 1 \text{ GeV}^2$  to 2% at  $Q^2 = 10 \text{ GeV}^2$ . The data are corrected for this inefficiency. The systematic uncertainty on the trigger efficiency is estimated to be 1% for S9 and 0.5% for the other triggers.

The inefficiency of the software filter farm component of the trigger is determined using a sample of the rejected

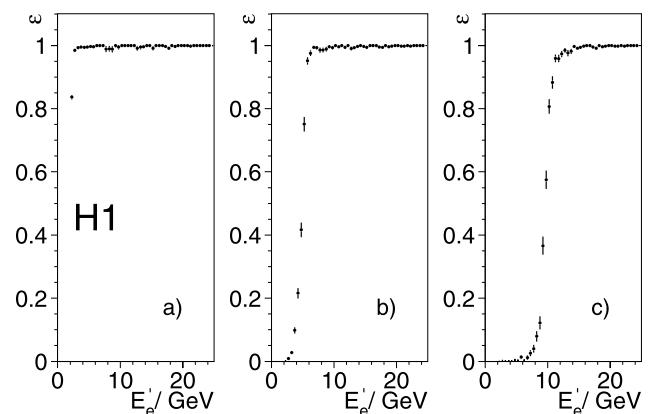


**Fig. 6** Efficiency of the SpaCal electron triggers, S9 (a), S0 (b), and S3 (c), used in this analysis, as a function of  $E'_e$

events, recorded for cross checks. The primary reason for the rejection is the online reconstruction of the event vertex which occasionally wrongly classifies  $ep$  events as non- $ep$  background. The loss corresponds to 0.7% for the NVX analysis and 0.8% (0.5%) for the SVX-BST (SVX-BDC) analysis. This loss is consistent with being uniform across the phase space and is applied as a global correction with a systematic uncertainty of size equal to the correction.

The efficiencies of the electron identification requirements (cluster shape, hadronic fraction, BDC or BST validation) for high energies of the scattered electron are evaluated using events passing all other selection cuts but the one to be investigated. This direct approach is applicable for  $E'_e > 20$  GeV due to the negligible background.

For low  $E'_e$ , the electron identification efficiency is studied after the background subtraction. In addition, special background-free samples are used. One such sample comprises initial state radiation events with the radiated photon detected in the photon tagger. Background levels below 1% are achieved in this case, even for  $E'_e \sim 3$  GeV, by requiring the sum of the photon tagger and scattered electron energies to be close to the electron beam energy. The efficiency of the electron identification cuts does not vary much as a function of  $E'_e$ . It is always above 90% and is well reproduced by the simulation.

The efficiency to find a central tracker vertex for the BDC analysis is determined using events with a reconstructed BST vertex. As shown in Fig. 7, it is larger than 50% for  $y_\Sigma > 0.03$  and 93% for  $y_\Sigma > 0.1$ . The BDC analysis is restricted to  $y_\Sigma > 0.03$ . At larger values of  $y_\Sigma$  the efficiency decreases again, the effect being more pronounced in the data than in the simulation. The reason for this difference is a deficit of events with a large rapidity gap in the DJANGO model, as already observed in [35]. This is accounted for by applying a correction to the MC simulation. The systematic error of the cross section resulting from this correction is found to decrease with increasing  $Q^2$ , from 10% to 2%.

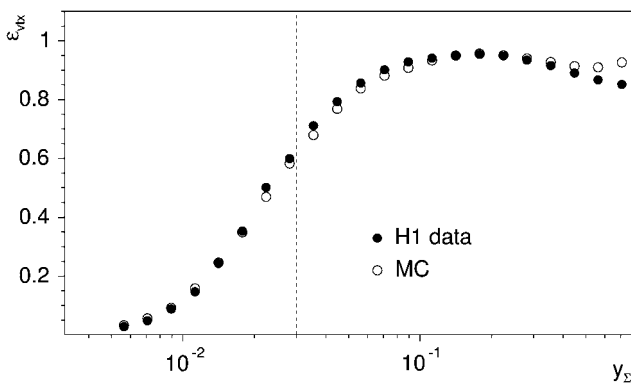


**Fig. 7** Central Tracker vertex reconstruction efficiency as a function of  $y_\Sigma$ . The dashed line corresponds to the applied selection criterion,  $y_\Sigma > 0.03$ . In the analysis the cross section at high  $y$  is measured with  $y_e$  instead of  $y_\Sigma$

A special procedure is developed to determine the BST inefficiency. Two main sources of inefficiency are distinguished which are both closely related to the readout procedure. The first is a hit finding inefficiency, which mostly depends on the performance of the front-end amplifier readout chip (APC). This efficiency is determined for each APC using BST tracks, requiring hits reconstructed in all but the BST plane under investigation. For most of the APCs the efficiency is high ( $>95\%$ ), but about 5% of APCs have efficiencies below 80%. A few BST regions, with an APC efficiency below 40%, are excluded from the analysis.

Correlated readout losses constitute the second source of inefficiency. In this case, signals are lost coherently in either BST1, BST2 or in both modules. The main source of coherent losses comes from timing desynchronisation at a level of about 5% with some dependence on the  $\phi$  sector. The coherent losses are measured separately and combined for BST1 and BST2 for each  $\phi$  sector. They are measured using a background-free DIS sample ( $15 \text{ GeV} < E'_e < 32 \text{ GeV}$ ) with a well reconstructed CT vertex and BDC track. All sources of BST losses are incorporated into the simulation.

The efficiency of the BST track segment finder, used to reconstruct the event vertex within the nominal  $z$  range and to validate the SpaCal electron candidate, is checked globally for data and for the DJANGO simulation using events with a well reconstructed central vertex and a BDC track segment. The photoproduction background is suppressed by demanding  $E'_e > 15$  GeV. In this procedure not only is the BST efficiency examined, but the description of the BST acceptance and the imperfections of the tracking algorithm are also checked. Figures 8 and 9 show the global BST efficiency as a function of the electron candidate’s radial position in the SpaCal for the NVX and SVX samples, respectively. Based on this comparison, the systematic uncertainty attributed to the description of the BST efficiency is taken to be 2% in both the NVX and the SVX data analyses. This

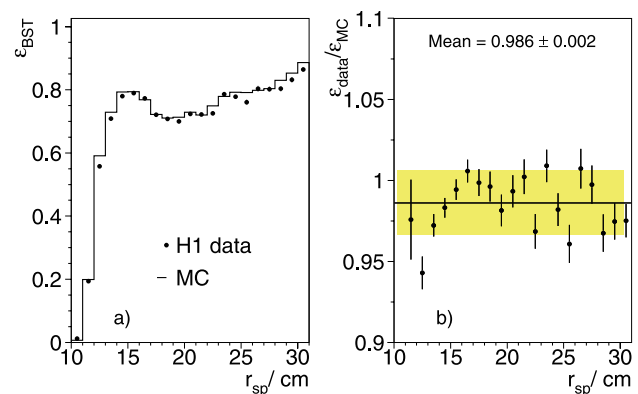


**Fig. 8** (a) BST track segment finding efficiency as a function of the radial position of the electron candidate in the SpaCal, for the NVX data sample, (b) ratio of data to MC efficiencies

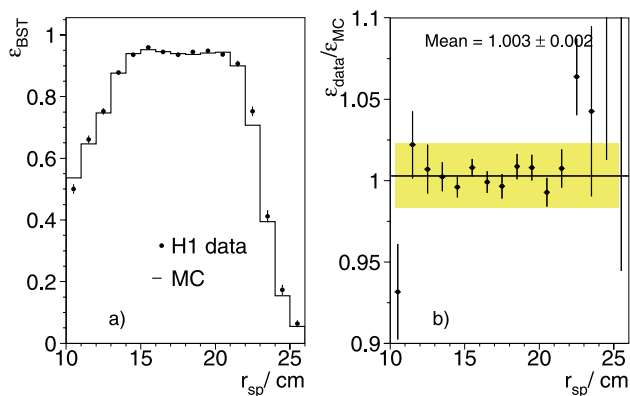


**Fig. 9** (a) BST track segment finding efficiency as a function of the radial position of the electron candidate in the SpaCal, for the SVX sample, (b) ratio of data to MC efficiencies

value also includes uncertainties arising from inefficiencies of the other electron identification criteria described above.

The efficiency of the selection criteria based on the BDC,  $N_{\text{link BDC}} \geq 4$  and  $|\Delta r_{\text{BDC-SpaCal}}| < 1.5$  cm, is determined for events with  $E'_e > 20$  GeV for data and for the DJANGO simulation. A correction to the simulated events is applied to account for discrepancies which are largest in the narrow transition region from small to large cells in the BDC. Events in this region are rejected from the NVX-S9 analysis. The systematic uncertainty attributed to the BDC efficiency amounts to 1.5%, also covering differences between data and the MC simulation for other electron selection criteria.

## 8.2 Subdetector alignment and calibration

### 8.2.1 Alignment

**Alignment of the central tracker, BDC and SpaCal** The relative alignment of the H1 sub-detectors and the alignment of the detector with respect to the beam direction is performed in several steps. The first step is the internal alignment of the Central Tracker. The  $x$  and  $y$  coordinates are defined by the precisely known positions of the CJC wires while the  $z$  coordinate is defined by the COZ. Using cosmic muon tracks, the relative positions of the inner and the outer CJC parts, the location of the CIZ and the parameters for the  $z$  coordinate measurement in the CJC are determined. The beam axis is reconstructed by measuring the  $x$  and  $y$  coordinates of the interaction vertex as functions of its  $z$  coordinate.

The alignment of the SpaCal and of the BDC is performed using high energy electron candidates, with  $E'_e > 20$  GeV, linked to a central track. The central track is required to have at least two reconstructed CIZ hits and the  $\theta$  uncertainty must be smaller than 2 mrad. The  $x$  and  $y$  offsets of the BDC and the SpaCal are measured by studying the difference in the polar angle measurements for these

electron candidates between the Central Tracker and the BDC,  $\Delta\theta = \theta_{\text{CT}} - \theta_{\text{BDC}}$ , and between the azimuthal angle measurements from the Central Tracker and the SpaCal,  $\Delta\phi = \phi_{\text{CT}} - \phi_{\text{SpaCal}}$ , as functions of the azimuthal angle  $\phi_{\text{SpaCal}}$ . The two methods find a consistent alignment in the  $x$  direction. For the  $y$  direction, the alignment is found to be different by 2 mm between the  $\Delta\theta$  and  $\Delta\phi$  methods. The average of the two values is used to correct for the misalignment.

The  $z$  offset of the BDC is measured by studying  $\Delta\theta$  versus  $\theta_{\text{CT}}$ . The  $z$  offset of the SpaCal is checked by comparing the  $\theta$  measurements in the BDC and in the SpaCal. The tilts of the backward detectors are studied using  $\Delta\theta$  versus  $\theta_{\text{CT}}$  for positive and negative  $x$  and  $y$  separately; they are found to be negligible. Figure 10 shows the comparison of the  $\theta_e$  measurement in the Central Tracker and the BDC after alignment.

The SpaCal alignment with respect to the beam direction is cross-checked using quasi-elastic QED Compton (QEDC) events. These are  $ep$  scattering events of the type  $ep \rightarrow ep\gamma$  with a hard photon radiated from the lepton line, the proton being scattered quasi-elastically at low momentum transfer such that the outgoing electron and photon are detected in the main detector, nearly back-to-back in azimuth. The QEDC process is selected by requiring two energy deposits in the electromagnetic SpaCal section with energies above 4 GeV. The sum of both cluster energies is required to exceed 25 GeV. The back-to-back requirement is enforced by demanding  $\cos \Delta\phi_{e\gamma} < -0.9$  with  $\Delta\phi_{e\gamma}$  being the azimuthal angle between the electron and the photon. Elastic events are selected by demanding no tracks reconstructed in the CJC and low activity in the calorimeters apart from the selected electron and photon. This alignment agrees within 1 mm with the alignment obtained using central tracks.

The dominant uncertainty of the alignment stems from the difference in the  $y$  direction between the  $\Delta\theta$  and  $\Delta\phi$

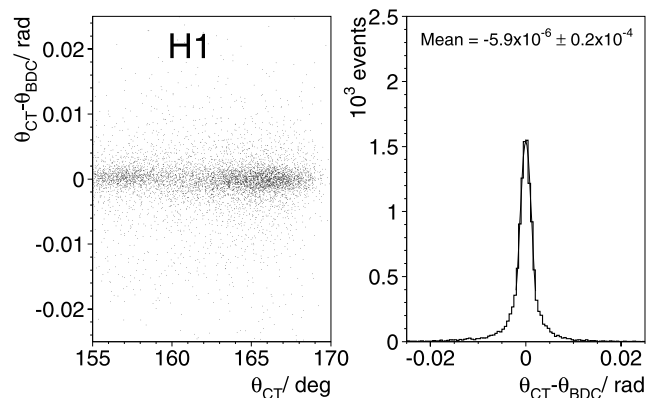


**Fig. 10** Relative alignment of the Central Tracker (CT) and BDC. Left:  $\theta_{\text{CT}} - \theta_{\text{BDC}}$  versus  $\theta_{\text{CT}}$  after alignment. Right:  $\theta_{\text{CT}} - \theta_{\text{BDC}}$  after alignment



methods. Since the H1 detector is nearly  $\phi$  symmetric, biases in the  $y$  coordinate reconstruction do not lead to large shifts in the measured cross section. To cover a potential global bias of the  $\theta_e$  measurement, a systematic uncertainty of 0.5 mrad is assigned for the polar angle reconstruction with the BDC and the Central Tracker.

**BST alignment** In the global BST alignment, the position of the BST is determined with respect to the H1 coordinate system. In the internal BST alignment, radial offsets and rotations around the  $z$  axis of the individual wafers are determined. The global and internal alignments use the electron track reconstructed from the Central Tracker vertex and the BDC track segment as a reference and compare it to the track segment found in the BST.

During the detector assembly each sensor is fixed to its nominal position with a mechanical precision of about 100  $\mu\text{m}$ . Remaining degrees of freedom are 128 radial shifts and 128 rotations of the wafers. For the  $r$  strip sensors, these parameters are determined for all detectors simultaneously using the global minimisation package Millepede [84]. The degeneracy between shifts and rotations is resolved utilising the wafer overlap regions. Typical shifts are less than 200  $\mu\text{m}$  and most rotations are less than 1 mrad. Figure 11(a) shows the distribution of the number of BST linked hits as a function of  $\phi_e$ . Figure 11(b) shows the difference in the  $\theta_e$  measurement between the two BST overlapping sectors in these cases, after the BST alignment. An agreement to better than 0.2 mrad is observed. Based on this study, the uncertainty on the scattered angle reconstruction by the BST is taken to be 0.2 mrad.

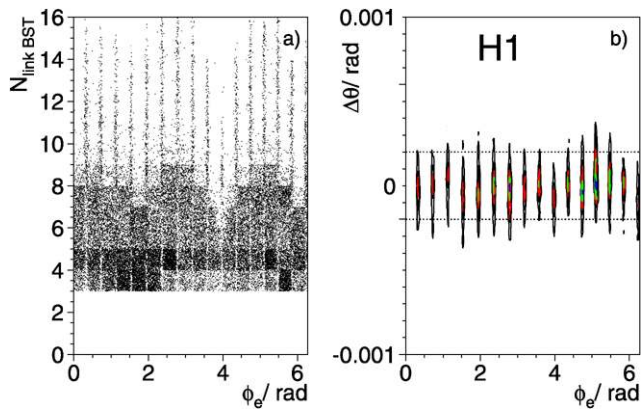


**Fig. 11** (a) Scatter plot of the number of BST hits linked to the electron candidate BST track as a function of the azimuthal angle  $\phi_e$  determined by the associated SpaCal cluster. At least three linked hits are required to define a track. A number of linked hits exceeding eight corresponds to a track passing the azimuthal BST wafer overlap region; (b) Contours of equal density for the distribution of  $\Delta\theta = \theta_1 - \theta_2$ , where  $\theta_{1,2}$  are the polar angles measured in the two overlapping BST sectors, as a function of  $\phi_e$ . The horizontal dotted lines indicate  $\pm 0.2$  mrad as is used for the systematic uncertainty of the alignment

The alignment of the  $u$  strip detector is done in an analogous way. Here, shifts perpendicular to the  $u$  coordinate for the 8 wafers are determined simultaneously using the interaction vertex and the BDC measurement as additional external constraints. The shifts of up to about 100  $\mu\text{m}$  are included in the external alignment.

### 8.2.2 Electromagnetic energy calibration

The largest uncertainty in the electromagnetic energy calibration stems from fluctuations of the gain factors of the individual SpaCal photomultiplier tubes. During the data taking, an initial cross calibration of the SpaCal cells was performed using cosmic muons. The stability of the gains was controlled by means of a dedicated LED system. First corrections to the gain factors were applied using DIS events based on the position of the “kinematic peak”—an enhancement in the  $E'_e$  distribution close to the electron beam energy which is characteristic of DIS at low  $Q^2$  at HERA.

At the analysis stage, a cell-by-cell gain determination is performed using the double angle (DA) calibration. The DA method is also used to perform additional non-uniformity corrections taking into account variations of the energy scale on the sub-cell size level. The SpaCal energy non-linearity, caused particularly by the energy losses in dead material in front of the calorimeter, is modelled in detail [85] using the H1 detector simulation based on the GEANT program [77]. The simulation is checked and corrected using  $\pi^0 \rightarrow \gamma\gamma$  decays. Finally, the energy scale is checked using  $J/\psi \rightarrow ee$  decays and QED Compton events. All calibration steps are described in the following.

**Double angle calibration** The double angle calibration procedure makes use of kinematic peak events. Large statistics are available in this kinematic domain with negligible background contamination. For  $y < 0.1$  the hadronic methods of  $y$  reconstruction (see (13) and (14)) have superior resolution. In particular, the scattered electron energy can be re-expressed in terms of the hadronic (see (17)) and electron scattering angles as

$$E_{\text{DA}} = \frac{E_e(1 - y_{\text{DA}})}{\sin^2 \frac{\theta_e}{2}}, \quad y_{\text{DA}} = \frac{\tan \frac{\theta_h}{2}}{\tan \frac{\theta_h}{2} + \tan \frac{\theta_e}{2}}. \quad (20)$$

In this method the scattered electron energy is calibrated to the electron beam energy.<sup>5</sup> The calibration corrects for genuine miscalibration and also energy loss in the dead material between the interaction point and the calorimeter. The same calibration procedure is applied separately to the data and the simulated events.

<sup>5</sup>The influence of initial state radiation, which effectively reduces the electron beam energy, is small for this kinematic selection and is included in the simulation.

For the calibration, events with  $E'_e > 20$  GeV are selected. The event vertex position and the scattered electron angle are measured using the BST. A good  $E_{DA}$  resolution is achieved by requiring  $15^\circ < \theta_h < 80^\circ$ . The calibration is performed by adjusting the gain factors of the individual SpaCal cells, such that the energy of the cluster agrees with the reference given by  $E_{DA}$ . This is achieved in an iterative procedure: for each selected event, a ratio  $c_{ev} = E_{DA}/E'_e$  is calculated. The cluster energy is usually shared among several cells; the contribution of each cell with an energy  $E_i$  is given by  $W_i = E_i/E'_e$ . A  $W_i$  weighted average of  $c_{ev}$  for each calorimeter cell is then calculated based on all calibration events. This average is used to modify the gain factor at the next iteration. The calibration procedure converges after three iterations.

The cell-by-cell calibration is followed by calibrations as a function of (i) the distance between the centre-of-gravity of the cluster and the centre of the cell with highest energy to correct for biases of the clustering algorithm, (ii)  $R_{box} = \max(|x_{sp}|, |y_{sp}|)$ , where  $x_{sp}$ ,  $y_{sp}$  are the  $x$  and  $y$  cluster coordinates, in order to correct for energy losses in between SpaCal cells, and (iii)  $r_{sp} = \sqrt{x_{sp}^2 + y_{sp}^2}$ , to correct for losses in the dead material in front of the calorimeter. These additional corrections are applied sequentially.

The results of the double angle calibration are checked by comparing the distribution of the electron energy  $E'_e$  in the data and the simulation for the standard selection in the kinematic peak region. By comparing the widths of these distributions an additional Gaussian smearing of 1.1% (0.2%) is applied to the electron energies in the simulated events for the NVX (SVX) data set. The need for this smearing in the MC may be due to short time scale drifts of the photomultiplier gain factors which are not simulated, to imperfections in the shower shape simulation or to a deficiency in the passive material simulation. For the NVX sample, the kinematic peak comparison is presented in Fig. 12(a). Fig.

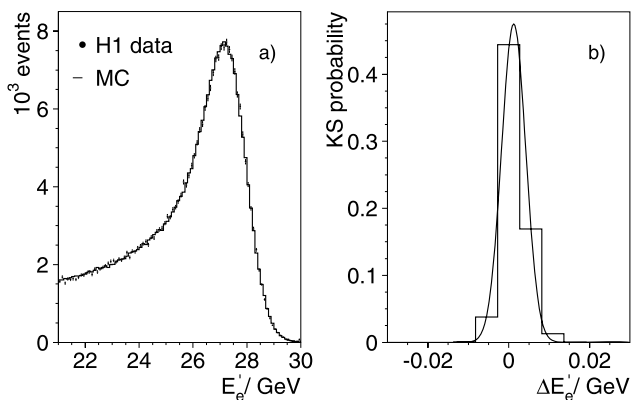


**Fig. 12** (a) Distribution of the scattered electron energy  $E'_e$  for the NVX data sample; (b) Kolmogorov-Smirnov test probability distribution as a function of the relative shift in the measured and simulated energy distributions

ure 12(b) shows the Kolmogorov-Smirnov (KS) test probability distribution as a function of the relative shift in the energy distribution between the data and the simulation. Shifts above 20 MeV are excluded, which corresponds to a relative energy scale agreement better than 0.1%. The systematic uncertainty on the relative energy scale at the kinematic peak is taken to be 0.2% to account for the uncertainties of the HERA beam energy, for uncertainties in the resolution adjustment in the simulation, deficiencies of the double angle method and a residual variation of the level of agreement in the kinematic peak between data and MC for different  $Q^2$  bins.

**Calibration using  $\pi^0 \rightarrow \gamma\gamma$**  The double angle energy calibration determines the energy scale of the individual SpaCal cells and radially dependent corrections of the energy loss for scattered electron energies close to the electron beam energy. The deviations from the linearity of the SpaCal response are measured using  $\pi^0 \rightarrow \gamma\gamma$  decays which probe much lower energies.

Events with two clusters in the electromagnetic SpaCal section are selected. The larger of the two cluster energies is required to be above 2.2 GeV, exceeding the trigger energy threshold, the smaller cluster energy is required to be above 0.7 GeV. The event vertex is determined from tracks reconstructed in the Central Tracker. The two clusters are assumed to be produced by two photons. The invariant mass,  $M_{\gamma\gamma}$ , is calculated using the reconstructed cluster energies and positions.

The simulation of  $\pi^0 \rightarrow \gamma\gamma$  decays is checked using the PHOJET MC sample. A reasonable agreement of the simulation with the data is observed for the total energy of the two clusters as shown in Fig. 13(a). The simulated  $\pi^0$  energy spectrum is reweighted to that observed in the data, in order to reproduce the opening angle and individual photon energy distributions.

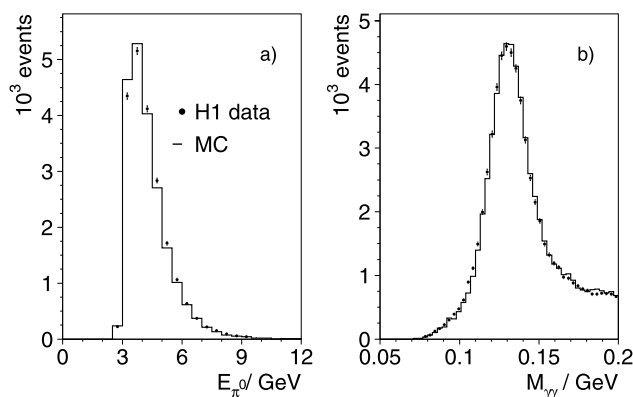


**Fig. 13** (a) Energy distribution for  $\pi^0$  candidates based on the NVX sample as triggered by the low energy trigger, S9; (b) di-photon invariant mass distribution for  $\pi^0$  candidates. The double angle calibration constants are applied to the data and MC simulation

The two-photon mass distribution is shown in Fig. 13(b). A prominent peak above the background is observed close to the nominal  $\pi^0$  mass. The peak is shifted to lower values, around 130 MeV instead of 135 MeV. This difference is not reproduced by the MC simulation after the double angle calibration. The figure shows the distribution of simulated events after applying an additional correction of  $-3\%$  to the energy scale for them. The data and the simulation are then in a good agreement. The shift of the peak is possibly caused by not fully simulated energy losses in the dead material in front of the calorimeter.

The low  $\gamma\gamma$  invariant mass and the relatively high photon energy cuts in the study of  $\pi^0 \rightarrow \gamma\gamma$  decays lead to a rather small separation between the photon clusters in SpaCal, with an average separation of only 13 cm. An overlap of the adjacent clusters could lead to an energy scale shift. Additional studies are performed to estimate this effect. The data sample is split into sub-samples with approximately equal statistics based on the larger or smaller cluster energy or on the cluster separation. In addition, the  $M_{\gamma\gamma}$  distribution is studied as a function of the projected  $\pi^0$  location in the calorimeter, the latter being calculated as an energy weighted sum of the two cluster positions. In all these studies the relative shifts of the energy scale in the data versus the simulation are consistent within 1% which is taken as a systematic uncertainty of the energy determination at  $E'_e = 2$  GeV.

A check of the relative energy scale using  $\pi^0$  decays is also performed for the SVX sample. The larger distance from the decay vertex to the calorimeter leads to larger separations between photon clusters, on average 18 cm. The relative shift of the  $M_{\gamma\gamma}$  distribution between the data and the simulation after the double angle calibration is  $-2.7\%$  in this case, consistent with the shift observed for the NVX sample.

The relative bias of the energy scale is corrected in the data assuming a linear dependence on  $E'_e$ . No correction is applied at  $E'_e = 27.6$  GeV and a correction of  $+3\%$  is applied at  $E'_e = 2$  GeV. The systematic uncertainty of the energy scale determination is also assumed to follow a linear dependence rising from 0.2% at  $E'_e = 27.6$  GeV to 1% at 2 GeV.

*Tests of the SpaCal energy calibration* The SpaCal energy response is checked using  $J/\psi \rightarrow ee$  decays and QED Compton  $ep \rightarrow ep\gamma$  events. The  $J/\psi$  candidates are selected by requiring exactly two electromagnetic clusters with a total energy of less than 22 GeV. At least one of the two clusters has to be linked to either a BST or a CJC track and both clusters must be associated with a BDC track segment. Events with additional CJC tracks not associated to the electrons are rejected, thus selecting events from elastic  $J/\psi$  production. The event vertex is defined by the CJC or the BST tracks.

In this study, the SpaCal energy measurement is explicitly corrected to the absolute scale obtained from the mean ratio of the reconstructed to the generated electron energy from the DJANGO simulation. Both the double angle and  $\pi^0$  calibration corrections are applied, so that the peak in the di-electron invariant mass  $M_{ee}$  distribution can be directly compared to the nominal  $J/\psi$  mass,  $M_{J/\psi} = 3.096$  GeV.

The distribution of  $M_{ee}$  for the NVX data is shown in Fig. 14. A clear enhancement around the nominal  $J/\psi$  mass is observed. The data are fitted with a sum of a Gaussian for the signal peak and a second order polynomial to describe the background shape. The fit uses the binned maximum likelihood method. The measured Gaussian peak position agrees with  $M_{J/\psi}$  within  $1.3\sigma$ . Based on this agreement the deviation from the nominal energy scale is limited to be below 0.8% at 68% confidence level for energies of about 6 GeV.

QED Compton events are used to check the calorimeter energy scale in the intermediate energy region. For elastic events, the energy of the scattered electron is related [86] to the polar angles of the scattered electron  $\theta_e$  and the photon  $\theta_\gamma$  by

$$E_{\text{QEDC}}^{\text{DA}} = \frac{2E_e \sin\theta_\gamma}{\sin\theta_e + \sin\theta_\gamma - \sin(\theta_e + \theta_\gamma)}. \tag{21}$$

The comparison of the measured electron energy with  $E_{\text{QEDC}}^{\text{DA}}$  tests the SpaCal energy scale linearity in the range 4–23 GeV.

For the QED Compton energy scale check, a bias free reconstruction of the electron and photon angles is essential. Therefore in addition to the basic QEDC event selection described in Sect. 8.2.1, both electron and photon SpaCal clusters are required to be linked to BDC track segments. This implies that the photon converted in the detector material in front of the BDC. The electron cluster is identified by requir-

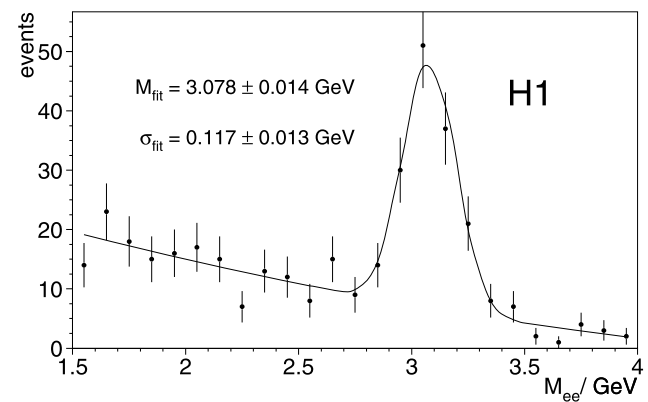


**Fig. 14** Invariant mass distribution of the two electron candidate tracks for a special  $J/\psi$  event selection. The line indicates a fit to the data.  $M_{\text{fit}}$  and  $\sigma_{\text{fit}}$  correspond to the Gaussian mean and width of the peak

ing a BST link. The photon cluster must have no associated signals, neither in the BST nor in the CIP.

The results of all calibration studies are summarised in Fig. 15. Both the  $J/\psi$  and the various QEDC energy scale determinations are inside the uncertainty band. The scattered electron energy distributions and the uncertainty bands attached to the simulated  $E'_e$  distributions in the kinematic peak region are shown in Fig. 16 for the NVX and the SVX analyses. The data are well described by the simulations.

### 8.2.3 Calibration of the hadronic energy scale

The calibration of the calorimeters employed for the hadronic final state energy measurement is based on kinematic constraints relating the scattered electron to the hadronic final state. For the calibration of the LAr calorimeter, conservation of the total transverse momentum  $P_T$  is used. The SpaCal calibration makes use of the conservation of  $E - P_z$ .

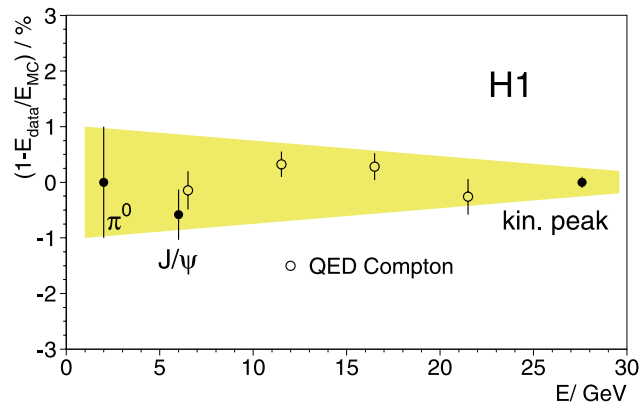


**Fig. 15** Summary of SpaCal energy scale determination. The band indicates the uncertainty due to the scale difference between the data and the simulation

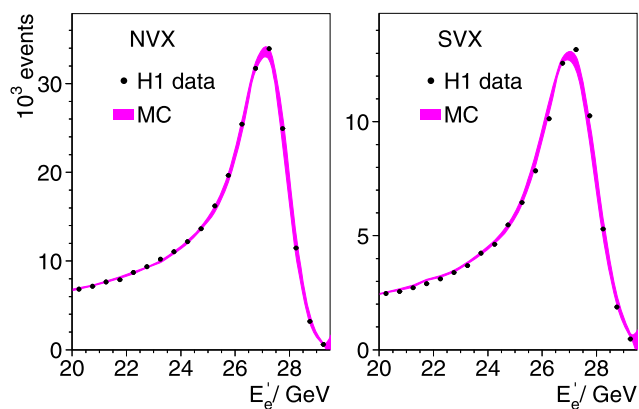


**Fig. 16** Distributions of the scattered electron energy  $E'_e$  for the data and the MC simulation in the NVX (left) and the SVX (right) analyses. The MC bands include the statistical uncertainty and the effect of a  $\pm 0.2\%$  electromagnetic energy scale variation

**Calibration of the LAr calorimeter** The hadronic final state in the central and forward regions of the H1 detector is reconstructed using a combination of tracks and LAr energy deposits (see Sect. 6.4). The LAr calibration coefficients are determined for the eight calorimeter wheels, each subdivided into eight octants, separately for the hadronic and electromagnetic sections. There are thus 120 calibration constants in total,<sup>6</sup> corresponding to the calorimeter segmentation in rapidity, azimuthal angle, and depth. The same calibration procedure is applied to the data and the MC simulation.

To reduce the influence of the SpaCal on the calibration of the LAr, forward and central hadronic angles are selected:  $13^\circ \leq \theta_h \leq 150^\circ$ . The electron transverse momentum  $P_T^e$  is determined from the SpaCal energy and the  $\theta_e$  measured by the BST. The photoproduction background is reduced to a negligible level by requiring  $E'_e > 20$  GeV.

In the calibration procedure, a least squares minimisation of the following function is performed

$$\mathcal{L}(\alpha_j) = \sum \left( P_T^e - \left| \mathbf{P}_T^{\text{Tr}} + \mathbf{P}_T^{\text{Sp}} + \sum_j \alpha_j \mathbf{P}_T^j \right| \cdot |\cos(\phi_e - \phi_h)| \right)^2 \quad (22)$$

Here the transverse momenta  $\mathbf{P}_T^{\text{Tr}}$  and  $\mathbf{P}_T^{\text{Sp}}$  are the vector sums of the contributions from the tracks and the SpaCal, respectively,  $\mathbf{P}_T^j$  are the vector sums of the contributions from all cells of a calorimeter volume  $j$ ,  $\phi_h$  is the azimuthal direction of the hadronic final state and  $\alpha_j$  are the calibration coefficients, which are free parameters. The outer summation is performed over all DIS events selected for the calibration.

The  $P_T$  balance between the scattered electron and the calibrated hadronic final state is studied as a function of various variables, such as  $P_T^e$ ,  $\theta_h$  and  $y_\Sigma$ . For central events, where  $y_\Sigma \geq 10^{-2}$ , the simulation reproduces the behaviour of the data within 2% accuracy. At lowest  $y$ , the hadronic final state is produced at small polar angles and partially escapes the LAr acceptance. In this case, simulation and data agree within 10%. The systematic uncertainty of the hadronic scale is therefore extrapolated linearly in  $\log y$ , from 10% at  $y_\Sigma = 10^{-3}$  to 2% at  $y_\Sigma = 10^{-2}$ . It is then set to 2% for  $y_\Sigma \geq 0.01$ . Figure 17 shows the overall  $P_T$  balance for the standard analysis selection. The vertical line at  $P_T^h/P_T^e = 0.3$  indicates the analysis cut value. An increase in number of events for  $P_T^h/P_T^e < 0.3$  corresponds to very low  $y < 0.001$ . The data agree with the simulation within the hadronic energy scale uncertainty.

<sup>6</sup>The most backward LAr wheel does not have a hadronic section.

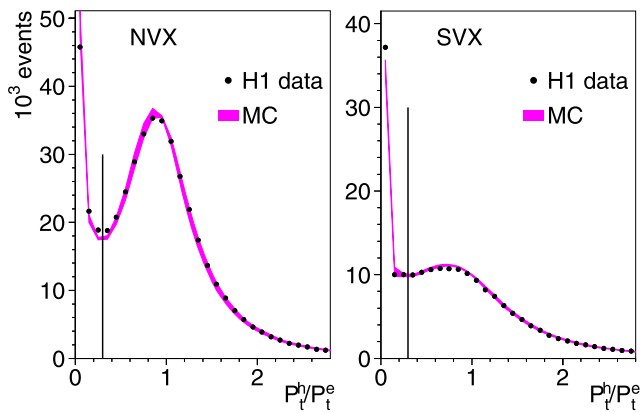


**Fig. 17** Transverse momentum balance  $P_T^h/P_T^e$  distribution for the data and the MC simulation in the NVX and the SVX analyses. The bands include the statistical uncertainty of the simulation and the effect of the LAr hadronic scale uncertainty, see description in the text. The vertical line indicates the analysis requirement  $P_T^h/P_T^e > 0.3$

**Hadronic energy calibration of the SpaCal** For large values of  $y \gtrsim 0.4$ , the contribution of the SpaCal to the total  $E-P_z$  becomes larger than the combined contribution of the LAr calorimeter and tracks. Given the accurate knowledge of the SpaCal linearity after calibration (Sect. 8.2.2), the study of  $E-P_z$  as a function of  $E'_e$  allows a check of both the linearity and the absolute scale of the SpaCal hadronic measurement to be made.

The  $E-P_z$  distribution is studied for  $E'_e > 7$  GeV in  $E'_e$  intervals of 1 GeV. For each interval, a Kolmogorov-Smirnov test is performed to estimate a possible shift in the  $E-P_z$  distribution between data and simulation. For the SVX analysis, the data and the simulation agree well within their statistical uncertainties, while for the NVX data sample a global shift of  $\sim 1$  GeV is observed. This shift is applied in the NVX analysis to the simulated events. An additional systematic uncertainty,  $\Delta(E-P_z)_{\text{SpaCal}} = 0.5$  GeV, is considered for both SVX and NVX analyses. Figure 18 shows the  $E-P_z$  distribution for the data and the simulation. The uncertainty band includes a  $\pm 0.5$  GeV variation of the SpaCal contribution to the total  $E-P_z$ .

8.2.4 Calorimeter noise uncertainty

For  $y \lesssim 0.01$ , even a small fake energy contribution in the LAr can strongly affect the determination of  $y_h$ . Therefore, a dedicated procedure is used to identify the LAr noise, as described in Sect. 6.4. Samples of LAr electronic and beam induced noise are recorded in special runs and added to the simulation.

The uncertainty of the noise influence on the DIS cross section measurement is determined as a function of  $y_h$  by studying the ratio  $y_{h,\text{noise}}/(y_h + y_{h,\text{noise}})$ , where  $y_{h,\text{noise}}$  is defined as  $y_{h,\text{noise}} = \sum_i (E_i - P_{z,i})/2E_e$  with the sum extending over the identified noise cells only. This comparison

is shown in Fig. 19 for the NVX and SVX data samples together with contributions to  $y_h$  from the tracks, LAr and SpaCal calorimeters. The noise fraction is described by the simulation within 10% accuracy which is taken as a systematic uncertainty. Note that at high  $y$  the noise fraction is small. More details on the LAr noise uncertainty estimation can be found in [82, 83].

8.3 Background subtraction

8.3.1 Methods

The dominant background source for this analysis arises from very low  $Q^2$  photoproduction events in which the scattered electron escapes detection in the backward beam pipe and a particle from the hadronic final state mimics the electron. Other potential background sources arise from non-ep

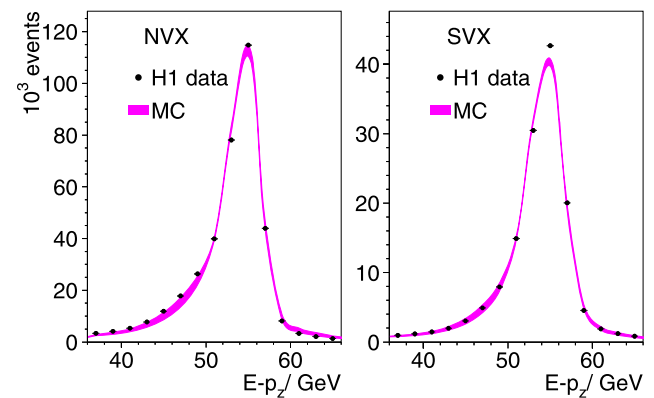


**Fig. 18**  $E-P_z$  distribution for the data and the MC simulation in the NVX and the SVX analyses. The bands include the statistical uncertainty of the simulation and the effect of a  $\pm 0.5$  GeV variation of the SpaCal hadronic final state contribution

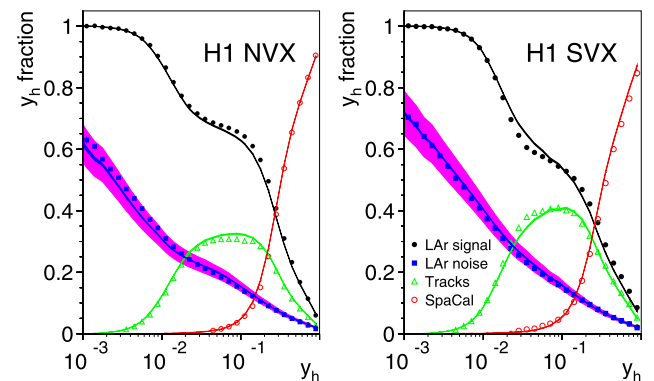


**Fig. 19** Relative contributions to the measured  $y_h$  from the LAr (closed circles), tracks (triangles) and SpaCal (open circles) together with the subtracted LAr noise fractions (squares) in the NVX (left) and SVX (right) analyses. The distributions of simulated events are shown as curves. The shaded areas correspond to a 10% systematic uncertainty on the LAr noise description

interactions. They are studied using non-colliding HERA bunches and are found to be negligible.

For a fraction of photoproduction events the scattered electron is detected by the electron tagger of the luminosity system. These events are used to study the photoproduction background. The acceptance of the electron tagger, which corresponds to the geometrical aperture of the detector as well as to the detection efficiency, is determined using Bethe-Heitler  $ep \rightarrow ep\gamma$  events [40], in which the scattered electron and the emitted photon are detected in the electron and photon tagger, respectively, and is parametrised as a function of  $y$ . The acceptance is large in the range  $0.3 < y < 0.6$ .

The simulated photoproduction background (PHOJET) is normalised based on events where the scattered electron is detected by the electron tagger and all of the analysis selection criteria<sup>7</sup> are satisfied. Two normalisation methods are used. In the first method the background is normalised globally and then subtracted bin-by-bin

$$N_{\gamma p}^i = N_{\text{bg MC, tag}}^i \cdot \frac{N_{\text{tag}}}{N_{\text{bg MC, tag}}}, \quad N_{\text{DIS}}^i = N_{\text{data}}^i - N_{\gamma p}^i. \quad (23)$$

Here,  $N_{\text{DIS}}^i$  ( $N_{\gamma p}^i$ ) is the estimated number of DIS (photoproduction) events in the cross section measurement bin  $i$ ,  $N_{\text{data}}^i$  and  $N_{\text{bg MC}}^i$  are the numbers of data and PHOJET events in bin  $i$ , respectively, and  $N_{\text{tag}}$ ,  $N_{\text{bg MC, tag}}$  are the total numbers of events detected using the electron tagger in the data and the PHOJET simulation, respectively.

In the second method the background is normalised bin-wise using the bin-averaged tagger acceptance  $A_i$  and then subtracted in each bin

$$A_i = \frac{N_{\text{bg MC, tag}}^i}{N_{\text{bg MC}}^i}, \quad N_{\text{DIS}}^i = N_{\text{data}}^i - \frac{N_{\text{tag}}^i}{A_i}, \quad (24)$$

where  $N_{\text{tag}}^i$  and  $N_{\text{bg MC, tag}}^i$  are the numbers of events detected by the electron tagger in bin  $i$  in the data and the PHOJET event sample, respectively. Both methods lead to a cancellation of global selection uncertainties, while the second method (see (24)) also allows local uncertainties to cancel at the expense of an increased statistical uncertainty.

For the NVX-S9 analysis, the global normalisation of the background (see (23)) is used, since for this sample the  $E_e'$  and  $\theta_e$  distributions are well reproduced by the simulation (Fig. 20). Furthermore there is a direct control of the background normalisation as discussed in the next section. For

<sup>7</sup>For the electron method, this selection excludes the  $E-P_z$  cut in order to increase the electron tagger acceptance. In addition, to reduce the influence of overlapping DIS and Bethe-Heitler events, the absence of energy deposits in the photon tagger is required, and the total  $(E-P_z)_{\text{tot}} = E-P_z + 2E_{\text{tagger}}^e$ , where  $E_{\text{tagger}}^e$  is the energy measured in the electron tagger, has to be less than 75 GeV.

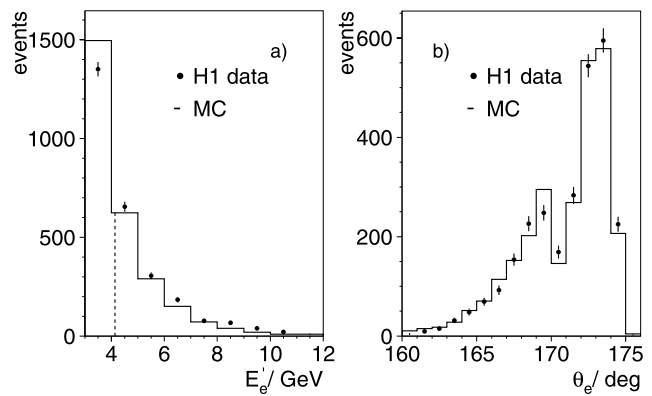


**Fig. 20** Distribution of  $E_e'$  (a) and  $\theta_e$  (b) for photoproduction events detected in the electron tagger. The plots are based on the NVX-S9 analysis. The *dashed line* in (a) corresponds to the minimum  $E_e'$  permitted by the analysis cut  $y_e < 0.85$

the other analyses, a local bin-wise normalisation is performed. As a cross check, both normalisation methods are used for all samples, leading to cross section results consistent within statistical uncertainties.

### 8.3.2 Normalisation uncertainty

The photoproduction background normalisation is checked for the NVX-S9 analysis using electron candidates associated with tracks of opposite charge to the lepton beam charge, termed “wrong charge” tracks. Assuming charge symmetry of the background tracks, the wrong charge track sample gives an estimate of the remaining background in the correct charge sample. The track charge can be measured for tracks which are reconstructed in the BST sector equipped with  $u$  strip detectors in addition to the  $r$  detectors.

In this method, any charge asymmetry creates a bias. In addition, the requirement of a  $u$  strip track in the background study could modify the normalisation compared to the standard sample. The geometrical acceptance and efficiency  $\epsilon$  of the  $u$  strip track reconstruction are first determined based on a high  $E_e'$  sample in which the background can be neglected. The acceptance and efficiency are well described by the simulation. The acceptance difference between data and simulation is found to be  $(2.0 \pm 1.3)\%$ , while the efficiency difference is determined to be  $(0.2 \pm 0.5)\%$ .

All events within the  $u$  sector acceptance passing the NVX-S9 analysis cuts,  $N_{\text{acc}}$ , are classified according to  $N_{\text{acc}} = N_0 + N_+ + N_-$ , where  $N_0$  denotes all events without a linked  $u$  track,  $N_+$  is the number of all events with correct sign tracks (positive, as expected from the scattered positron) and  $N_-$  is the number of all events with wrong sign tracks. If  $\kappa = N_+^{\text{bg}}/N_-^{\text{bg}}$  is the background charge asymmetry ratio, then the total number of background events in the

$u$  sector geometrical acceptance is

$$\begin{aligned}
 N_{\text{bg}} &= N_{\text{acc}} - N_{\text{sig}} = N_{\text{acc}} - \frac{N_+ - \kappa N_-}{\epsilon} \\
 &= N_0 + N_- \left(1 + \frac{\kappa}{\epsilon}\right) + N_+ \left(1 - \frac{1}{\epsilon}\right). \tag{25}
 \end{aligned}$$

Here  $N_{\text{acc}}(N_{\text{sig}})$  denotes the number of accepted (genuine DIS signal) events.

The charge asymmetry of the background for the PHOJET simulation is found to be  $\kappa = 0.79 \pm 0.06$ . A dedicated study of the origin of this asymmetry [37] showed that the main effect is due to the difference between the proton and antiproton interaction cross sections and the visible energy which they deposit in the SpaCal. A larger value of  $|E/p|$  is expected for antiprotons since they annihilate at the end of their paths. Indeed, for simulated events with  $|E/p| > 2$  the deviation of  $\kappa$  from unity is larger:  $\kappa = 0.60 \pm 0.14$ . From the data with  $|E/p| > 2$  a consistent value  $\kappa = 0.65 \pm 0.12$  is measured.<sup>8</sup> The charge asymmetry is also checked using events in which the scattered electron is detected in the electron tagger. It is found to be  $0.82 \pm 0.17$ . The PHOJET based asymmetry estimate is also consistent with the value estimated in [37] using tagged events,  $\kappa = 0.91 \pm 0.04$ . In order to cover the findings on the charge asymmetry explained above, a value  $\kappa = 0.9 \pm 0.1$  is assumed for this analysis.

The ratio of the number of photoproduction events obtained using (25) to the estimated number of events based on the electron tagger, (23), for the  $E'_e$  range of the NVX-S9 analysis, is  $r = 1.00 \pm 0.14_{\text{stat}} \pm 0.05_{\text{asym}}$ . Here the first error gives the statistical uncertainty and the second error corresponds to the uncertainty in the background asymmetry determination. Figure 21 shows the distribution of  $E'_e$  for the background events, estimated using  $u$  sector tracks. The systematic uncertainty on the background normalisation is taken to be  $\pm 15\%$ , based on the statistical uncertainty of the  $u$  sector sample and the uncertainty in the background charge asymmetry.

### 8.4 Luminosity determination

The luminosity measurement is based on Bethe-Heitler events detected using the photon detector. A precise luminosity measurement requires a good understanding of the beam optics, of the photon detector acceptance and its variation with changing beam conditions. The uncertainties related to the acceptance are similar for the NVX and the SVX data.

The time structure of the  $ep$  bunch crossings is characterised by the main proton bunch accompanied by satellite

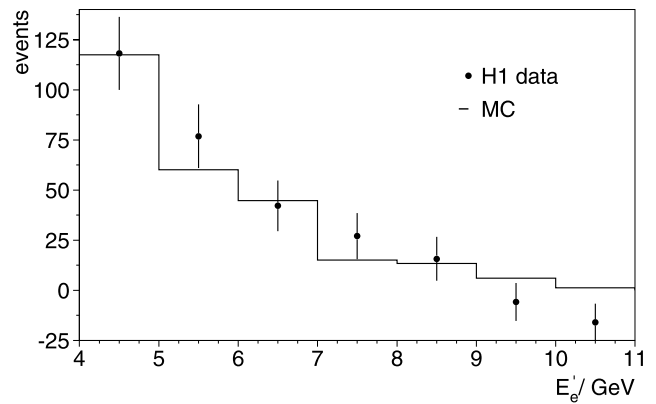


**Fig. 21** Distribution of  $E'_e$  for background events, estimated using wrong charge BST tracks (see (25)) for data and the PHOJET simulation. The simulated sample is normalised using photoproduction events with the scattered electron detected in the electron tagger

bunches. Two such bunches are at  $\pm 4.8$  ns away from the nominal bunch and lead to  $ep$  interactions at about  $\pm 70$  cm from the mean vertex position. The photon detector is sensitive in a time window of about 12 ns for Bethe-Heitler events and thus does not distinguish interactions at the nominal vertex position from satellite bunch interactions. The luminosity measurement therefore requires the fraction of satellite bunch interactions to be determined independently. This is possible in H1 using TOF and PPU systems.

For the SVX data, with the main bunch centred at  $z = 70$  cm, the backward satellite is located at  $z \sim 0$  cm. The backward satellite in this case gives a larger contribution to the luminosity measurement than the forward satellite at  $z \sim 140$  cm. The fraction of events in the backward satellite can be determined directly from the fraction of DIS events with a reconstructed vertex around  $z = 0$  cm and amounts to 2.7%. A 3% uncertainty is assigned to the luminosity measurement for the SVX data, which covers the differences observed between the methods of determining the satellite bunch fraction and also includes uncertainties related to the photon detector. The same procedure is performed to verify the contribution from the forward satellite at +70 cm of the NVX data sample. In this case the different methods are in agreement within 0.7%, leading to a total luminosity uncertainty of 1.1%.

In the course of this analysis an extended reanalysis of the 1997 data at  $Q^2 \leq 12 \text{ GeV}^2$ , this sample termed B in [37], was performed, which reproduced the published cross sections in shape. These, however, are to be multiplied by a factor of 1.034 as the result from an improved analysis of the satellite bunch structure and the photon detector acceptance. This corresponds to a shift of two standard deviations of the quoted luminosity measurement accuracy.

<sup>8</sup>At low energy, the contribution of DIS electrons with  $|E/p| > 2$  is negligible.

## 8.5 Summary of systematic uncertainties

The systematic uncertainties are classified into two groups, bin-to-bin correlated and uncorrelated systematic errors. For this analysis the correlated sources are the electromagnetic and hadronic energy scales, the electron scattering angle, the calorimeter noise, the background subtraction and the normalisation uncertainty. The uncorrelated errors are related to various efficiencies and radiative corrections. A summary of the correlated and uncorrelated errors for the present analysis is given in Table 4.

The large overall contributions to the total error are due to the BST electron track reconstruction efficiency and the Central Tracker vertex efficiency uncertainty. The correlated error sources affect the DIS cross section measurement in a manner which depends on the kinematic domain. The most pronounced variation arises with the inelasticity  $y$ . For high  $y$ , the uncertainty is dominated by the photoproduction background (about 6% for  $y = 0.8$ ). For intermediate  $y \sim 0.1$ , the  $E'_e$  scale uncertainty becomes more prominent for the electron method (about 3% cross section uncertainty). For  $y < 0.01$ , the dominant error source is the LAr noise (up to 10% cross section error).

## 8.6 Control distributions

Data and Monte Carlo simulation distributions of important quantities for the events passing all selection criteria

are compared in Figs. 22–25. Only events corresponding to analysis bins passing the stability and purity criteria are considered. The simulated distributions are normalised to the measured luminosity. The DIS MC cross section prediction is reweighted to a parameterisation using the fractal model introduced in Sect. 11.1. A rather good (NVX) to acceptable (SVX) overall agreement is obtained in the description of the data by the simulation.

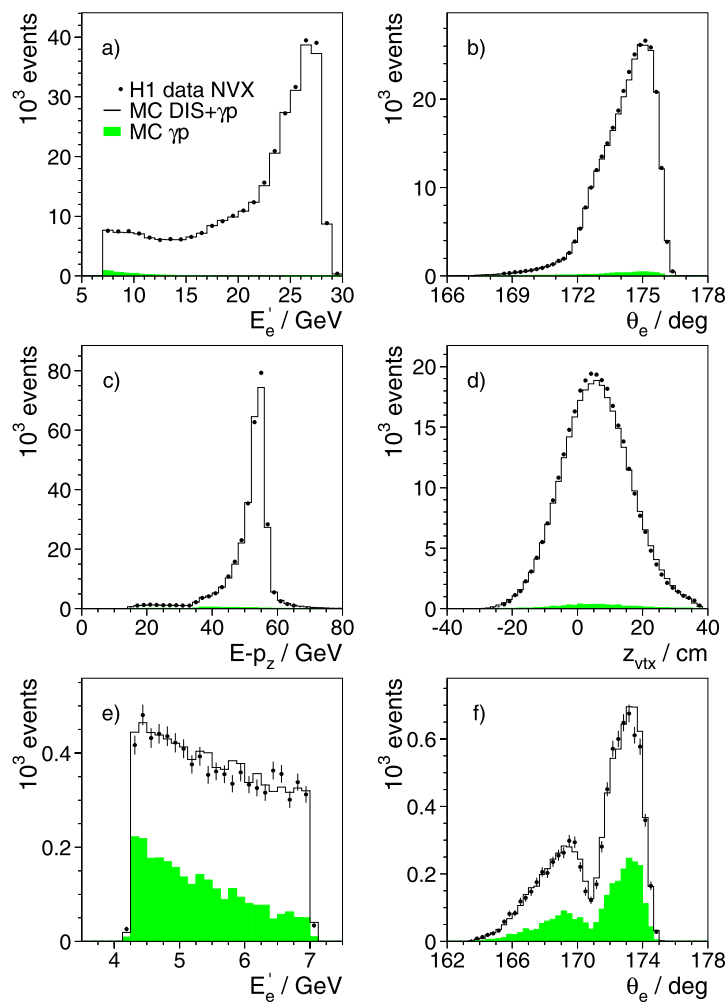
Figure 22(a–d) shows basic kinematic and vertex distributions for the NVX analysis. The background from photoproduction events is very small. It is larger at lower scattered positron energies  $E'_e$  as can be seen in Figs. 22(e) and (f), which show the  $E'_e$  and  $\theta_e$  distributions for the dedicated high  $y$  analysis (NVX-S9). In Fig. 23 basic kinematic distributions for the SVX-BST analysis (a)–(c), the SVX-BDC analysis (d) and the SVX-BST analysis considering events from ISR bins only (e), (f) are shown. The ISR distributions are very well reproduced by the simulation. The other SVX plots reveal a small normalisation difference. Figure 24 shows the  $x$  and  $Q^2$  distributions for the two kinematic reconstruction methods, electron and  $\Sigma$ , in the NVX analysis. Figure 25 shows similar distributions for the SVX analysis. Events are only taken into account from bins which pass the stability and purity criteria and are covered by the chosen method. For the SVX sample the data are less well described than for the NVX sample, but consistency is observed within the total measurement uncertainty including a 3% normalisation error of the SVX data.

**Table 4** Summary of the systematic uncertainties. For the correlated sources, the uncertainties are given in terms of the uncertainty of the corresponding source. The effect on the cross section measurement varies from bin to bin and is given in Tables 10–14. For the uncorrelated sources, the uncertainties are quoted in terms of the effect on the measured cross section directly and the type of analysis is given in brackets

Source	Uncertainty
<b>Correlated errors</b>	
$E'_e$ scale uncertainty	0.2% at 27.6 GeV to 1% at 2 GeV linear in $E'_e$
$\theta_e$ uncertainty	0.2 mrad (BST) 0.5 mrad (BDC-Central vertex)
LAr scale uncertainty	10% at $y = 0.001$ to 2% at $y = 0.01$ linear in $\log y$ 2% for $y > 0.01$
LAr noise contribution to $E-P_z$	10%
SpaCal hadronic scale	0.5 GeV
$\gamma p$ background normalisation	15%
Luminosity	3% (SVX) 1.1% (NVX)
<b>Uncorrelated errors</b>	
BST efficiency	2% (BST)
BDC efficiency	1.5% (BDC-Central vertex)
Central Tracker vertex efficiency	2–10% (BDC-Central vertex)
Trigger efficiency	0.9% (NVX) 1.1% (NVX-S9) 0.9% (SVX-BST) 0.7% (SVX-BDC)
Radiative corrections	0.5%



**Fig. 22** Distribution of events for the NVX-BST analysis: the energy (a) and the polar angle (b) of the scattered positron;  $E-P_z$  (c) and the  $z$  vertex position (d). Control distributions for the NVX-S9 analysis: energy (e) and polar angle (f) of the scattered positron candidates. The histograms represent the simulation of DIS and the photoproduction background (shaded)



### 8.7 Cross checks

The stability of the cross section measurement is tested with a set of dedicated cross checks which can be divided into three classes: (i) checks for a given data set and a given reconstruction method, (ii) checks of the consistency between the different reconstruction methods, and (iii) checks of the consistency between the different data sets.

The consistency of the cross section measurement for a given data set (e.g. NVX) and a given reconstruction method (e.g. the electron method with  $\theta_e$  measured by the BST) is studied by splitting the data into two approximately equal sub-samples and comparing these sub-samples to each other. The data are compared as measured with the upper and the lower half of the SpaCal, for negative and positive  $z$ -vertex positions, and dividing the sample into an early and late data taking period. These tests are sensitive to local effects like efficiency variation, energy miscalibrations and the stability of the luminosity measurement. In such studies no significant deficiencies in the data are observed.

For the comparison of the cross section measurements for a given data set but using different reconstruction methods, the test samples are strongly correlated. The uncorrelated statistical uncertainty is estimated in this case by subdividing the simulated events into a number of independent sub-samples of equal size. The measurement of the cross sections is repeated for each sub-sample and the statistical uncertainty is calculated as the luminosity rescaled RMS of the resulting variations of the cross section measurements. Employing this technique, the cross section measurements based on different triggers and different  $\theta_e$  reconstruction methods (BDC and BST) are compared. In most of the cases the measurements with each of the samples agree within the uncorrelated statistical uncertainty. In a few cases the measurements agree within the total uncertainty only. A particularly interesting test is the comparison of the cross section measurement performed with the electron and sigma methods, since the two methods have different sensitivities to systematic error sources. The two methods can both be applied in many common bins where the purity and stability of the

**Fig. 23** Distribution of events for the SVX-BST (a–c, e, f) and SVX-BDC (d) analyses: the energy (a) and the polar angle (b) of the scattered positron;  $E-P_z$  (c) and the  $z$  vertex position (d); the energy (e) and  $E-P_z$  (f) for the ISR bins. The histograms represent the simulation of DIS and the photoproduction background (shaded)

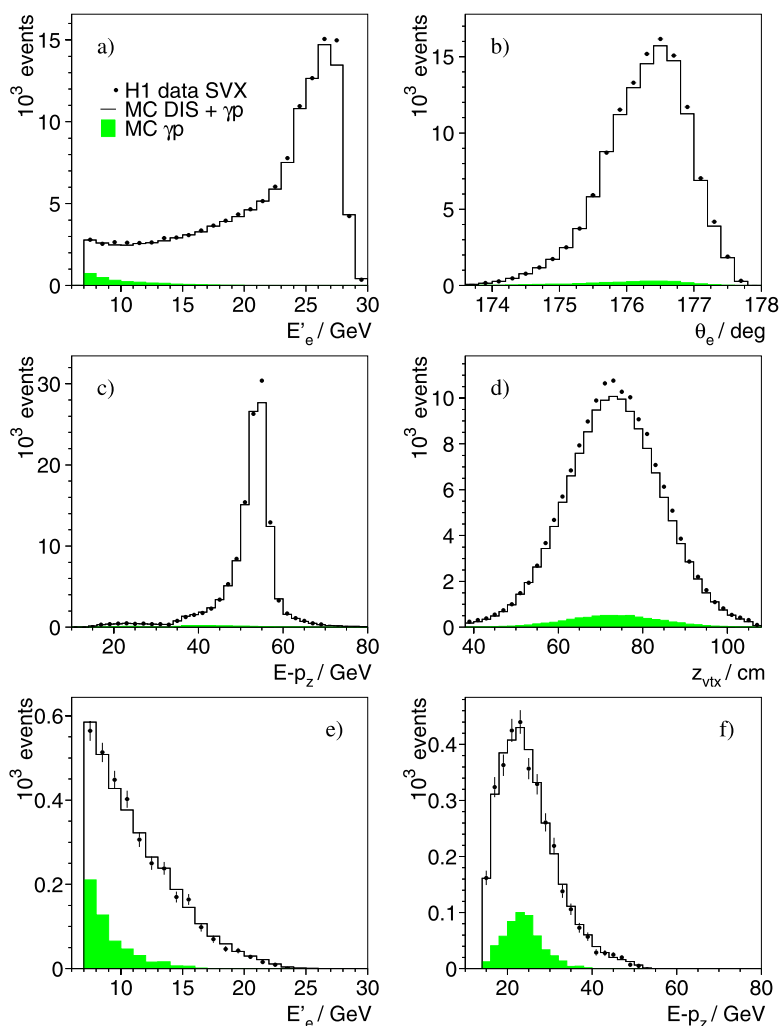


**Fig. 24** Distribution of Bjorken- $x$  and  $Q^2$  using the electron (top) and sigma (bottom) reconstruction methods for the NVX data. The histograms represent the simulation of DIS and the photoproduction background (shaded)

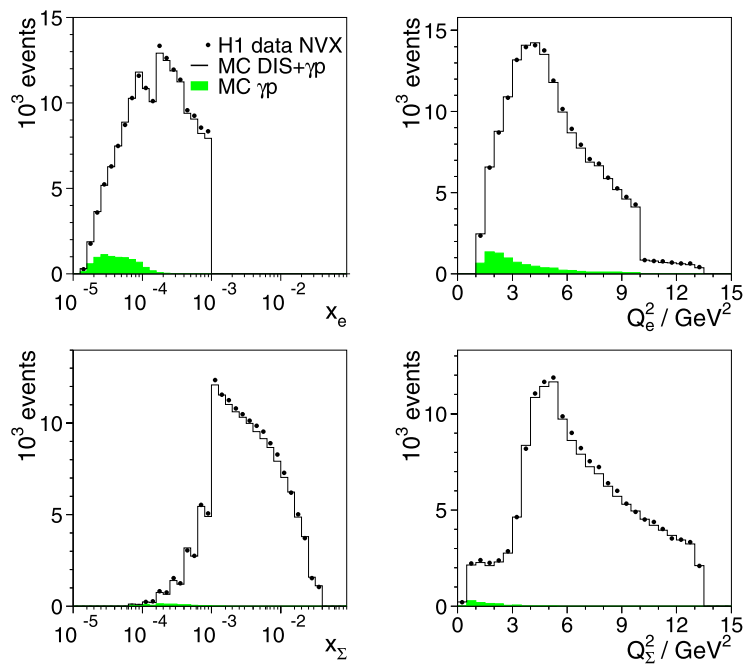


**Fig. 25** Distribution of Bjorken- $x$  and  $Q^2$  using the electron (*top*) and sigma (*bottom*) reconstruction methods for the SVX data. The histograms represent the simulation of DIS and the photoproduction background (*shaded*)

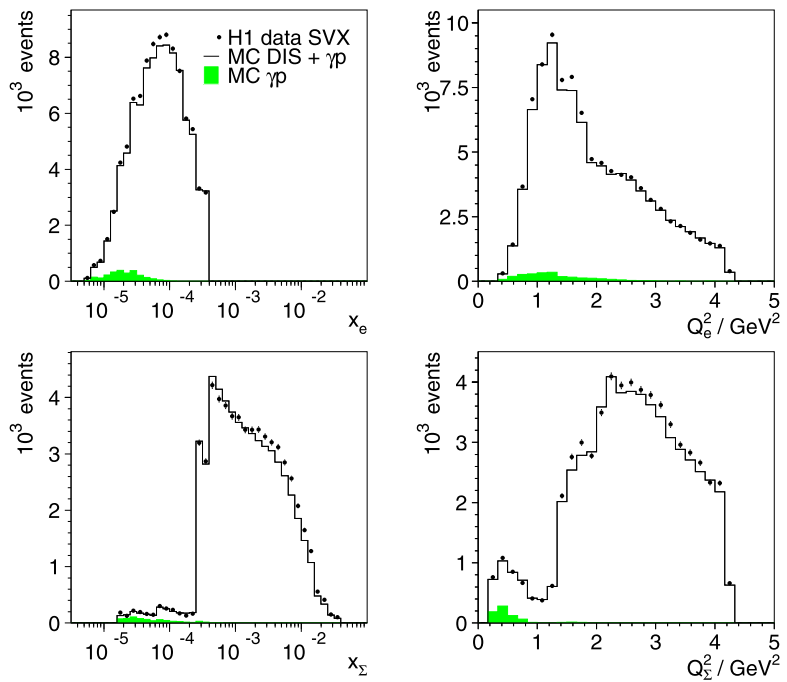
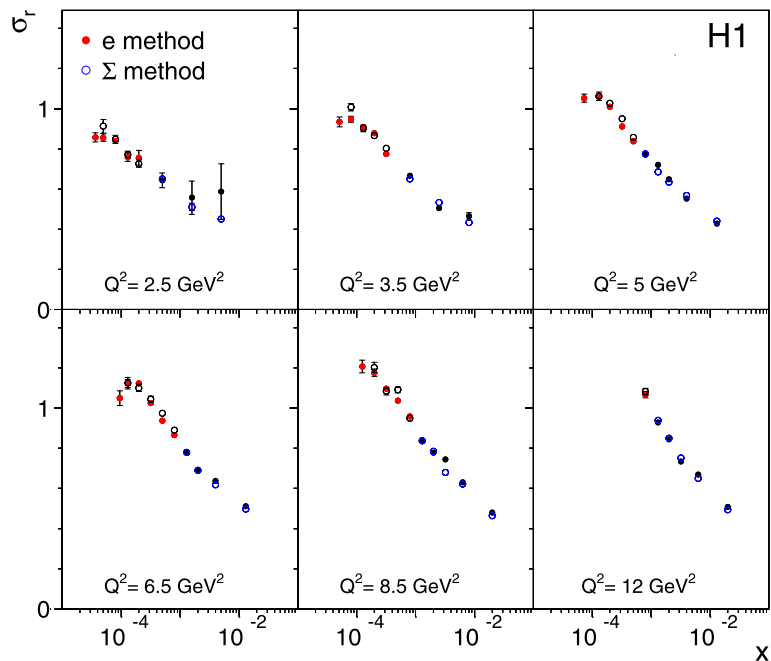


**Fig. 26** Comparison of reduced cross sections as obtained with the electron (*closed circles*) and  $\Sigma$  (*open circles*) reconstruction methods, for the NVX data sample. The errors represent statistical uncertainties only



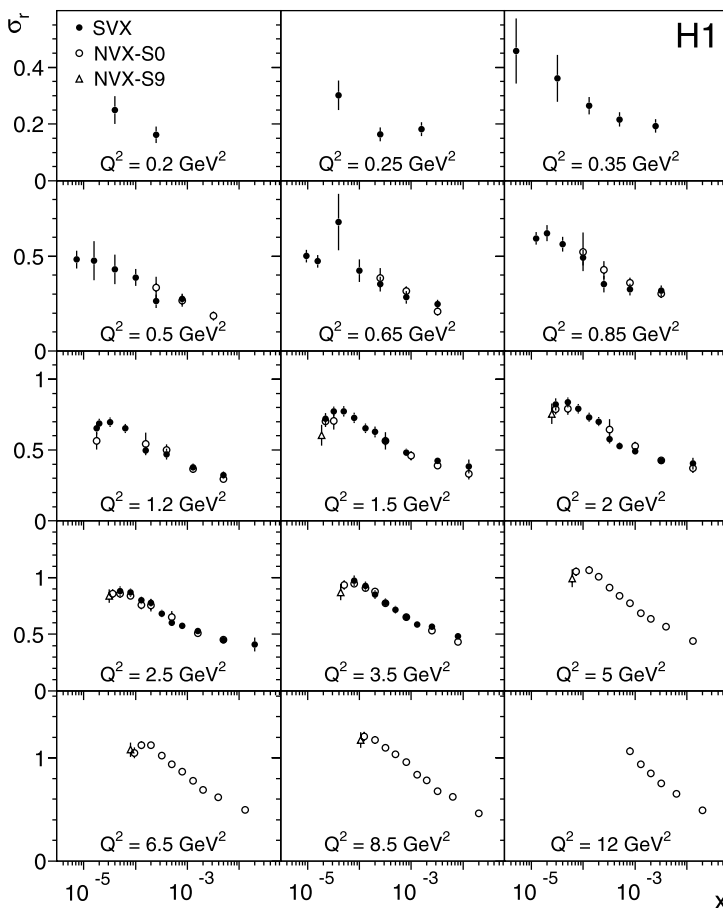
measurement are high for both methods. Figure 26 shows an example of this comparison, performed for the NVX-BST data set.

The third class of cross checks compares the cross section measurements performed with different data samples: SVX is compared to NVX and the new data are compared to the previously published results. This comparison is an integral part of the cross section averaging procedure, as discussed subsequently.

### 8.8 Cross sections

The cross section data measured from the SVX and NVX data samples are given in Tables 10–14 and presented in Fig. 27. The uncertainty of the new data is typically 3–4% and larger at the acceptance edges. Lowest values of  $Q^2$ , down to  $0.2 \text{ GeV}^2$ , are reached with the shifted vertex data. The analysis of the SVX data is mainly based on the BST but complemented by an independent analysis using the BDC an

**Fig. 27** Reduced inclusive  $e^+p$  scattering cross section as measured in the NVX-BST (open circles), NVX-S9 (triangles) and SVX (closed circles) analyses of the 920 GeV data. The errors represent the statistical and systematic uncertainties added in quadrature



lower radii. For  $Q^2$  between 0.5 and 3.5 GeV<sup>2</sup>, the NVX and SVX cross section data overlap in their kinematic coverage and are observed to be in agreement. The kinematic region of larger  $Q^2 \geq 5$  GeV<sup>2</sup> is covered by the nominal vertex data. The data at highest  $y$ , corresponding to smallest  $x$ , are obtained using the dedicated trigger S9 and can be seen in Fig. 27 to be consistent with the behaviour of  $\sigma_r$  towards small  $x$ .

**9 Combination of H1 cross section measurements**

The new data cover a kinematic region which overlaps with data sets taken at 820 GeV proton beam energy in 1995 [35] and in 1997 (sample B) [37]. The combination of all these data, as described subsequently, provides a single data set in the range  $0.2 \leq Q^2 \leq 12$  GeV<sup>2</sup> and  $5 \cdot 10^{-6} \leq x \leq 0.02$ .

**9.1 Procedure**

The combination of the data sets is based on the prescription introduced in [87] which is applicable if the uncertainties of the measurements do not depend on the central values. This procedure is described in Sect. 9.1.1. For the cross section measurements the estimated statistical and systematic

uncertainties depend on the central values. This leads to a modification of the averaging procedure as is described in Sect. 9.1.2.

*9.1.1 Linear averaging*

The averaging procedure is based on a  $\chi^2$  minimisation. For a single data set, the  $\chi^2$  function can be defined as

$$\chi_{\text{exp}}^2(\mathbf{m}, \mathbf{a}) = \sum_i \frac{[m^i - \sum_j \frac{\partial \mu^i}{\partial \alpha_j} (a_j - \alpha_j) - \mu^i]^2}{\Delta_i^2} + \sum_j \frac{(a_j - \alpha_j)^2}{\Delta_{\alpha_j}^2} \tag{26}$$

Here  $\mu^i$  is the measured central value at a point  $i$  with combined statistical and uncorrelated systematic uncertainty  $\Delta_i = (\Delta_{i,\text{stat}}^2 + \Delta_{i,\text{uncor}}^2)^{1/2}$ . Further,  $\alpha_j$  denotes the central value determined for a correlated systematic error source of type  $j$  with an uncertainty  $\Delta_{\alpha_j}$ , while  $\partial \mu^i / \partial \alpha_j$  quantifies the sensitivity of the measurement  $\mu^i$  at the point  $i$  to the systematic source  $j$ . The function  $\chi_{\text{exp}}^2$  depends on the set of underlying physical quantities  $m^i$  (denoted as the vector  $\mathbf{m}$ ) and the set of systematic uncertainties  $a_j$  ( $\mathbf{a}$ ). For the

reduced cross section measurements one has  $\mu^i = \sigma_r^i$ ,  $i$  denotes a  $(x, Q^2)$  interval, and the summation over  $j$  extends over all correlated systematic sources.

Introducing the variables  $b_j = (a_j - \alpha_j)/\Delta\alpha_j$  and  $\Gamma_j^i = (\partial\mu^i/\partial\alpha_j)\Delta\alpha_j$ , (26) can be written as

$$\chi_{\text{exp}}^2(\mathbf{m}, \mathbf{b}) = \sum_i \frac{[m^i - \sum_j \Gamma_j^i b_j - \mu^i]^2}{\Delta_i^2} + \sum_j b_j^2. \quad (27)$$

If several analyses provide a number of measurements at the same  $(x, Q^2)$  values, they can be combined using the formula above, generalised for the case of multiple data sets. Then a total  $\chi^2$  function,  $\chi_{\text{tot}}^2$ , is built from the sum of the  $\chi_{\text{exp}}^2$  functions for each data set according to

$$\chi_{\text{tot}}^2(\mathbf{m}, \mathbf{b}) = \sum_e \sum_{i=1}^{N_M} \frac{[m^i - \sum_{j=1}^{N_S} \Gamma_{j,e}^i b_j - \mu_e^i]^2}{\Delta_{i,e}^2} w_{i,e} + \sum_{j=1}^{N_S} b_j^2, \quad (28)$$

where the summation over  $i$  ( $j$ ) runs over all  $N_M$  measured points (all  $N_S$  systematic error sources) of all data sets considered. The symbol  $w_{i,e}$  is equal to one if data set  $e$  contributes a measurement at the point  $i$ , otherwise it is zero. Similarly, the symbol  $\Gamma_{j,e}^i$  equals to zero if the measurement  $i$  from the data set  $e$  is insensitive to the systematic source  $j$ . This definition of  $\chi_{\text{tot}}^2$  assumes that the data sets  $e$  are statistically uncorrelated. The systematic error sources  $b_j$ , however, may be either uncorrelated (separate sources) or correlated across data sets (different data sets sharing a common source).

Since  $\chi_{\text{tot}}^2$  is a quadratic form of  $\mathbf{m}$  and  $\mathbf{b}$ , it may be rearranged such that it takes a form similar to (26)

$$\begin{aligned} \chi_{\text{tot}}^2(\mathbf{m}, \mathbf{a}) &\equiv \chi_{\text{min}}^2 + \sum_{i=1}^{N_M} \frac{[m^i - \sum_j \frac{\partial\mu^{i,\text{ave}}}{\partial\alpha_j}(a_j - \alpha_{j,\text{ave}}) - \mu^{i,\text{ave}}]^2}{\Delta_{i,\text{ave}}^2} \\ &+ \sum_{j=1}^{N_S} \sum_{k=1}^{N_S} (a_j - \alpha_{j,\text{ave}})(a_k - \alpha_{k,\text{ave}})(A'_S)_{jk}. \end{aligned} \quad (29)$$

The data averaging procedure, described in detail in Appendix, determines the average values  $\mu^{i,\text{ave}}$ , the uncorrelated uncertainties  $\Delta_{i,\text{ave}}$ , the average systematic error source values  $\alpha_{j,\text{ave}}$ , the dependencies of  $\mu^{i,\text{ave}}$  on  $\alpha_j$ ,  $\partial\mu^{i,\text{ave}}/\partial\alpha_j$ , and the matrix  $(A'_S)_{jk}$ . The value of  $\chi_{\text{min}}^2$  corresponds to the minimum of (28). The ratio  $\chi_{\text{min}}^2/n_{\text{dof}}$  is a measure of the consistency of the data sets. The number of degrees of freedom,  $n_{\text{dof}}$ , is calculated as the difference

between the total number of measurements and the number of the measured points  $N_M$ . This procedure represents a method to average data sets, which allows correlations among the measurements due to systematic uncertainties to be taken into account.

The matrix  $(A'_S)_{jk}$  can be diagonalised and the  $\chi^2$  function takes a form similar to (27)

$$\chi_{\text{tot}}^2(\mathbf{m}, \mathbf{b}') = \chi_{\text{min}}^2 + \sum_{i=1}^{N_M} \frac{[m^i - \sum_{j=1}^{N_S} \Gamma_j^{i,\text{ave}} b'_j - \mu^{i,\text{ave}}]^2}{\Delta_{i,\text{ave}}^2} + \sum_{j=1}^{N_S} (b'_j)^2, \quad (30)$$

where  $b'_j = \sum_k U_{jk}(b_k - \beta_{k,\text{ave}})D_{jj}$  and  $\beta_{k,\text{ave}} = \alpha_{k,\text{ave}}/\Delta\alpha_k$ . The orthogonal matrix  $U$  connecting the systematic sources before and after averaging and the diagonal matrix  $D$  are given in Appendix.

### 9.1.2 Implementation for the cross section averaging

The  $\chi^2$  function of (26) is suitable for measurements in which the uncertainties are absolute, i.e. do not depend on the central value of the measurement. However, for the H1 cross section data considered here, the correlated and uncorrelated systematic errors are to a good approximation proportional to the central values (multiplicative errors), whereas the statistical errors scale with the square roots of the expected number of events. In this case the combination of the data sets using (26) leads to a small bias to lower cross section values since the measurements with lower central values have smaller absolute uncertainties. To take this effect into account, the  $\chi^2$  definition is modified to

$$\begin{aligned} \chi_{\text{exp}}^2(\mathbf{m}, \mathbf{b}) &= \sum_i \frac{[m^i - \sum_j \gamma_j^i m^i b_j - \mu^i]^2}{\delta_{i,\text{stat}}^2 \mu^i (m^i - \sum_j \gamma_j^i m^i b_j) + (\delta_{i,\text{uncor}} m^i)^2} \\ &+ \sum_j b_j^2. \end{aligned} \quad (31)$$

Here  $\gamma_j^i = \Gamma_j^i/\mu^i$ ,  $\delta_{i,\text{stat}} = \Delta_{i,\text{stat}}/\mu^i$  and  $\delta_{i,\text{uncor}} = \Delta_{i,\text{uncor}}/\mu^i$  are relative correlated systematic, statistical and uncorrelated systematic uncertainty, respectively. This  $\chi^2$  definition is used for the averaging procedure and also for the phenomenological analysis of the data (see Sect. 10). Equation (31) is equivalent to the one used in previous H1 analyses [37] up to modifications in the denominator. In contrast to (27), the  $\chi^2$  function of (31) is not a simple quadratic form with respect to  $m^i$  and  $b_j$ . The average is found in an iterative procedure: first equation (27) is used to get an initial approximation for  $\mu^{i,\text{ave}}$  and  $\beta_{j,\text{ave}}$  which are

used to recalculate the errors as  $\Gamma_j^i = \gamma_j^i \mu^{i,ave}$  and  $\Delta_i^2 = \delta_{i,stat}^2 \mu^i (\mu^{i,ave} - \sum_j \gamma_j^i \mu^{i,ave} \beta_{j,ave}) + (\delta_{i,uncor} \mu^{i,ave})^2$ . Then the determination of  $\mu^{i,ave}$  is repeated. Convergence is observed after two iterations.

For measurements with multiplicative errors the geometric mean instead of the arithmetic mean can be used as an alternative, i.e. the average is performed for  $\ln \sigma_r^i$ . In this case the quadratic equation (27) can be used by replacing  $\mu^i \rightarrow \ln \sigma_r^i$ ,  $\Delta_i \rightarrow (\delta_{i,stat}^2 + \delta_{i,uncor}^2)^{1/2}$  and  $\Gamma_j^i \rightarrow \gamma_j^i$ . This logarithmic averaging procedure is used as a cross check.

For the NVX and SVX analyses, the measured cross section values  $\sigma_r^i$ , the statistical and uncorrelated uncertainties  $\delta_{i,stat}$ ,  $\delta_{i,uncor}$  and all correlated systematic uncertainties  $\gamma_j^i$  as well as the total error  $\delta_{i,tot} = [\delta_{i,stat}^2 + \delta_{i,uncor}^2 + \sum_j (\gamma_j^i)^2]^{1/2}$  are given in Tables 10–14. The average of the H1 data is reported in Tables 15–20, where the average reduced cross sections  $\sigma_r^{i,ave} = \mu^{i,ave}$ , the statistical  $\delta_{i,ave,stat}$ , uncorrelated  $\delta_{i,ave,uncor}$ , correlated  $\gamma_j^{i,ave}$  and total  $\delta_{i,ave,tot} = [\delta_{i,ave,stat}^2 + \delta_{i,ave,uncor}^2 + \sum_j (\gamma_j^{i,ave})^2]^{1/2}$  uncertainties are given. The transformation matrix  $U$  is given in Table 21. The shifts of the central values of the systematic error sources, in units of the systematic errors  $\alpha_{j,ave}/\Delta_{\alpha j}$ , are given in Table 5.

### 9.2 Compatibility of SVX and NVX data

The combination of the SVX and NVX data depends upon assumptions on the correlation between different data points, within a data set as well as across the data sets. For each data set, two types of systematic uncertainty are considered: fully correlated ones, which are treated as  $\alpha_j$  in (31), and fully uncorrelated ones, which are added to the statistical uncertainties in quadrature and treated as  $\delta_i$  in (31). Following the notation in Table 4, the six sources of correlated uncertainties are  $E'_e$  scale,  $\theta_e$ , LAr hadronic energy scale, LAr noise, SpaCal hadronic scale and photoproduction background. A further correlated uncertainty arises from the luminosity measurements. Concerning the relation between data sets, the systematic uncertainty of the

luminosity measurement is separated into a 0.5% fully correlated theoretical uncertainty and an uncorrelated experimental part due to variations of beam and detector acceptance conditions. The other systematic uncertainties are considered to be uncorrelated.

The systematic uncertainties which are correlated between data points can be assumed as either fully correlated, uncorrelated or partially correlated between the NVX and the SVX data. The reasons for correlations between data sets are the similarity in the calibration procedure and the detector setup. Uncorrelated effects arise from variations with time, differences between the kinematic ranges of the calibration samples, the dead material, the detector illumination or the acceptance. For each source the uncorrelated part is more important and thus all sources are considered to be uncorrelated between the NVX and the SVX data.

To check the sensitivity of the averaged result to the correlation assumptions, the average of the NVX and SVX data, obtained by considering the six systematic sources to be uncorrelated, is compared to  $2^6 - 1$  other possible assumptions in which each source is either fully correlated or fully uncorrelated. Most of the cases lead to numerically small variations for both the central values and the total errors of the average data. The only significant variation is observed for the lowest  $y$  points for  $Q^2 > 2 \text{ GeV}^2$ , if the LAr noise is assumed to be correlated between the NVX and SVX data. Since the LAr noise, however, is a time dependent uncorrelated source, no additional systematic uncertainty is assigned to the combined measurement.

The NVX and SVX data sets are fully consistent, according to the averaging procedure, with  $\chi^2_{\min}/n_{\text{dof}} = 19.5/39$ . The shifts of the central values of the systematic uncertainties do not exceed one standard deviation.

### 9.3 Global combination of low $Q^2$ H1 data

The new data given in Tables 10–14 are combined with the previously published H1 data obtained for a similar kinematic region. The comparison of the present cross section data, obtained by averaging the SVX and the NVX data,

**Table 5** Shifts of the central values of the systematic uncertainties  $\alpha_{j,ave}/\delta_{\alpha j}$  based on the average of the published  $E_p = 820 \text{ GeV}$  and the new NVX-SVX data. For example, the quoted value for the luminosity shift of the SVX95 sample,  $-1.60$ , corresponds to a  $-1.60 \times 3\% = 4.80\%$  downward shift of the SVX95 cross section values

Systematic source	Shift in $\sigma$			
	SVX95	NVX97	NVX	SVX
$E'_e$ scale	0.03	1.19	-0.32	0.36
$\theta_e$	0.20	-0.72	1.03	0.48
LAr scale	-0.09	0.06	-0.23	-1.79
LAr noise	-	-1.06	-0.20	-1.13
SpaCal hadronic scale	-	-	0.48	-1.66
$\gamma p$ background	0.48	-0.10	0.05	0.10
Luminosity	-1.60	0.66	0.10	0.17

with the published cross section data, is given in Fig. 28. The new data are in agreement with the published NVX97 data [37] taking the +3.4% normalisation shift of the published data (Sect. 8.4) into account. The data are also consistent with the SVX95 data [35] within their rather large uncertainties. For the combination of all data, the systematic uncertainties are considered to be uncorrelated across the data sets.

The published H1 data [35, 37] were taken with a proton beam energy of  $E_p = 820$  GeV. Therefore a centre-of-mass energy (CME) correction, based on (1), is applied when comparing to the previously published cross section according to

$$\sigma_r^{920}(x, Q^2) = \sigma_r^{820}(x, Q^2) + F_L^{\text{th}}(x, Q^2)[f(y_{820}) - f(y_{920})]. \quad (32)$$

Here  $\sigma_r^{920}(x, Q^2)$  is the reduced cross section rescaled to  $E_p = 920$  GeV;  $\sigma_r^{820}(x, Q^2)$  is the measured reduced cross section for  $E_p = 820$  GeV;  $y_{820}$  and  $y_{920}$  are the inelasticities for the two proton beam energies calculated as  $y = Q^2/4E_e E_p x$ , and  $F_L^{\text{th}}(x, Q^2)$  is calculated using the fractal model for  $F_2(x, Q^2)$  and  $R = 0.5$ . This correction becomes large only at high  $y$ . To avoid any sizeable effect of the en-

ergy dependence of  $\sigma_r$  on the combination of the 820 and 920 GeV data, the combination of the points at the same  $(x, Q^2)$  is restricted to a region of  $y_{820} < 0.35$ . At higher  $y$  the measurements are kept separately but they are affected by the combination procedure. The residual dependence on the  $F_L$  assumption for the average points is negligible. For illustrative purposes, the CME correction is applied to all 820 GeV data points in Figs. 28–32.

The H1 data sets are consistent with each other. If all samples are averaged in a single step one obtains  $\chi^2_{\text{tot}}/n_{\text{dof}} = 86.2/125$ . Shifts of the central values of the systematic sources  $\alpha_j/\Delta\alpha_j$  are given in Table 5. The systematic shifts imposed by the averaging procedure are mostly within one standard deviation. The most noticeable effects are a downward shift of the normalisation of the SVX95 data and a modification of the LAr hadronic energy scale of the SVX data which corresponds to a small adjustment of the SVX data at large  $x$ .

The combination of the H1 data using the  $\chi^2$  definition of (31) has been compared to that using the  $\chi^2$  definition of (27) and also using the logarithmic averaging procedure. For the bulk of the phase space, the definition of (27) would lead to a change of typically  $-0.7\%$ , which increases to  $-2.0\%$  for the data at  $Q^2 \leq 0.5$  GeV<sup>2</sup>. For the logarithmic

**Fig. 28** Reduced cross section  $\sigma_r$ . Closed circles: combined 1999–2000 data taken at  $E_p = 920$  GeV; Triangles: SVX data taken in 1995 [35]; Open circles: NVX data taken in 1997 [37]. The normalisation of the 1997 data has changed by +3.4%, see Sect. 8.4. The 1995 and 1997 data were taken at  $E_p = 820$  GeV but are corrected here for comparison to 920 GeV. The errors represent the statistical and systematic uncertainties added in quadrature

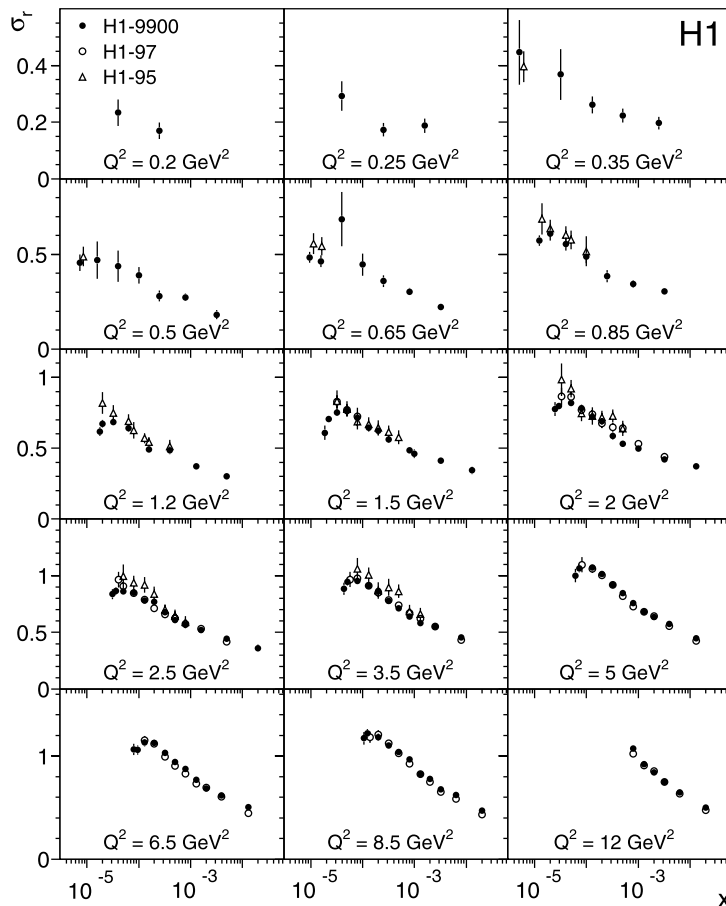
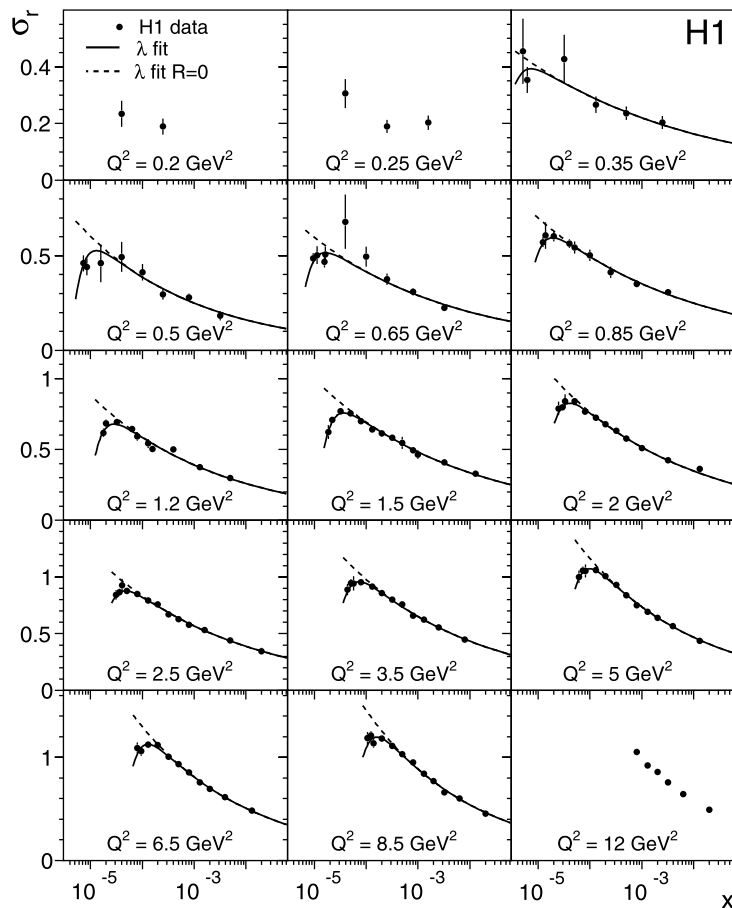


**Fig. 29** Reduced cross section  $\sigma_r$ , from the combined low  $Q^2$  H1 data, as a function of  $x$  compared to the  $\lambda$  fit result (solid line) and to a  $\lambda$  parameterisation with the same values of  $c(Q^2)$  and  $\lambda(Q^2)$  but  $R = 0$  (dashed line). The errors represent the statistical and systematic uncertainties added in quadrature



mic average the difference compared to (31) is typically below 0.1%.

#### 9.4 Combined cross section results

The combined low  $Q^2$  data and the resulting uncertainties are listed in Tables 15–20 and shown in Figs. 28–32. There are 149 data points. The total uncertainty in the central  $Q^2$ ,  $x$  region of this measurement is about 2% but it becomes larger towards the edges of the covered phase space. At high  $y$ , for example, the measurement at a  $Q^2$  value of a few  $\text{GeV}^2$  has an uncertainty of about 5%.

Figures 29 and 30 show the combined H1 reduced  $ep$  cross section measurement and different phenomenological descriptions as introduced below. For all  $Q^2$  bins, starting at large  $x$  the reduced cross section first increases for  $x \rightarrow 0$ . For  $Q^2 \geq 0.6 \text{ GeV}^2$  there is a characteristic turn over of the cross section observed at the smallest  $x$  values. This region, for each  $Q^2$ , corresponds to highest inelasticity,  $y = Q^2/(sx)$ , and thus the turn over at  $y \approx 0.6$  can be attributed to the influence of the longitudinal structure function  $F_L$ .

For  $y < 0.6$  the influence of the longitudinal structure function is small and thus one can extract the structure function  $F_2$  with only a small residual dependence on the assumption on  $F_L$ . Using  $R = 0.5$ ,  $F_2$  is extracted and shown in Fig. 31. The structure function  $F_2$  exhibits a steady increase as  $x \rightarrow 0$  for all  $Q^2$  bins.

Figure 32 shows the measurement of the virtual photon-proton effective cross section  $\sigma_{\gamma^*p}^{\text{eff}}$  as a function of  $Q^2$  at various values of  $W$ . The H1 data are compared to the data of ZEUS [38, 39] and to different models, as discussed below. A good agreement between the data sets is observed. The H1 data extend the HERA measurements to higher and lower  $W$  and also cover the  $Q^2 \sim 1 \text{ GeV}^2$  region.

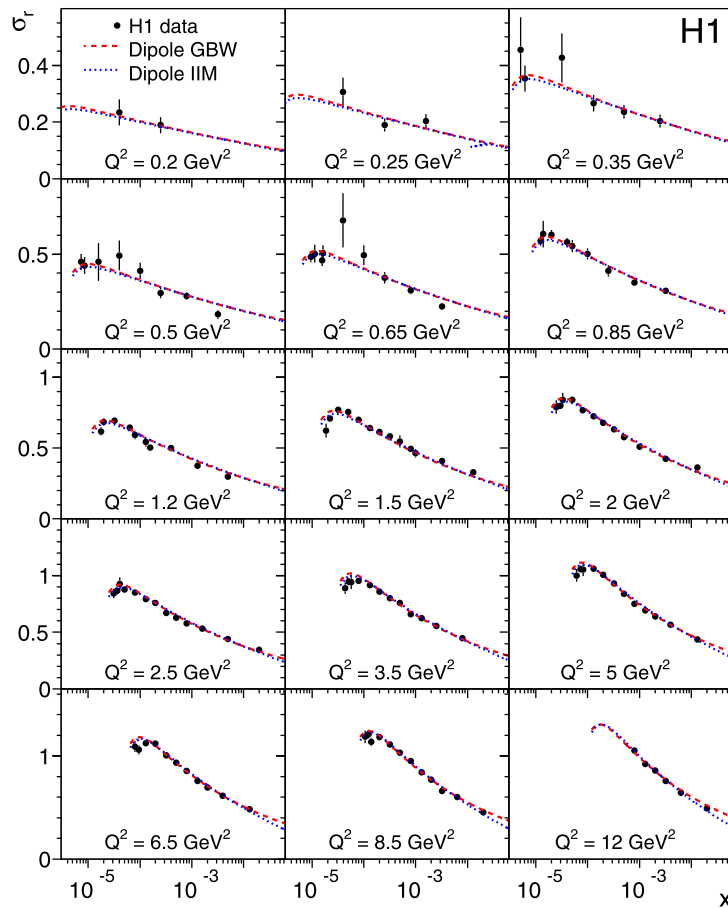
## 10 Cross section analysis

### 10.1 Rise of $F_2$ at low $x$ and extraction of $R$

The rise of the structure function  $F_2$  towards low  $x$  has previously been described by a power law in  $x$ ,  $F_2 = c(Q^2)x^{-\lambda(Q^2)}$ , where the exponent  $\lambda$  increases approximately logarithmically with  $\ln Q^2$  for  $Q^2 \gtrsim 2 \text{ GeV}^2$  [88].



**Fig. 30** Reduced cross section  $\sigma_r$ , from the combined low  $Q^2$  H1 data, as a function of  $x$  compared to the GBW and IIM models. The errors represent the statistical and systematic uncertainties added in quadrature



This simple parametrisation has been shown to model the  $ep$  data well for  $x < 0.01$ .

This idea can be extended to fit the reduced cross section  $\sigma_r$  in order simultaneously to extract the exponent  $\lambda$  and to estimate the longitudinal structure function  $F_L$ . The measured  $ep$  cross section is sensitive to the longitudinal structure function  $F_L$  only for large  $y \gtrsim 0.5$ , a region which corresponds to a limited  $x$  range for a given  $Q^2$  value. Gluon dominance at low  $x$  suggests that the function  $F_L$  may exhibit an  $x$  dependence similar to  $F_2$ . In the subsequent studies using this ansatz it is assumed that  $F_L$  is proportional to  $F_2$  and that the coefficient of proportionality depends only on  $Q^2$ . For the extraction of  $F_L$ , the ratio of  $\sigma_L/\sigma_T = R$  is used such that

$$F_L(Q^2, x) = F_2(Q^2, x) \frac{R(Q^2)}{1 + R(Q^2)} \tag{33}$$

and

$$\sigma_r(Q^2, x) = c(Q^2) x^{-\lambda(Q^2)} \left[ 1 - f(y) \frac{R(Q^2)}{1 + R(Q^2)} \right]. \tag{34}$$

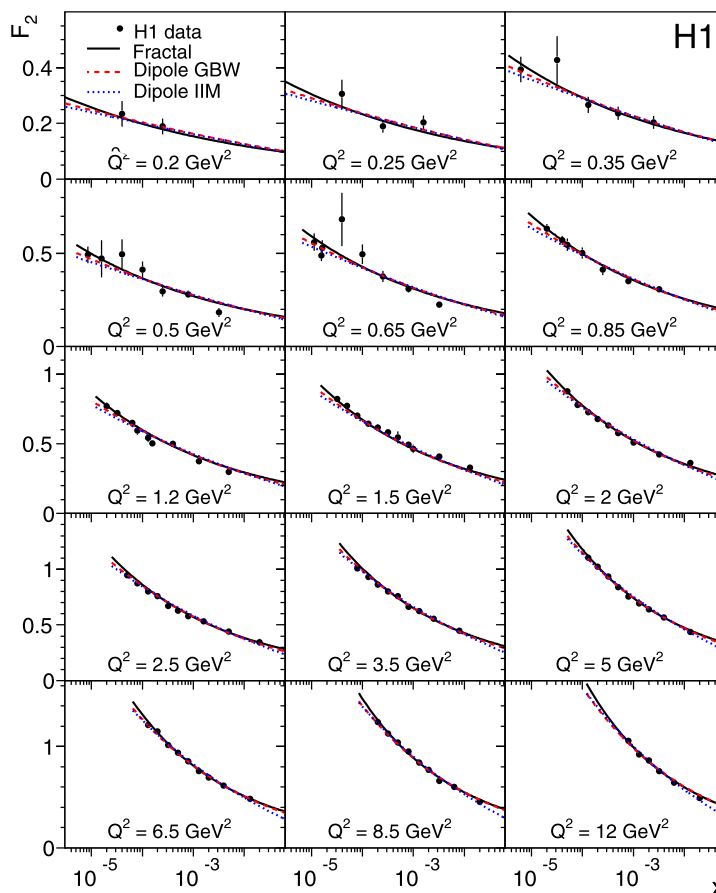
The combined 1995–2000 H1 low  $Q^2$  data are fitted following (34) for each  $Q^2$  bin. These fits describe the data

very well, as is illustrated in Fig. 29. The results of these fits are shown in Figs. 33 and 34. The fit results for  $\lambda(Q^2)$  are given in Table 6. One can see in Fig. 33(b) that the parameter  $\lambda$  shows an approximately linear increase as a function of  $\ln Q^2$  for  $Q^2 > 2 \text{ GeV}^2$  as has been observed previously [88]. For lower  $Q^2$  the variation of  $\lambda$  is diminished but relatively large uncertainties prevent definite conclusions. The normalisation coefficient  $c(Q^2)$  rises with increasing  $Q^2$  for  $Q^2 < 2 \text{ GeV}^2$  and is consistent with a constant behaviour in the DIS region, as in [88].

The values of the coefficient  $R(Q^2)$  are consistent with no dependence on  $Q^2$ . The mean  $R$  is  $0.55 \pm 0.05$  with  $\chi^2/n_{\text{dof}} = 7.9/(8 - 1)$ . While the experimental error is small there is a very strong model dependence, different parameterisations for  $F_2$  leading to significant changes in  $F_L$ , see Sect. 11. The value of the average  $R$  obtained in this model is consistent within about one standard deviation with  $R = 0.5$  or  $\sigma_L = \frac{1}{2}\sigma_T$ . This value of  $R$  leads to an  $F_L$  which is higher than the first direct measurement of  $F_L$  at low  $x$  performed by the H1 collaboration [89]. The data in [89] correspond however to higher  $Q^2$  values ( $\geq 12 \text{ GeV}^2$ ).

<sup>9</sup>For the determination of the mean,  $R$  values from different  $Q^2$  bins are assumed to be uncorrelated and total errors are used.

**Fig. 31** Structure function  $F_2$ , from the combined low  $Q^2$  H1 data for  $y < 0.6$ , as a function of  $x$  compared to the fractal, the dipole GBW and the dipole IIM fit results. The errors represent the statistical and systematic uncertainties added in quadrature



10.2 Determination of  $F_L$  using the  $y$  dependence of the cross section

The turn-over of the measured DIS cross section for the highest  $y$  values, apparent in Fig. 29, can be used for an extraction of the longitudinal structure function  $F_L$  using the so-called derivative method [37]. The derivative of the reduced cross section with respect to  $\ln y$  is

$$\left. \frac{d\sigma_r}{d \ln y} \right|_{Q^2=\text{const}} = -\frac{dF_2}{d \ln x} - \frac{2y^2(2-y)}{(1+(1-y)^2)^2} F_L - \frac{y^2}{1+(1-y)^2} \frac{dF_L}{d \ln x}. \tag{35}$$

At high  $y$  for a wide variety of models the term proportional to  $F_L$  becomes numerically larger than other contributions. Therefore the extraction of the derivative provides means for determining  $F_L$  at low  $x$  and  $Q^2$  with little phenomenological assumptions.

Experimentally,  $d\sigma_r/d \ln y$  is approximated by  $y_{\text{av}} \Delta\sigma_r/\Delta y$ , which is calculated for each pair of cross section measurements in neighbouring bins. Here  $\Delta y$  is determined using bin centre values, and  $y_{\text{av}}$  is the logarithmic

average value. Only the  $E_p = 920$  GeV data are used in this determination. The H1 data are illustrated in Fig. 35 and are compared to the fractal and dipole models discussed below in Sects. 11.1 and 11.2. Similar analysis using the  $E_p = 820$  GeV data was presented in [37]. The systematic uncertainties are evaluated by changing the cross sections for each source of systematic uncertainty and repeating the calculation of the cross section difference. For the model predictions,  $\Delta\sigma_r/\Delta y$  is calculated in an analogous way and using the same binning as for the data.

For the extraction of the structure function  $F_L$ , the fractal fit, introduced in Sect. 11.1, is used to estimate the  $dF_2/d \ln x$  contribution to  $\Delta\sigma_r/\Delta y$ , and also for the bin centre correction. To reduce the dependence on  $F_2$ , only  $\Delta\sigma_r/\Delta y$  value corresponding to  $y = 0.735$  are used to determine  $F_L$ .

The resulting longitudinal structure function values are shown in Fig. 36. The derivative method is only weakly dependent on the model assumptions. There are however large experimental uncertainties, mostly due to statistics and the photoproduction background at large  $y$ . The  $F_L$  data are consistent with a constant  $R = 0.5$ , as introduced above, and also with smaller values on  $R$ , as obtained in the dipole models. The dependence of the measurement on the assumption

**Fig. 32** Measurement of the virtual photon-proton cross section  $\sigma_{\gamma^*p}^{\text{eff}}$  as a function of  $Q^2$  at various values of  $W$ . The cross sections for different  $W$  values are multiplied by the factors indicated in the figure. The errors represent the statistical and systematic errors added in quadrature. The averaged H1 results are compared to data obtained by the ZEUS experiment and to the fractal and dipole model fit results

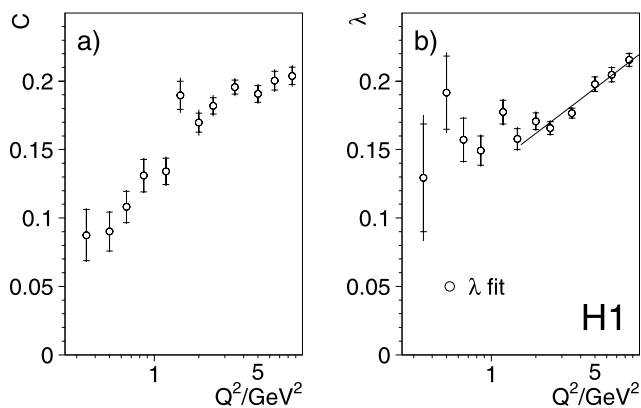
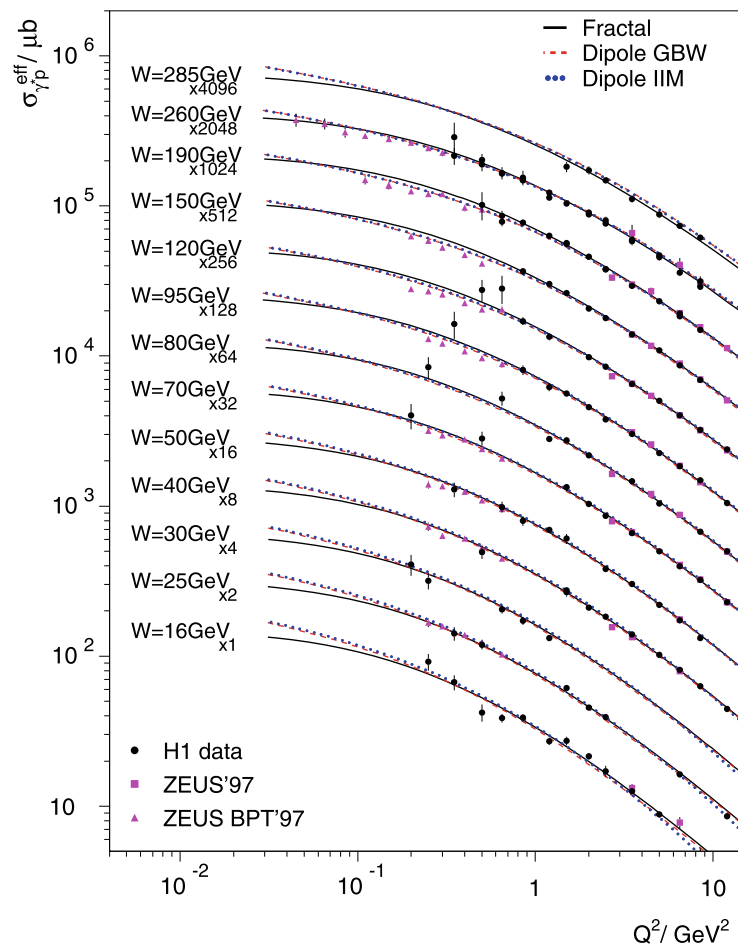


**Fig. 33** Coefficients  $c$  and  $\lambda$ , as defined in (34), determined from a fit to the H1 data as a function of  $Q^2$ . The inner error bars represent uncorrelated systematic uncertainties. The outer error bars represent total uncertainties. The line in (b) shows a straight line fit for  $Q^2 \geq 2 \text{ GeV}^2$

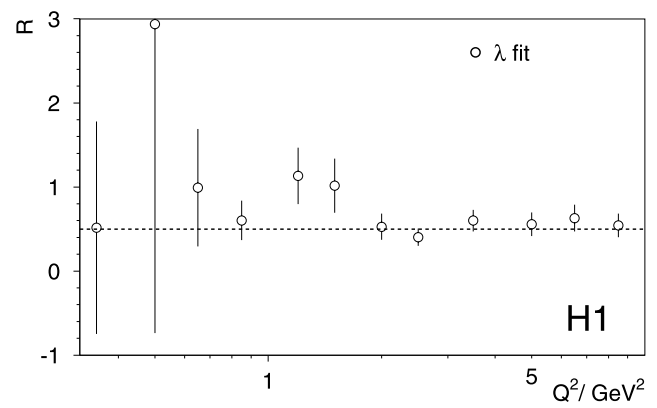


**Fig. 34** Coefficient  $R$  as a function of  $Q^2$  from a simple parameterisation of the reduced cross section as defined in (34). The dashed line is drawn at  $R = 0.5$ . The errors represent the total uncertainties

made for  $F_2$  is estimated by a comparison with results obtained when assuming  $F_2$  to be independent of  $x$ . The difference between the extracted  $F_L$  values is shown as the band at the bottom of Fig. 36.

### 11 Model comparisons

In the following the combined data are analysed in the context of the fractal model [33] and two versions of the colour dipole model [42, 45], which unlike pQCD may be applied

**Table 6** Results of the fit (see (34)) to the combined H1 low  $Q^2$  data on the exponent  $\lambda$  with the statistical  $\delta\lambda_{\text{stat}}$ , uncorrelated systematic  $\delta\lambda_{\text{uncor}}$ , correlated systematic  $\delta\lambda_{\text{cor}}$ , and total uncertainties  $\delta\lambda_{\text{tot}}$

$Q^2/\text{GeV}^2$	$\lambda$	$\delta\lambda_{\text{stat}}$	$\delta\lambda_{\text{uncor}}$	$\delta\lambda_{\text{cor}}$	$\delta\lambda_{\text{tot}}$
0.35	0.129	0.029	0.026	0.024	0.046
0.50	0.192	0.022	0.016	0.012	0.030
0.65	0.157	0.010	0.011	0.006	0.016
0.85	0.149	0.009	0.009	0.005	0.014
1.20	0.177	0.007	0.007	0.005	0.011
1.50	0.158	0.004	0.006	0.004	0.008
2.00	0.171	0.003	0.005	0.004	0.007
2.50	0.166	0.002	0.005	0.003	0.006
3.50	0.177	0.002	0.003	0.002	0.004
5.00	0.198	0.003	0.004	0.002	0.005
6.50	0.205	0.003	0.005	0.003	0.007
8.50	0.216	0.003	0.005	0.003	0.007

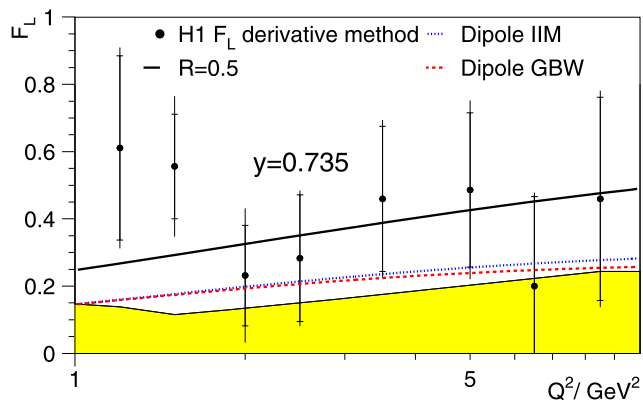


**Fig. 36** Structure function  $F_L$  extracted using the derivative method. The solid line is drawn for  $R = 0.5$  assuming the fractal parameterisation for  $F_2$ . The dashed (dotted) line corresponds to the dipole GBW (IIM) model. The inner error bars represent statistical and uncorrelated uncertainties added in quadrature, the outer error bars represent the total uncertainties. The solid (yellow) band indicates the model uncertainty, see text

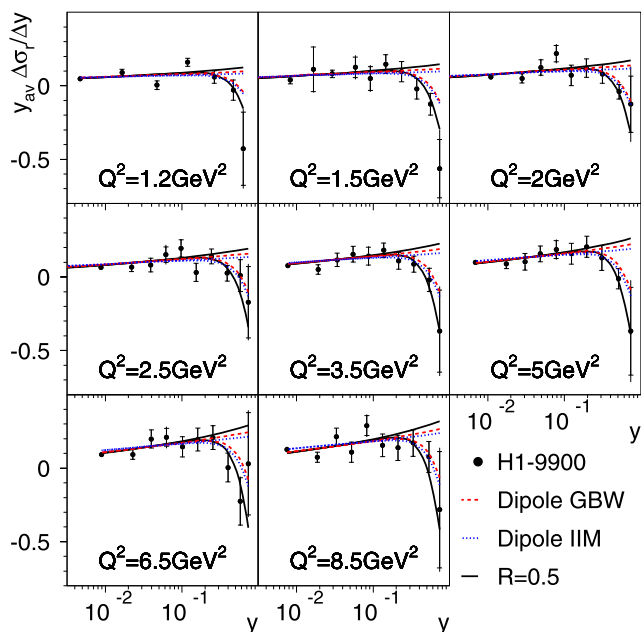


**Fig. 35** Derivative  $y_{\text{av}} \Delta\sigma/\Delta y$  for the combined 1999–2000 H1 data compared to the predictions of the dipole models and the fractal model for  $F_2$  with an assumption  $R = 0.5$  to describe  $F_L$ , labeled  $R = 0.5$ . The lines increasing as a function of  $\ln y$  correspond to  $F_L = 0$  for these models. The lines turning over at high  $y$  correspond to the cross section predictions. The inner error bars represent statistical and uncorrelated uncertainties added in quadrature, the outer error bars represent the total uncertainties

to describe the transition region from photoproduction to deep inelastic scattering. Fits are performed using (31).

### 11.1 Fractal fit

In the fractal ansatz [33], the proton structure function  $F_2$  is parameterised using five parameters  $Q_0$  and  $D_0$  to  $D_3$  as

$$F_2(Q^2, x) = D_0 Q_0^2 \left(1 + \frac{Q_0^2}{Q^2}\right)^{1-D_2} \frac{x^{-D_2+1}}{1 + D_3 - D_1 \ln x} \times \left(x^{-D_1 \ln[1 + \frac{Q_0^2}{Q^2}]} \left(1 + \frac{Q^2}{Q_0^2}\right)^{D_3+1} - 1\right). \quad (36)$$

The parameters of this model are determined with a fit to the cross section data, except for the parameter  $D_2$ , which governs the structure function behaviour for the photoproduction regime and is fixed to  $D_2 = 1.08$ . This parameterisation is used in the Monte Carlo reweighting procedure. The fractal model [33] does not provide predictions for  $F_L$ . The same prescription is followed as for the  $\lambda$  parameterisation fit described in Sect. 10.1 taking the  $F_L$  contribution to be proportional to  $F_2$ .

The values of  $R$  are found to be consistent with the  $\lambda$  fit and with being independent of  $Q^2$ . Thus for the fractal parameterisation of the reduced cross section,  $R$  is taken to be a constant, which results in the simple five parameter representation used in the present analysis. The parameters of the fit are given in Table 7. The fit describes the data well with  $\chi^2/n_{\text{dof}} = 155.3/(149 - 5)$ . Similarly to the  $\lambda$  fit, the value of  $R = 0.56 \pm 0.07$  is consistent within about one standard deviation with  $R = 0.5$ . This agreement with the  $\lambda$  fit may be attributed to the structure function  $F_2$  having a power law-like  $x$  dependence.

**Table 7** Parameters of the fractal fit and their total uncertainties. For the central fit  $D_2$  is kept constant:  $D_2 = 1.08$ . If the parameter  $D_2$  is floated, the fit gives  $D_2 = 1.061 \pm 0.012$

Parameter	Value	Uncertainty
$D_0$ (GeV <sup>-2</sup> )	0.75	0.03
$D_1$	0.052	0.002
$D_3$	-1.16	0.03
$Q_0^2$ (GeV <sup>2</sup> )	0.093	0.010
$R$	0.56	0.07

### 11.2 Dipole model fits

In the GBW model [42] the dipole-proton cross section  $\hat{\sigma}$  (see Sect. 3) is given by

$$\hat{\sigma}(x, r) = \sigma_0 \{1 - \exp[-r^2/(4r_0^2(x))]\}, \tag{37}$$

where  $r$  corresponds to the transverse separation between the quark and the antiquark, and  $r_0^2$  is an  $x$  dependent scale parameter, assumed to have the form

$$r_0^2(x) \sim (x/x_0)^\lambda. \tag{38}$$

For small  $r \ll r_0$ ,  $\hat{\sigma}$  is proportional to  $r^2$  (colour transparency,  $\hat{\sigma} \sim (r/2r_0)^2$ ) while for  $r \gg r_0$  the cross section approaches a constant value (saturation,  $\hat{\sigma} \simeq \sigma_0$ ). The boundary in the  $(x, Q^2)$  plane which separates these regions is described by the “critical line” at the  $x$  dependent saturation scale  $Q_s^2(x) = 1/r_0^2(x)$ . The model provides predictions for both  $\sigma_T$  and  $\sigma_L$  in terms of only three parameters,  $\sigma_0$ ,  $x_0$  and  $\lambda$ .

The fit to the reduced cross section with the dipole model of GBW (“GBW fit”) yields a  $\chi^2/n_{\text{dof}} = 183.1/(149 - 3)$ , acceptable but worse than that for the fractal model. It has been suggested that improved models of  $\hat{\sigma}$  lead to a better description of the data and a variety of models has been developed. As an example, a fit using  $\hat{\sigma}$  as proposed in the IIM model, with  $N_0 = 0.7$  as defined in [45], has been performed. This fit also has three free parameters and gives  $\chi^2/n_{\text{dof}} = 178.2/(149 - 3)$ . The results of the two dipole model fits are shown in Figs. 30–32 and 35–36. The dipole model fit parameters are given in Tables 8 and 9.

To trace the origin of the  $\chi^2$  differences between the models, predictions for the structure functions  $F_2$  and  $F_L$  are compared individually. As an example, Fig. 37 shows the comparison between the three models for the bin  $Q^2 = 1.2 \text{ GeV}^2$ . The structure functions  $F_2$  agree rather well for the models considered for  $x > x_s = 0.18 \times 10^{-4}$ , where  $x_s$  corresponds to the saturation radius of the GBW dipole model at the chosen  $Q^2$  value. However, for  $x < x_s$  the dipole models show a softer  $F_2$  dependence on  $x$ . This holds in particular for the IIM dipole model. The main difference between the models is in the structure function  $F_L$ . As shown

**Table 8** Parameters of the GBW dipole fit and their total uncertainties

Parameter	Value	Uncertainty
$\sigma_0$ (mb)	24.5	0.5
$\lambda$	0.256	0.003
$x_0$	$0.60 \times 10^{-4}$	$0.03 \times 10^{-4}$

**Table 9** Parameters of the IIM dipole fit with  $N_0 = 0.7$  and their total uncertainties

Parameter	Value	Uncertainty
$R_{\text{IIM}}$ (fm)	0.605	0.008
$\lambda$	0.260	0.003
$x_0$	$0.45 \times 10^{-4}$	$0.03 \times 10^{-4}$

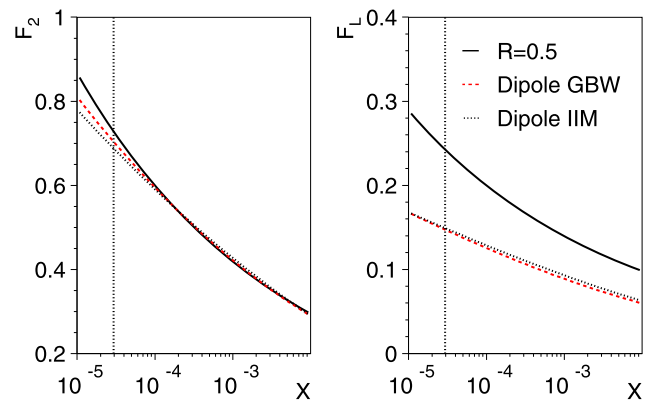


**Fig. 37** Comparison of the structure functions  $F_2$  (left) and  $F_L$  (right) for  $Q^2 = 1.2 \text{ GeV}^2$  as a function of Bjorken  $x$ , for the fractal fit with  $R = 0.5$  (solid line), and the predictions of the dipole models, GBW (dashed line) and IIM (dotted line), resulting from the fits to the H1 cross section data. The vertical line indicates the value of  $x = x_s$  for which the GBW dipole model saturation radius is reached

in Fig. 37, the predictions of the dipole models are nearly half of the result for  $F_L$  obtained with the fractal model analysis.

The strict correlation between  $F_L$  and  $F_2$  predicted by the dipole models could be broken by higher twist effects [90]. To quantify the influence of the structure function  $F_L$  another fit to the reduced cross section data is performed, in which the  $F_L$  prediction of the dipole model is scaled with an additional free parameter  $B_L$

$$F_L(x, Q^2) = F_L^{\text{dipole}}(x, Q^2)(1 + B_L). \tag{39}$$

With  $B_L$  as a formal free parameter the GBW fit returns  $B_L$  deviating from 0 by more than 3 standard deviations,  $B_L = 0.54 \pm 0.15$ . The fit for the IIM model does not yield a significant change for the  $F_L$  prediction:  $B_L = 0.15 \pm 0.14$ .

To summarise, a steeper rise to smaller  $x$  of the structure function  $F_2$ , together with a larger  $R$  value as obtained in

**Table 10** Reduced cross section  $\sigma_r$ , as measured with the SVX data sample for  $0.2 \leq Q^2 \leq 1.2 \text{ GeV}^2$ . The uncertainties are quoted in % relative to  $\sigma_r$ .  $\delta_{\text{tot}}$  is the total uncertainty determined as the quadratic sum of systematic and statistical uncertainties.  $\delta_{\text{stat}}$  is the statistical uncertainty.  $\delta_{\text{uncor}}$  represents the uncorrelated systematic uncertainty.  $\gamma_{E'_e}$ ,  $\gamma_{\theta_e}$ ,  $\gamma_{E_{\text{had}}}$ ,  $\gamma_{\text{noise}}$ ,  $\gamma_{E_{\text{SpaCal}}^h}$  and  $\gamma_{\gamma p}$  are the bin-to-bin correlated systematic uncertainties in the cross section measurement due to uncertainties in the SpaCal electromagnetic energy scale, electron scattering angle, LAr calorimeter hadronic energy scale, LAr calorimeter noise, SpaCal hadronic energy scale and the photoproduction background, respectively. The luminosity uncertainty of 3% for the SVX data is not included in  $\delta_{\text{tot}}$

$Q^2$ GeV <sup>2</sup>	$x$	$y$	$\sigma_r$	$\delta_{\text{tot}}$ %	$\delta_{\text{stat}}$ %	$\delta_{\text{uncor}}$ %	$\gamma_{E'_e}$ %	$\gamma_{\theta_e}$ %	$\gamma_{E_{\text{had}}}$ %	$\gamma_{\text{noise}}$ %	$\gamma_{E_{\text{SpaCal}}^h}$ %	$\gamma_{\gamma p}$ %
0.20	$3.980 \times 10^{-5}$	$4.948 \times 10^{-2}$	0.249	20.3	13.8	12.0	0.58	-1.74	5.70	-0.34	-1.37	-6.44
0.20	$2.510 \times 10^{-4}$	$7.845 \times 10^{-3}$	0.162	16.7	14.2	6.19	1.38	-0.78	-1.65	-3.64	-4.21	-1.68
0.25	$3.980 \times 10^{-5}$	$6.184 \times 10^{-2}$	0.302	17.5	9.80	11.3	0.49	-2.22	3.10	-1.48	-2.62	-7.69
0.25	$2.510 \times 10^{-4}$	$9.806 \times 10^{-3}$	0.163	14.1	10.8	4.71	-1.93	0.70	0.01	-4.47	-5.71	-1.42
0.25	$1.580 \times 10^{-3}$	$1.558 \times 10^{-3}$	0.182	13.2	11.5	5.29	0.57	0.46	-1.73	-1.93	-2.61	-0.30
0.35	$5.120 \times 10^{-6}$	$6.726 \times 10^{-1}$	0.458	25.2	21.6	12.8	-0.61	-0.51	0.34	-0.03	0.59	-2.45
0.35	$3.200 \times 10^{-5}$	$1.077 \times 10^{-1}$	0.361	22.2	9.72	11.1	-2.17	-0.08	-1.61	0.54	-6.88	-14.78
0.35	$1.300 \times 10^{-4}$	$2.651 \times 10^{-2}$	0.265	11.6	9.61	4.38	-0.38	0.27	2.55	-2.99	-0.51	-2.46
0.35	$5.000 \times 10^{-4}$	$6.892 \times 10^{-3}$	0.216	11.1	9.22	4.19	-0.91	-0.81	-0.47	-3.51	-2.48	-0.53
0.35	$2.510 \times 10^{-3}$	$1.373 \times 10^{-3}$	0.193	11.6	10.2	4.55	-1.19	-0.25	-0.04	-2.49	-1.47	-0.08
0.50	$7.320 \times 10^{-6}$	$6.726 \times 10^{-1}$	0.483	10.0	5.23	5.74	0.18	1.96	2.31	-0.18	2.75	-4.84
0.50	$1.580 \times 10^{-5}$	$3.116 \times 10^{-1}$	0.477	21.6	18.6	9.84	-3.86	-2.83	0.27	0.03	0.47	-0.19
0.50	$3.980 \times 10^{-5}$	$1.237 \times 10^{-1}$	0.431	17.7	10.7	6.07	-2.11	0.82	-1.48	-0.10	-4.88	-11.49
0.50	$1.000 \times 10^{-4}$	$4.923 \times 10^{-2}$	0.388	11.0	9.10	4.87	-0.30	0.57	-0.02	0.52	-3.39	-1.75
0.50	$2.510 \times 10^{-4}$	$1.961 \times 10^{-2}$	0.262	12.8	10.6	4.45	0.01	-1.43	0.66	-4.32	-3.28	-1.27
0.50	$8.000 \times 10^{-4}$	$6.154 \times 10^{-3}$	0.275	9.51	7.92	3.86	-0.40	-0.43	0.04	-3.41	-0.90	-0.22
0.65	$9.520 \times 10^{-6}$	$6.726 \times 10^{-1}$	0.502	6.22	3.87	2.90	-1.15	0.68	1.11	-0.18	1.85	-2.98
0.65	$1.580 \times 10^{-5}$	$4.050 \times 10^{-1}$	0.474	6.68	3.06	5.44	-0.63	-2.05	0.24	-0.09	0.34	-0.92
0.65	$3.980 \times 10^{-5}$	$1.608 \times 10^{-1}$	0.681	21.7	17.4	11.2	-6.22	2.19	-0.04	0.04	-0.15	0.00
0.65	$1.000 \times 10^{-4}$	$6.400 \times 10^{-2}$	0.424	13.2	5.59	5.85	-1.89	-2.22	-1.17	0.52	-9.22	-3.52
0.65	$2.510 \times 10^{-4}$	$2.550 \times 10^{-2}$	0.353	10.6	8.94	4.04	-0.78	-1.00	-0.48	0.49	-3.39	-1.53
0.65	$8.000 \times 10^{-4}$	$8.000 \times 10^{-3}$	0.283	10.5	7.57	3.61	-1.74	0.53	1.06	-5.94	-0.75	-0.15
0.65	$3.200 \times 10^{-3}$	$2.000 \times 10^{-3}$	0.246	10.1	8.92	4.05	-1.83	0.36	-0.68	1.63	-0.36	-0.09
0.85	$1.244 \times 10^{-5}$	$6.726 \times 10^{-1}$	0.594	5.01	2.48	2.52	-1.16	-0.22	1.23	-0.17	1.77	-2.55
0.85	$2.000 \times 10^{-5}$	$4.184 \times 10^{-1}$	0.623	6.24	1.94	5.36	-0.98	-2.27	0.16	-0.03	0.34	-0.45
0.85	$3.980 \times 10^{-5}$	$2.103 \times 10^{-1}$	0.564	6.24	2.03	5.37	-0.98	-2.23	0.01	-0.08	0.00	-0.05
0.85	$1.000 \times 10^{-4}$	$8.369 \times 10^{-2}$	0.493	7.75	4.98	5.78	-0.38	-0.81	0.16	-0.77	0.63	0.00
0.85	$2.510 \times 10^{-4}$	$3.334 \times 10^{-2}$	0.353	11.3	8.06	3.75	0.57	-1.86	-1.56	0.17	-6.37	-1.05
0.85	$8.000 \times 10^{-4}$	$1.046 \times 10^{-2}$	0.325	8.86	6.77	3.41	-0.19	-0.32	1.16	-4.25	-1.20	-0.26
0.85	$3.200 \times 10^{-3}$	$2.615 \times 10^{-3}$	0.318	8.65	7.27	3.78	0.55	-1.91	1.43	-1.05	-0.73	-0.04
1.20	$1.757 \times 10^{-5}$	$6.726 \times 10^{-1}$	0.652	5.82	2.66	2.51	-1.08	-0.35	1.33	-0.26	2.16	-3.57
1.20	$2.000 \times 10^{-5}$	$5.907 \times 10^{-1}$	0.686	3.95	2.59	2.51	-0.73	-0.46	0.40	-0.04	0.91	-0.93
1.20	$3.200 \times 10^{-5}$	$3.692 \times 10^{-1}$	0.697	3.78	1.66	2.73	-0.81	-1.73	0.22	-0.10	0.09	-0.59
1.20	$6.310 \times 10^{-5}$	$1.872 \times 10^{-1}$	0.653	4.12	1.37	2.71	-1.17	-2.50	0.07	-0.22	0.22	-0.02
1.20	$1.580 \times 10^{-4}$	$7.478 \times 10^{-2}$	0.498	4.40	2.06	2.78	0.69	-2.07	0.70	-1.43	0.35	0.00
1.20	$3.980 \times 10^{-4}$	$2.969 \times 10^{-2}$	0.471	7.52	5.21	3.16	-2.04	0.11	-1.35	-0.02	-3.65	-0.10
1.20	$1.300 \times 10^{-3}$	$9.088 \times 10^{-3}$	0.378	6.85	5.08	3.09	-2.10	-0.39	1.38	-2.00	-1.05	-0.03
1.20	$5.000 \times 10^{-3}$	$2.363 \times 10^{-3}$	0.322	8.23	6.55	3.54	-1.54	-1.25	2.10	1.84	-0.71	0.00

**Table 11** Reduced cross section  $\sigma_r$ , as measured with the SVX data sample for  $1.5 \leq Q^2 \leq 3.5 \text{ GeV}^2$ . The uncertainties are quoted in % relative to  $\sigma_r$ .  $\delta_{\text{tot}}$  is the total uncertainty determined as the quadratic sum of systematic and statistical uncertainties.  $\delta_{\text{stat}}$  is the statistical uncertainty.  $\delta_{\text{uncor}}$  represents the uncorrelated systematic uncertainty.  $\gamma_{E'_e}$ ,  $\gamma_{\theta_e}$ ,  $\gamma_{E_{\text{had}}}$ ,  $\gamma_{\text{noise}}$ ,  $\gamma_{E_{\text{SpaCal}}^h}$  and  $\gamma_{\gamma p}$  are the bin-to-bin correlated systematic uncertainties in the cross section measurement due to uncertainties in the SpaCal electromagnetic energy scale, electron scattering angle, LAr calorimeter hadronic energy scale, LAr calorimeter noise, SpaCal hadronic energy scale and the photoproduction background, respectively. The luminosity uncertainty of 3% for the SVX data is not included in  $\delta_{\text{tot}}$

$Q^2$ GeV <sup>2</sup>	$x$	$y$	$\sigma_r$	$\delta_{\text{tot}}$ %	$\delta_{\text{stat}}$ %	$\delta_{\text{uncor}}$ %	$\gamma_{E'_e}$ %	$\gamma_{\theta_e}$ %	$\gamma_{E_{\text{had}}}$ %	$\gamma_{\text{noise}}$ %	$\gamma_{E_{\text{SpaCal}}^h}$ %	$\gamma_{\gamma p}$ %
1.50	$2.196 \times 10^{-5}$	$6.726 \times 10^{-1}$	0.722	4.43	2.45	2.47	-1.08	-0.58	0.81	-0.20	1.37	-1.86
1.50	$3.200 \times 10^{-5}$	$4.615 \times 10^{-1}$	0.774	3.28	1.78	2.36	-0.63	-0.76	0.39	-0.10	0.65	-0.68
1.50	$5.000 \times 10^{-5}$	$2.954 \times 10^{-1}$	0.773	3.80	1.46	2.71	-0.93	-2.02	0.01	-0.09	-0.04	-0.13
1.50	$8.000 \times 10^{-5}$	$1.846 \times 10^{-1}$	0.727	3.92	1.57	2.73	-0.84	-2.17	0.04	-0.18	0.16	-0.02
1.50	$1.300 \times 10^{-4}$	$1.136 \times 10^{-1}$	0.654	4.31	1.77	2.75	-0.94	-2.57	0.18	-0.54	0.28	-0.01
1.50	$2.000 \times 10^{-4}$	$7.384 \times 10^{-2}$	0.628	5.58	3.57	2.77	-3.21	-0.43	0.45	-0.15	0.00	0.00
1.50	$3.200 \times 10^{-4}$	$4.615 \times 10^{-2}$	0.564	4.78	1.90	2.76	-0.45	-2.40	-1.13	0.11	-2.08	-0.14
1.50	$8.000 \times 10^{-4}$	$1.846 \times 10^{-2}$	0.483	4.32	2.38	2.47	-1.61	-0.99	0.33	-1.23	-1.30	-0.02
1.50	$3.200 \times 10^{-3}$	$4.615 \times 10^{-3}$	0.424	5.02	2.69	2.56	-1.41	-0.56	2.17	-2.06	-0.31	0.00
1.50	$1.300 \times 10^{-2}$	$1.136 \times 10^{-3}$	0.384	14.1	4.49	3.05	-1.71	-0.37	1.16	12.8	-0.33	0.00
2.00	$2.928 \times 10^{-5}$	$6.726 \times 10^{-1}$	0.822	4.28	2.19	2.39	-0.61	-0.93	1.07	-0.18	1.51	-1.75
2.00	$5.000 \times 10^{-5}$	$3.938 \times 10^{-1}$	0.837	3.10	1.62	2.33	-0.84	-0.76	0.27	-0.22	0.20	-0.30
2.00	$8.000 \times 10^{-5}$	$2.461 \times 10^{-1}$	0.791	3.03	1.63	2.34	-0.94	-0.32	0.29	-0.15	0.00	-0.05
2.00	$1.300 \times 10^{-4}$	$1.515 \times 10^{-1}$	0.731	3.28	1.81	2.36	-1.33	-0.07	0.37	-0.12	0.00	-0.01
2.00	$2.000 \times 10^{-4}$	$9.846 \times 10^{-2}$	0.700	3.58	1.97	2.39	-1.73	-0.28	0.46	-0.11	0.00	-0.01
2.00	$3.200 \times 10^{-4}$	$6.154 \times 10^{-2}$	0.578	4.39	2.14	2.40	-0.73	-0.65	-0.78	-0.16	-2.71	-0.03
2.00	$5.000 \times 10^{-4}$	$3.938 \times 10^{-2}$	0.528	3.95	2.41	2.43	-1.46	-0.07	-0.61	-0.28	-1.16	-0.01
2.00	$1.000 \times 10^{-3}$	$1.969 \times 10^{-2}$	0.490	3.79	1.86	2.36	-1.38	-0.11	0.67	-1.62	-0.61	-0.01
2.00	$3.200 \times 10^{-3}$	$6.154 \times 10^{-3}$	0.424	4.65	1.63	2.34	-1.35	-0.07	2.41	-2.41	-0.25	0.00
2.00	$1.300 \times 10^{-2}$	$1.515 \times 10^{-3}$	0.404	10.5	2.46	2.48	-1.12	-0.52	0.95	9.81	-0.25	0.00
2.50	$5.000 \times 10^{-5}$	$4.923 \times 10^{-1}$	0.881	3.68	2.28	2.40	-0.96	-0.47	0.65	-0.18	0.68	-0.75
2.50	$8.000 \times 10^{-5}$	$3.077 \times 10^{-1}$	0.869	3.08	1.66	2.34	-0.80	-0.74	0.30	0.03	0.04	-0.14
2.50	$1.300 \times 10^{-4}$	$1.893 \times 10^{-1}$	0.800	3.04	1.63	2.34	-0.85	-0.53	0.33	-0.03	0.00	-0.01
2.50	$2.000 \times 10^{-4}$	$1.231 \times 10^{-1}$	0.777	3.25	1.63	2.34	-1.44	-0.47	0.36	-0.16	0.00	-0.01
2.50	$3.200 \times 10^{-4}$	$7.692 \times 10^{-2}$	0.683	4.03	1.71	2.35	-2.69	-0.52	0.48	-0.15	0.00	-0.01
2.50	$5.000 \times 10^{-4}$	$4.923 \times 10^{-2}$	0.601	3.45	1.90	2.36	0.15	-0.85	-0.10	-0.81	-1.14	-0.01
2.50	$8.000 \times 10^{-4}$	$3.077 \times 10^{-2}$	0.574	3.31	1.96	2.38	-0.23	-0.41	0.35	-0.95	-0.49	0.00
2.50	$1.580 \times 10^{-3}$	$1.558 \times 10^{-2}$	0.527	3.99	1.44	2.32	-0.20	-0.42	1.17	-2.60	-0.27	0.00
2.50	$5.000 \times 10^{-3}$	$4.923 \times 10^{-3}$	0.448	4.10	1.29	2.31	-0.19	-0.58	2.66	-1.53	-0.21	0.00
2.50	$2.000 \times 10^{-2}$	$1.231 \times 10^{-3}$	0.409	16.8	2.30	2.44	-0.14	-0.63	0.73	16.4	-0.18	0.00
3.50	$8.000 \times 10^{-5}$	$4.307 \times 10^{-1}$	0.971	3.75	2.35	2.42	-1.09	-1.15	0.32	-0.14	0.22	-0.25
3.50	$1.300 \times 10^{-4}$	$2.651 \times 10^{-1}$	0.925	3.21	1.81	2.36	-0.50	-1.04	0.34	-0.05	0.00	-0.05
3.50	$2.000 \times 10^{-4}$	$1.723 \times 10^{-1}$	0.852	3.20	1.78	2.35	-1.02	-0.64	0.35	-0.08	0.00	-0.02
3.50	$3.200 \times 10^{-4}$	$1.077 \times 10^{-1}$	0.779	3.44	1.80	2.36	-1.53	-0.71	0.40	-0.14	0.00	-0.01
3.50	$5.000 \times 10^{-4}$	$6.892 \times 10^{-2}$	0.716	3.49	1.96	2.38	0.39	-0.73	0.02	-0.88	-1.11	-0.01
3.50	$8.000 \times 10^{-4}$	$4.307 \times 10^{-2}$	0.651	3.59	2.02	2.38	0.36	-0.66	0.45	-1.45	-0.56	0.00
3.50	$1.300 \times 10^{-3}$	$2.651 \times 10^{-2}$	0.588	3.65	2.09	2.39	0.36	-0.88	0.37	-1.46	-0.30	0.00
3.50	$2.510 \times 10^{-3}$	$1.373 \times 10^{-2}$	0.566	4.57	1.48	2.33	0.23	-0.63	1.87	-3.04	-0.22	0.00
3.50	$8.000 \times 10^{-3}$	$4.307 \times 10^{-3}$	0.481	3.76	1.38	2.32	0.30	-0.73	2.48	0.20	-0.17	0.00

**Table 12** Reduced cross section  $\sigma_r$ , as measured with the NVX-BST data sample for  $0.5 \leq Q^2 \leq 3.5$  GeV<sup>2</sup>. The uncertainties are quoted in % relative to  $\sigma_r$ .  $\delta_{\text{tot}}$  is the total uncertainty determined as the quadratic sum of systematic and statistical uncertainties.  $\delta_{\text{stat}}$  is the statistical uncertainty.  $\delta_{\text{uncor}}$  represents the uncorrelated systematic uncertainty.  $\gamma_{E'_e}$ ,  $\gamma_{\theta_e}$ ,  $\gamma_{E_{\text{had}}}$ ,  $\gamma_{\text{noise}}$ ,  $\gamma_{E_{\text{SpaCal}}^h}$  and  $\gamma_{\gamma p}$  are the bin-to-bin correlated systematic uncertainties in the cross section measurement due to uncertainties in the SpaCal electromagnetic energy scale, electron scattering angle, LAr calorimeter hadronic energy scale, LAr calorimeter noise, SpaCal hadronic energy scale and the photoproduction background, respectively. The luminosity uncertainty of 1.1% for the NVX data is not included in  $\delta_{\text{tot}}$

$Q^2$ GeV <sup>2</sup>	$x$	$y$	$\sigma_r$	$\delta_{\text{tot}}$ %	$\delta_{\text{stat}}$ %	$\delta_{\text{uncor}}$ %	$\gamma_{E'_e}$ %	$\gamma_{\theta_e}$ %	$\gamma_{E_{\text{had}}}$ %	$\gamma_{\text{noise}}$ %	$\gamma_{E_{\text{SpaCal}}^h}$ %	$\gamma_{\gamma p}$ %
0.50	$2.510 \times 10^{-4}$	$1.968 \times 10^{-2}$	0.334	19.6	14.4	10.0	1.91	-1.41	1.76	0.43	-6.60	-4.90
0.50	$8.000 \times 10^{-4}$	$6.176 \times 10^{-3}$	0.266	11.7	9.14	6.46	-0.46	-0.75	-1.13	-2.77	-0.84	-1.10
0.50	$3.200 \times 10^{-3}$	$1.544 \times 10^{-3}$	0.184	13.5	11.3	6.39	-0.76	0.65	-0.94	0.61	-3.15	-0.59
0.65	$2.510 \times 10^{-4}$	$2.559 \times 10^{-2}$	0.385	14.2	10.8	6.38	-0.77	0.64	0.25	-2.71	-5.02	-3.39
0.65	$8.000 \times 10^{-4}$	$8.029 \times 10^{-3}$	0.315	8.75	6.62	4.88	0.06	0.57	-1.69	-1.78	-1.52	-0.46
0.65	$3.200 \times 10^{-3}$	$2.007 \times 10^{-3}$	0.209	9.47	7.68	4.59	-0.03	0.68	-0.76	-2.43	-1.64	-0.14
0.85	$1.000 \times 10^{-4}$	$8.399 \times 10^{-2}$	0.523	20.5	14.2	5.30	-1.12	-0.62	-0.92	-1.13	-4.02	-13.04
0.85	$2.510 \times 10^{-4}$	$3.346 \times 10^{-2}$	0.428	11.9	9.45	4.93	-0.63	0.71	0.07	-1.49	-3.32	-3.71
0.85	$8.000 \times 10^{-4}$	$1.050 \times 10^{-2}$	0.359	8.15	6.42	4.13	-0.51	0.22	-0.98	-1.97	-0.54	-1.63
0.85	$3.200 \times 10^{-3}$	$2.625 \times 10^{-3}$	0.302	7.22	5.82	3.98	-0.36	0.27	-0.90	-0.10	-1.17	-0.11
1.20	$1.757 \times 10^{-5}$	$6.750 \times 10^{-1}$	0.563	10.1	6.54	3.79	-1.95	1.82	-0.15	-0.16	1.00	-6.00
1.20	$1.580 \times 10^{-4}$	$7.505 \times 10^{-2}$	0.542	15.8	10.2	4.06	-0.24	0.26	-0.90	-0.93	-7.76	-8.15
1.20	$3.980 \times 10^{-4}$	$2.979 \times 10^{-2}$	0.501	8.02	6.08	4.14	0.00	0.38	0.18	-0.94	-2.70	-1.37
1.20	$1.300 \times 10^{-3}$	$9.121 \times 10^{-3}$	0.364	7.27	4.98	4.45	0.07	-0.11	-1.48	-2.36	-0.50	-0.50
1.20	$5.000 \times 10^{-3}$	$2.372 \times 10^{-3}$	0.295	7.64	6.03	3.75	1.51	-0.06	-1.63	0.84	-1.51	-0.25
1.50	$2.196 \times 10^{-5}$	$6.750 \times 10^{-1}$	0.703	5.78	3.08	2.53	-0.95	0.49	-0.10	-0.11	0.90	-3.94
1.50	$3.200 \times 10^{-5}$	$4.632 \times 10^{-1}$	0.706	8.41	6.46	4.21	-0.66	2.58	-0.07	-0.09	0.67	-1.95
1.50	$3.200 \times 10^{-4}$	$4.632 \times 10^{-2}$	0.565	10.7	7.50	3.18	-1.08	0.09	-0.14	-0.68	-5.64	-3.71
1.50	$1.000 \times 10^{-3}$	$1.482 \times 10^{-2}$	0.459	6.94	5.24	3.74	-1.41	0.73	-0.93	-1.45	-1.04	-0.44
1.50	$3.200 \times 10^{-3}$	$4.632 \times 10^{-3}$	0.390	6.13	4.43	3.29	-0.53	0.04	-2.05	-1.51	-0.63	0.00
1.50	$1.300 \times 10^{-2}$	$1.140 \times 10^{-3}$	0.331	11.5	6.93	4.32	1.21	-0.49	-1.26	7.65	-1.98	0.00
2.00	$2.928 \times 10^{-5}$	$6.750 \times 10^{-1}$	0.788	4.45	2.00	2.28	-1.08	0.19	-0.13	-0.11	1.10	-2.85
2.00	$5.000 \times 10^{-5}$	$3.953 \times 10^{-1}$	0.792	5.31	4.25	2.58	-0.91	1.42	-0.16	-0.08	0.29	-0.73
2.00	$3.200 \times 10^{-4}$	$6.176 \times 10^{-2}$	0.645	12.2	3.48	2.70	-2.66	1.50	0.91	0.92	-10.8	-1.58
2.00	$1.000 \times 10^{-3}$	$1.976 \times 10^{-2}$	0.527	5.93	4.55	3.36	0.77	-0.05	-0.20	-0.41	-1.43	-0.52
2.00	$3.200 \times 10^{-3}$	$6.176 \times 10^{-3}$	0.426	5.80	3.93	3.06	-0.63	0.51	-2.41	-1.00	-1.16	-0.05
2.00	$1.300 \times 10^{-2}$	$1.520 \times 10^{-3}$	0.372	9.24	5.78	3.79	-0.68	0.63	-0.80	5.80	-1.55	0.00
2.50	$3.660 \times 10^{-5}$	$6.750 \times 10^{-1}$	0.857	4.42	2.29	2.29	-0.70	-0.32	-0.21	-0.12	0.96	-2.73
2.50	$5.000 \times 10^{-5}$	$4.941 \times 10^{-1}$	0.856	3.39	1.99	2.26	-1.01	0.00	-0.19	-0.10	0.52	-1.05
2.50	$8.000 \times 10^{-5}$	$3.088 \times 10^{-1}$	0.839	3.01	1.63	2.29	-0.76	0.66	-0.27	-0.05	0.12	-0.23
2.50	$1.300 \times 10^{-4}$	$1.900 \times 10^{-1}$	0.759	4.67	2.73	2.62	-1.39	2.32	-0.31	0.00	0.00	-0.05
2.50	$2.000 \times 10^{-4}$	$1.235 \times 10^{-1}$	0.756	7.06	4.84	3.65	-1.19	3.38	-0.38	0.00	0.00	-0.10
2.50	$5.000 \times 10^{-4}$	$4.941 \times 10^{-2}$	0.651	8.65	1.99	2.36	-2.61	1.76	0.86	1.25	-7.27	-0.55
2.50	$1.580 \times 10^{-3}$	$1.564 \times 10^{-2}$	0.511	5.86	3.52	2.92	-2.34	2.37	-0.16	0.61	-1.40	-0.10
2.50	$5.000 \times 10^{-3}$	$4.941 \times 10^{-3}$	0.451	5.91	3.27	2.82	-1.43	2.21	-2.87	-0.75	-0.79	0.00
3.50	$5.124 \times 10^{-5}$	$6.750 \times 10^{-1}$	0.935	4.27	2.17	2.25	-0.87	-0.14	-0.16	-0.11	1.03	-2.57
3.50	$8.000 \times 10^{-5}$	$4.323 \times 10^{-1}$	0.947	2.89	1.49	2.20	-0.85	-0.20	-0.20	-0.09	0.38	-0.57
3.50	$1.300 \times 10^{-4}$	$2.660 \times 10^{-1}$	0.908	2.63	1.21	2.21	-0.67	0.00	-0.35	-0.01	0.00	-0.07
3.50	$2.000 \times 10^{-4}$	$1.729 \times 10^{-1}$	0.879	2.83	1.42	2.26	-0.83	0.35	-0.30	0.00	0.00	-0.03
3.50	$3.200 \times 10^{-4}$	$1.081 \times 10^{-1}$	0.775	3.60	1.75	2.32	-1.70	1.21	-0.45	0.00	0.00	0.00
3.50	$8.000 \times 10^{-4}$	$4.323 \times 10^{-2}$	0.651	4.34	1.08	2.20	-1.44	0.67	0.30	0.38	-3.17	-0.12
3.50	$2.510 \times 10^{-3}$	$1.378 \times 10^{-2}$	0.533	3.64	1.66	2.31	-1.54	1.14	-0.80	-0.19	-0.89	-0.01
3.50	$8.000 \times 10^{-3}$	$4.323 \times 10^{-3}$	0.433	4.44	1.68	2.31	-1.56	1.20	-2.71	0.46	-0.36	-0.01



**Table 13** Reduced cross section  $\sigma_r$ , as measured with the NVX-BST data sample for  $5 \leq Q^2 \leq 12 \text{ GeV}^2$ . The uncertainties are quoted in % relative to  $\sigma_r$ .  $\delta_{\text{tot}}$  is the total uncertainty determined as the quadratic sum of systematic and statistical uncertainties.  $\delta_{\text{stat}}$  is the statistical uncertainty.  $\delta_{\text{uncor}}$  represents the uncorrelated systematic uncertainty.  $\gamma_{E'_e}$ ,  $\gamma_{\theta_e}$ ,  $\gamma_{E_{\text{had}}}$ ,  $\gamma_{\text{noise}}$ ,  $\gamma_{E_{\text{SpaCal}}^h}$  and  $\gamma_{\gamma p}$  are the bin-to-bin correlated systematic uncertainties in the cross section measurement due to uncertainties in the SpaCal electromagnetic energy scale, electron scattering angle, LAr calorimeter hadronic energy scale, LAr calorimeter noise, SpaCal hadronic energy scale and the photoproduction background, respectively. The luminosity uncertainty of 1.1% for the NVX data is not included in  $\delta_{\text{tot}}$

$Q^2$ GeV <sup>2</sup>	x	y	$\sigma_r$	$\delta_{\text{tot}}$ %	$\delta_{\text{stat}}$ %	$\delta_{\text{uncor}}$ %	$\gamma_{E'_e}$ %	$\gamma_{\theta_e}$ %	$\gamma_{E_{\text{had}}}$ %	$\gamma_{\text{noise}}$ %	$\gamma_{E_{\text{SpaCal}}^h}$ %	$\gamma_{\gamma p}$ %
5.00	$7.320 \times 10^{-5}$	$6.750 \times 10^{-1}$	1.052	3.26	1.60	2.21	-0.75	-0.31	-0.22	-0.12	0.84	-1.33
5.00	$1.300 \times 10^{-4}$	$3.801 \times 10^{-1}$	1.066	2.72	1.33	2.20	-0.79	-0.32	-0.26	-0.07	0.09	-0.14
5.00	$2.000 \times 10^{-4}$	$2.470 \times 10^{-1}$	1.009	2.62	1.13	2.20	-0.75	-0.22	-0.40	0.00	0.00	-0.03
5.00	$3.200 \times 10^{-4}$	$1.544 \times 10^{-1}$	0.911	2.79	1.20	2.21	-1.15	-0.17	-0.32	0.00	0.00	-0.01
5.00	$5.000 \times 10^{-4}$	$9.881 \times 10^{-2}$	0.838	3.11	1.27	2.22	-1.72	-0.04	-0.40	0.00	0.00	0.00
5.00	$8.000 \times 10^{-4}$	$6.176 \times 10^{-2}$	0.775	3.50	1.29	2.23	-0.27	-0.09	0.17	-0.40	-2.32	-0.02
5.00	$1.300 \times 10^{-3}$	$3.801 \times 10^{-2}$	0.686	2.91	1.39	2.24	-0.46	0.07	-0.18	-0.53	-0.99	-0.04
5.00	$2.000 \times 10^{-3}$	$2.470 \times 10^{-2}$	0.636	2.84	1.45	2.26	-0.69	0.26	-0.24	-0.06	-0.53	-0.01
5.00	$3.980 \times 10^{-3}$	$1.241 \times 10^{-2}$	0.569	3.18	1.08	2.20	-0.50	-0.04	-1.73	-0.86	-0.33	-0.01
5.00	$1.300 \times 10^{-2}$	$3.801 \times 10^{-3}$	0.440	3.90	1.13	2.20	-0.43	0.05	-2.50	1.62	-0.26	0.00
6.50	$9.515 \times 10^{-5}$	$6.750 \times 10^{-1}$	1.050	4.71	2.96	2.31	-0.65	-0.19	-0.20	-0.14	0.82	-2.63
6.50	$1.300 \times 10^{-4}$	$4.941 \times 10^{-1}$	1.122	2.98	1.67	2.22	-0.80	-0.45	-0.23	-0.11	0.37	-0.31
6.50	$2.000 \times 10^{-4}$	$3.211 \times 10^{-1}$	1.122	2.70	1.25	2.20	-0.84	-0.24	-0.31	-0.03	0.02	-0.06
6.50	$3.200 \times 10^{-4}$	$2.007 \times 10^{-1}$	1.024	2.70	1.19	2.20	-0.85	-0.40	-0.39	0.00	0.00	-0.01
6.50	$5.000 \times 10^{-4}$	$1.285 \times 10^{-1}$	0.937	2.79	1.22	2.21	-1.08	-0.41	-0.31	0.00	0.00	-0.01
6.50	$8.000 \times 10^{-4}$	$8.029 \times 10^{-2}$	0.865	3.50	1.25	2.22	-2.31	-0.51	-0.39	0.00	0.00	0.00
6.50	$1.300 \times 10^{-3}$	$4.941 \times 10^{-2}$	0.780	3.06	1.32	2.23	0.19	-0.22	-0.41	-0.96	-1.20	-0.03
6.50	$2.000 \times 10^{-3}$	$3.211 \times 10^{-2}$	0.691	2.80	1.36	2.24	0.48	-0.55	-0.03	-0.33	-0.59	0.00
6.50	$3.980 \times 10^{-3}$	$1.614 \times 10^{-2}$	0.618	2.79	1.00	2.19	0.07	-0.22	-1.09	-0.82	-0.28	0.00
6.50	$1.300 \times 10^{-2}$	$4.941 \times 10^{-3}$	0.497	3.52	0.98	2.18	0.03	-0.24	-2.39	0.89	-0.24	0.00
8.50	$1.244 \times 10^{-4}$	$6.750 \times 10^{-1}$	1.207	3.60	2.26	2.28	-0.65	-0.33	-0.21	-0.12	0.88	-1.15
8.50	$2.000 \times 10^{-4}$	$4.200 \times 10^{-1}$	1.176	2.87	1.52	2.22	-0.90	-0.27	-0.22	-0.09	0.20	-0.14
8.50	$3.200 \times 10^{-4}$	$2.625 \times 10^{-1}$	1.097	2.76	1.29	2.21	-0.94	-0.31	-0.30	0.00	0.00	-0.01
8.50	$5.000 \times 10^{-4}$	$1.680 \times 10^{-1}$	1.036	2.71	1.30	2.22	-0.71	-0.39	-0.28	0.00	0.00	0.00
8.50	$8.000 \times 10^{-4}$	$1.050 \times 10^{-1}$	0.959	3.05	1.32	2.23	-1.53	-0.30	-0.38	0.00	0.00	0.00
8.50	$1.300 \times 10^{-3}$	$6.461 \times 10^{-2}$	0.837	3.13	1.41	2.24	0.43	-0.55	-0.26	-0.97	-1.14	0.00
8.50	$2.000 \times 10^{-3}$	$4.200 \times 10^{-2}$	0.784	2.89	1.43	2.25	0.47	-0.47	-0.20	-0.53	-0.68	0.00
8.50	$3.200 \times 10^{-3}$	$2.625 \times 10^{-2}$	0.679	2.91	1.49	2.26	0.37	-0.44	-0.45	-0.66	-0.42	0.00
8.50	$6.310 \times 10^{-3}$	$1.331 \times 10^{-2}$	0.621	3.09	1.08	2.20	0.16	-0.34	-1.59	-0.89	-0.29	0.00
8.50	$2.000 \times 10^{-2}$	$4.200 \times 10^{-3}$	0.464	3.99	1.20	2.21	0.41	-0.50	-1.77	2.45	-0.27	0.00
12.00	$8.000 \times 10^{-4}$	$1.482 \times 10^{-1}$	1.067	3.05	1.45	2.25	-1.40	-0.34	-0.24	0.00	0.00	0.00
12.00	$1.300 \times 10^{-3}$	$9.121 \times 10^{-2}$	0.938	3.31	1.54	2.26	0.48	-0.36	-0.29	-0.80	-1.54	-0.01
12.00	$2.000 \times 10^{-3}$	$5.929 \times 10^{-2}$	0.850	3.00	1.58	2.27	0.47	-0.42	-0.08	-0.67	-0.67	0.00
12.00	$3.200 \times 10^{-3}$	$3.706 \times 10^{-2}$	0.752	2.98	1.63	2.29	0.44	-0.39	-0.40	-0.55	-0.40	0.00
12.00	$6.310 \times 10^{-3}$	$1.879 \times 10^{-2}$	0.650	2.89	1.21	2.22	0.46	-0.47	-0.91	-0.77	-0.31	0.00
12.00	$2.000 \times 10^{-2}$	$5.929 \times 10^{-3}$	0.494	3.45	1.25	2.22	0.54	-0.56	-1.75	1.32	-0.26	0.00

**Table 14** Reduced cross section  $\sigma_r$ , as measured with the NVX-S9 data sample. The uncertainties are quoted in % relative to  $\sigma_r$ .  $\delta_{\text{tot}}$  is the total uncertainty determined as the quadratic sum of systematic and statistical uncertainties.  $\delta_{\text{stat}}$  is the statistical uncertainty.  $\delta_{\text{uncor}}$  represents the uncorrelated systematic uncertainty.  $\gamma_{E'_e}$ ,  $\gamma_{\theta_e}$ ,  $\gamma_{E_{\text{had}}}$ ,  $\gamma_{\text{noise}}$ ,  $\gamma_{E_{\text{SpaCal}}^h}$  and  $\gamma_{\gamma p}$  are the bin-to-bin correlated systematic uncertainties in the cross section measurement due to uncertainties in the SpaCal electromagnetic energy scale, electron scattering angle, LAr calorimeter hadronic energy scale, LAr calorimeter noise, SpaCal hadronic energy scale and the photoproduction background, respectively. The luminosity uncertainty of 1.1% for the NVX data is not included in  $\delta_{\text{tot}}$

$Q^2$ GeV <sup>2</sup>	$x$	$y$	$\sigma_r$	$\delta_{\text{tot}}$ %	$\delta_{\text{stat}}$ %	$\delta_{\text{uncor}}$ %	$\gamma_{E'_e}$ %	$\gamma_{\theta_e}$ %	$\gamma_{E_{\text{had}}}$ %	$\gamma_{\text{noise}}$ %	$\gamma_{E_{\text{SpaCal}}^h}$ %	$\gamma_{\gamma p}$ %
1.50	$1.853 \times 10^{-5}$	$8.000 \times 10^{-1}$	0.605	12.0	3.18	3.48	0.49	0.81	-0.02	0.20	1.19	-10.97
2.00	$2.470 \times 10^{-5}$	$8.000 \times 10^{-1}$	0.756	9.23	2.35	2.70	-1.47	1.36	-0.03	0.12	2.15	-7.98
2.50	$3.088 \times 10^{-5}$	$8.000 \times 10^{-1}$	0.837	7.11	2.46	2.67	-1.17	-0.44	-0.05	0.21	0.12	-5.98
3.50	$4.323 \times 10^{-5}$	$8.000 \times 10^{-1}$	0.871	7.99	3.10	2.83	-0.86	-0.56	0.62	-0.04	2.32	-6.28
5.00	$6.176 \times 10^{-5}$	$8.000 \times 10^{-1}$	0.993	7.70	3.12	2.78	-1.70	-0.72	-0.72	0.14	0.50	-6.13
6.50	$8.029 \times 10^{-5}$	$8.000 \times 10^{-1}$	1.080	6.42	3.11	2.64	-0.55	0.91	0.00	-0.46	-1.62	-4.54
8.50	$1.050 \times 10^{-4}$	$8.000 \times 10^{-1}$	1.174	6.22	3.73	2.80	-0.28	1.06	-0.89	0.00	-1.12	-3.71

**Table 15** Combined H1 reduced cross section  $\sigma_r^{\text{ave}}$  for  $0.2 \leq Q^2 \leq 1.5$  GeV<sup>2</sup>. The uncertainties are quoted in % relative to  $\sigma_r^{\text{ave}}$ .  $F_L^{\text{th}}$  represents the structure function  $F_L$  used for the CME correction (see (32)) and to calculate the structure function  $F_2$ .  $\delta_{\text{ave,stat}}$  ( $\delta_{\text{ave,uncor}}$ ) represents the statistical (uncorrelated systematic) uncertainty.  $\delta_{\text{ave,tot}}$  is the total uncertainty calculated as a sum of uncorrelated uncertainty and all correlated sources in quadrature. A global normalisation uncertainty of 0.5% is not included in  $\delta_{\text{ave,tot}}$ . CME stands for the centre-of-mass energy of the measurement

#	$Q^2$ GeV <sup>2</sup>	$x$	$y$	$F_L^{\text{th}}$	$\sigma_r^{\text{ave}}$	$F_2$	$\delta_{\text{ave,stat}}$ %	$\delta_{\text{ave,uncor}}$ %	$\delta_{\text{ave,tot}}$ %	CME GeV
1	0.2	$0.398 \times 10^{-4}$	0.050	0.08	0.230	0.230	14.3	12.0	19.98	319
2	0.2	$0.251 \times 10^{-3}$	0.008	0.06	0.190	0.190	13.1	6.18	15.03	319
3	0.25	$0.398 \times 10^{-4}$	0.062	0.09	0.300	0.300	9.84	11.3	16.82	319
4	0.25	$0.251 \times 10^{-3}$	0.010	0.07	0.191	0.191	10.00	4.70	12.05	319
5	0.25	$0.158 \times 10^{-2}$	0.002	0.06	0.203	0.203	10.8	5.29	12.37	301
6	0.35	$0.512 \times 10^{-5}$	0.675	-	0.450	-	21.7	12.8	25.34	319
7	0.35	$0.610 \times 10^{-5}$	0.634	-	0.357	-	5.74	11.0	13.50	301
8	0.35	$0.320 \times 10^{-4}$	0.108	0.12	0.410	0.411	9.12	11.1	20.36	319
9	0.35	$0.130 \times 10^{-3}$	0.027	0.10	0.264	0.264	9.62	4.38	10.99	319
10	0.35	$0.500 \times 10^{-3}$	0.007	0.08	0.237	0.237	8.81	4.19	10.08	319
11	0.35	$0.251 \times 10^{-2}$	0.001	0.07	0.204	0.204	9.93	4.55	11.08	319
12	0.5	$0.732 \times 10^{-5}$	0.675	-	0.449	-	5.42	5.74	9.44	319
13	0.5	$0.860 \times 10^{-5}$	0.642	-	0.442	-	3.75	9.17	10.69	301
14	0.5	$0.158 \times 10^{-4}$	0.313	0.16	0.461	0.472	19.0	9.84	21.61	319
15	0.5	$0.398 \times 10^{-4}$	0.124	0.15	0.478	0.480	10.1	6.07	16.25	319
16	0.5	$0.100 \times 10^{-3}$	0.049	0.13	0.411	0.411	8.85	4.87	10.57	319
17	0.5	$0.251 \times 10^{-3}$	0.020	0.11	0.296	0.296	8.37	4.20	9.74	319
18	0.5	$0.800 \times 10^{-3}$	0.006	0.10	0.280	0.280	5.92	3.44	7.07	319
19	0.5	$0.320 \times 10^{-2}$	0.002	0.08	0.183	0.183	11.4	6.39	13.12	301
20	0.65	$0.952 \times 10^{-5}$	0.675	-	0.479	-	3.96	2.90	5.85	319
21	0.65	$0.112 \times 10^{-4}$	0.641	-	0.504	-	3.74	8.21	9.89	301

**Table 15** (Continued)

#	$Q^2$ GeV <sup>2</sup>	$x$	$y$	$F_L^{\text{th}}$	$\sigma_T^{\text{ave}}$	$F_2$	$\delta_{\text{ave,stat}}$ %	$\delta_{\text{ave,uncor}}$ %	$\delta_{\text{ave,tot}}$ %	CME GeV
22	0.65	$0.158 \times 10^{-4}$	0.407	0.20	0.466	0.490	3.09	5.44	6.51	319
23	0.65	$0.164 \times 10^{-4}$	0.438	0.19	0.510	0.538	3.02	7.28	8.33	301
24	0.65	$0.398 \times 10^{-4}$	0.161	0.17	0.678	0.681	17.5	11.2	21.16	319
25	0.65	$0.100 \times 10^{-3}$	0.064	0.15	0.500	0.500	5.14	5.84	10.70	319
26	0.65	$0.251 \times 10^{-3}$	0.026	0.13	0.376	0.376	6.79	3.46	7.98	319
27	0.65	$0.800 \times 10^{-3}$	0.008	0.11	0.308	0.308	4.94	3.02	6.17	319
28	0.65	$0.320 \times 10^{-2}$	0.002	0.09	0.225	0.225	5.81	3.15	6.76	319
29	0.85	$0.124 \times 10^{-4}$	0.675	–	0.565	–	2.54	2.52	4.50	319
30	0.85	$0.138 \times 10^{-4}$	0.675	–	0.614	–	5.20	9.45	12.17	301
31	0.85	$0.200 \times 10^{-4}$	0.420	0.22	0.612	0.641	1.96	5.36	5.99	319
32	0.85	$0.200 \times 10^{-4}$	0.469	0.22	0.596	0.634	2.65	4.98	6.27	301
33	0.85	$0.398 \times 10^{-4}$	0.211	0.20	0.567	0.573	1.65	3.39	4.13	319
34	0.85	$0.500 \times 10^{-4}$	0.168	0.20	0.546	0.549	2.92	4.52	5.97	319
35	0.85	$0.100 \times 10^{-3}$	0.084	0.18	0.499	0.500	2.78	3.59	5.98	319
36	0.85	$0.251 \times 10^{-3}$	0.033	0.15	0.414	0.414	5.88	2.98	7.31	319
37	0.85	$0.800 \times 10^{-3}$	0.010	0.13	0.350	0.350	4.61	2.66	5.60	319
38	0.85	$0.320 \times 10^{-2}$	0.003	0.11	0.307	0.307	4.56	2.81	5.49	301
39	1.2	$0.176 \times 10^{-4}$	0.675	–	0.608	–	2.54	2.14	4.65	319
40	1.2	$0.200 \times 10^{-4}$	0.593	–	0.671	–	2.62	2.51	3.94	319
41	1.2	$0.200 \times 10^{-4}$	0.663	–	0.741	–	3.60	8.36	9.98	301
42	1.2	$0.320 \times 10^{-4}$	0.371	0.26	0.689	0.714	1.67	2.73	3.55	319
43	1.2	$0.320 \times 10^{-4}$	0.414	0.26	0.705	0.738	2.68	4.55	5.83	301
44	1.2	$0.631 \times 10^{-4}$	0.188	0.23	0.647	0.652	1.18	2.25	3.09	319
45	1.2	$0.800 \times 10^{-4}$	0.148	0.22	0.594	0.597	2.18	4.02	5.24	319
46	1.2	$0.130 \times 10^{-3}$	0.091	0.21	0.543	0.544	2.43	4.97	5.78	319
47	1.2	$0.158 \times 10^{-3}$	0.075	0.20	0.503	0.504	1.67	2.30	3.24	319
48	1.2	$0.398 \times 10^{-3}$	0.030	0.17	0.502	0.502	2.88	2.67	4.26	319
49	1.2	$0.130 \times 10^{-2}$	0.009	0.14	0.374	0.374	3.58	2.62	4.74	319
50	1.2	$0.500 \times 10^{-2}$	0.002	0.12	0.298	0.298	4.51	2.60	5.47	319
51	1.5	$0.185 \times 10^{-4}$	0.800	–	0.610	–	3.17	3.48	7.93	319
52	1.5	$0.220 \times 10^{-4}$	0.675	–	0.702	–	1.94	1.78	3.31	319
53	1.5	$0.320 \times 10^{-4}$	0.463	0.29	0.756	0.804	1.77	2.12	3.08	319
54	1.5	$0.320 \times 10^{-4}$	0.518	0.29	0.801	0.864	1.20	3.20	4.47	301
55	1.5	$0.500 \times 10^{-4}$	0.296	0.27	0.759	0.775	1.06	1.97	2.62	319
56	1.5	$0.800 \times 10^{-4}$	0.185	0.25	0.699	0.705	1.26	2.15	2.95	319
57	1.5	$0.130 \times 10^{-3}$	0.114	0.23	0.643	0.644	1.49	2.42	3.32	319
58	1.5	$0.200 \times 10^{-3}$	0.074	0.22	0.615	0.616	2.40	2.59	3.97	319
59	1.5	$0.320 \times 10^{-3}$	0.046	0.20	0.584	0.584	1.60	2.18	3.30	319
60	1.5	$0.500 \times 10^{-3}$	0.030	0.19	0.548	0.548	2.51	7.05	7.74	319
61	1.5	$0.800 \times 10^{-3}$	0.019	0.17	0.495	0.495	2.35	2.47	3.80	319
62	1.5	$0.100 \times 10^{-2}$	0.015	0.17	0.463	0.463	5.22	3.74	6.61	319
63	1.5	$0.320 \times 10^{-2}$	0.005	0.14	0.409	0.409	2.32	2.03	3.51	301
64	1.5	$0.130 \times 10^{-1}$	0.001	0.11	0.327	0.327	3.99	2.49	7.00	319





**Table 17** Combined H1 reduced cross section  $\sigma_r^{\text{ave}}$  for  $2 \leq Q^2 \leq 5 \text{ GeV}^2$ . The uncertainties are quoted in % relative to  $\sigma_r^{\text{ave}}$ .  $F_L^{\text{th}}$  represents the structure function  $F_L$  used for the CME correction (see (32)) and to calculate the structure function  $F_2$ .  $\delta_{\text{ave,stat}}$  ( $\delta_{\text{ave,uncor}}$ ) represents the statistical (uncorrelated systematic) uncertainty.  $\delta_{\text{ave,tot}}$  is the total uncertainty calculated as a sum of uncorrelated uncertainty and all correlated sources in quadrature. A global normalisation uncertainty of 0.5% is not included in  $\delta_{\text{ave,tot}}$ . CME stands for the centre-of-mass energy of the measurement

#	$Q^2$ GeV <sup>2</sup>	$x$	$y$	$F_L^{\text{th}}$	$\sigma_r^{\text{ave}}$	$F_2$	$\delta_{\text{ave,stat}}$ %	$\delta_{\text{ave,uncor}}$ %	$\delta_{\text{ave,tot}}$ %	CME GeV
65	2.0	$0.247 \times 10^{-4}$	0.800	–	0.775	–	2.32	2.70	6.03	319
66	2.0	$0.293 \times 10^{-4}$	0.675	–	0.792	–	1.49	1.65	2.86	319
67	2.0	$0.327 \times 10^{-4}$	0.675	–	0.839	–	1.82	5.21	6.34	301
68	2.0	$0.500 \times 10^{-4}$	0.395	0.32	0.825	0.861	1.61	1.86	2.71	319
69	2.0	$0.500 \times 10^{-4}$	0.442	0.32	0.856	0.903	0.92	2.45	3.00	301
70	2.0	$0.800 \times 10^{-4}$	0.247	0.29	0.768	0.780	0.91	1.64	2.19	319
71	2.0	$0.130 \times 10^{-3}$	0.152	0.27	0.726	0.730	1.05	1.69	2.32	319
72	2.0	$0.200 \times 10^{-3}$	0.099	0.25	0.679	0.680	1.09	1.78	2.51	319
73	2.0	$0.320 \times 10^{-3}$	0.062	0.23	0.634	0.635	1.15	1.55	2.49	319
74	2.0	$0.500 \times 10^{-3}$	0.040	0.21	0.578	0.578	1.33	1.94	2.83	319
75	2.0	$0.100 \times 10^{-2}$	0.020	0.19	0.510	0.510	1.15	1.69	2.42	319
76	2.0	$0.320 \times 10^{-2}$	0.006	0.15	0.424	0.424	1.26	1.78	2.77	319
77	2.0	$0.130 \times 10^{-1}$	0.002	0.12	0.361	0.361	2.40	2.11	5.34	301
78	2.5	$0.309 \times 10^{-4}$	0.800	–	0.835	–	2.46	2.67	5.06	319
79	2.5	$0.366 \times 10^{-4}$	0.675	–	0.860	–	2.29	2.29	3.74	319
80	2.5	$0.409 \times 10^{-4}$	0.675	–	0.920	–	1.56	6.21	6.98	301
81	2.5	$0.500 \times 10^{-4}$	0.494	0.35	0.861	0.930	1.51	1.65	2.51	319
82	2.5	$0.500 \times 10^{-4}$	0.552	0.35	0.895	0.984	1.20	2.09	3.13	301
83	2.5	$0.800 \times 10^{-4}$	0.309	0.32	0.856	0.877	0.69	1.17	1.72	319
84	2.5	$0.130 \times 10^{-3}$	0.190	0.30	0.795	0.801	0.73	1.14	1.73	319
85	2.5	$0.200 \times 10^{-3}$	0.124	0.27	0.758	0.760	0.92	1.53	2.09	319
86	2.5	$0.320 \times 10^{-3}$	0.077	0.25	0.671	0.672	0.92	1.68	2.28	319
87	2.5	$0.500 \times 10^{-3}$	0.049	0.23	0.630	0.631	0.90	1.39	2.09	319
88	2.5	$0.800 \times 10^{-3}$	0.031	0.21	0.578	0.578	1.02	1.77	2.30	319
89	2.5	$0.158 \times 10^{-2}$	0.016	0.19	0.534	0.534	0.87	1.54	2.13	319
90	2.5	$0.500 \times 10^{-2}$	0.005	0.16	0.439	0.439	1.01	1.69	2.59	319
91	2.5	$0.200 \times 10^{-1}$	0.001	0.12	0.342	0.342	2.52	2.45	8.69	319
92	3.5	$0.432 \times 10^{-4}$	0.800	–	0.877	–	3.09	2.83	5.75	319
93	3.5	$0.512 \times 10^{-4}$	0.675	–	0.940	–	2.16	2.25	3.61	319
94	3.5	$0.573 \times 10^{-4}$	0.675	–	0.931	–	2.00	6.18	6.94	301
95	3.5	$0.800 \times 10^{-4}$	0.432	0.38	0.954	1.007	1.29	1.64	2.33	319
96	3.5	$0.800 \times 10^{-4}$	0.483	0.38	0.950	1.020	1.00	1.75	2.67	301
97	3.5	$0.130 \times 10^{-3}$	0.266	0.35	0.918	0.934	0.66	1.06	1.60	319
98	3.5	$0.200 \times 10^{-3}$	0.173	0.32	0.859	0.865	0.69	1.07	1.64	319
99	3.5	$0.320 \times 10^{-3}$	0.108	0.29	0.800	0.802	0.74	1.12	1.70	319
100	3.5	$0.500 \times 10^{-3}$	0.069	0.27	0.759	0.760	0.83	1.31	1.91	319
101	3.5	$0.800 \times 10^{-3}$	0.043	0.25	0.661	0.662	0.69	1.15	1.71	319
102	3.5	$0.130 \times 10^{-2}$	0.027	0.22	0.626	0.626	0.89	1.36	1.98	319
103	3.5	$0.251 \times 10^{-2}$	0.014	0.20	0.556	0.556	0.64	1.11	1.69	319
104	3.5	$0.800 \times 10^{-2}$	0.004	0.16	0.448	0.448	0.84	1.48	2.32	319
105	5.0	$0.618 \times 10^{-4}$	0.800	–	0.990	–	3.13	2.78	5.61	319
106	5.0	$0.732 \times 10^{-4}$	0.675	–	1.056	–	1.60	2.21	3.02	319
107	5.0	$0.818 \times 10^{-4}$	0.675	–	1.047	–	2.08	4.85	6.07	301
108	5.0	$0.130 \times 10^{-3}$	0.380	0.41	1.066	1.108	1.33	2.20	2.76	319

**Table 17** (Continued)

#	$Q^2$ GeV <sup>2</sup>	$x$	$y$	$F_L^{\text{th}}$	$\sigma_r^{\text{ave}}$	$F_2$	$\delta_{\text{ave,stat}}$ %	$\delta_{\text{ave,uncor}}$ %	$\delta_{\text{ave,tot}}$ %	CME GeV
109	5.0	$0.130 \times 10^{-3}$	0.425	0.41	1.053	1.108	1.02	1.68	2.28	301
110	5.0	$0.200 \times 10^{-3}$	0.247	0.37	1.011	1.025	0.74	1.19	1.75	319
111	5.0	$0.320 \times 10^{-3}$	0.154	0.34	0.931	0.936	0.80	1.28	1.81	319
112	5.0	$0.500 \times 10^{-3}$	0.099	0.31	0.839	0.841	0.80	1.28	1.83	319
113	5.0	$0.800 \times 10^{-3}$	0.062	0.28	0.753	0.754	0.82	1.29	1.84	319
114	5.0	$0.130 \times 10^{-2}$	0.038	0.25	0.696	0.696	0.85	1.31	1.93	319
115	5.0	$0.200 \times 10^{-2}$	0.025	0.23	0.639	0.639	0.88	1.31	1.89	319
116	5.0	$0.398 \times 10^{-2}$	0.012	0.20	0.569	0.569	0.67	1.22	1.81	319
117	5.0	$0.130 \times 10^{-1}$	0.004	0.16	0.438	0.438	0.80	1.82	2.60	319

the fractal model fit with constant  $R$ , gives the best description of the H1 data. However, a sufficiently softer rise of  $F_2$  together with a smaller  $F_L$ , as predicted by the IIM model, also describes the data well. For the GBW model, the rise of  $F_2$  is rather steep such that the fit to the data prefers a larger  $F_L$ , which is inconsistent with the prediction of the model.

## 12 Summary

A new measurement is performed of the inclusive double differential cross section for neutral current deep inelastic positron-proton scattering,  $e^+p \rightarrow e^+X$ , in the region of small Bjorken  $x$  and low absolute momentum transfers squared,  $Q^2$ . The data were obtained with the H1 detector at the  $ep$  collider HERA in two dedicated periods of data taking at beam energies  $E_e = 27.5$  GeV and  $E_p = 920$  GeV. In the year 1999, events were collected with a dedicated trigger on low  $Q^2$  DIS events at the nominal interaction vertex position, corresponding to an integrated luminosity of  $2.1 \text{ pb}^{-1}$ . In the year 2000, the interaction vertex was shifted forward by +70 cm in proton beam direction to access even smaller values of  $Q^2$ , and data with an integrated luminosity of  $0.505 \text{ pb}^{-1}$  were taken.

The measurement is performed in a wide range of inelasticity  $y$ , from 0.0015 to 0.8, and of Bjorken  $x$ , from  $5 \cdot 10^{-6}$  to 0.02. The data cover a  $Q^2$  range from 0.2 to  $12 \text{ GeV}^2$ , with an overlap region of the nominal and the shifted vertex data of  $0.5 \leq Q^2 \leq 3.5 \text{ GeV}^2$ , in which both measurements agree. At low  $Q^2$  the data analysed here comprise the full statistics collected with the H1 experiment at 920 GeV.

The measurement obtained with the 1999 and the 2000 data is combined with data collected in the years 1995 and 1997, which were taken at 820 GeV proton beam energy in similar experimental conditions and published previously. This combination takes the correlation of systematic uncertainties into account and provides a new, single data set from

the H1 experiment, which supersedes all H1 data previously released in that kinematic region. The total uncertainty of the final reduced cross section measurement is about 2% for a large part of the phase space.

The neutral current  $ep$  cross section at low  $Q^2$  is governed by two independent proton structure functions,  $F_2$  and  $F_L$ . For  $y < 0.6$ , the influence of the longitudinal structure function  $F_L$  is small, and the data in this range are also presented as a measurement of the proton structure function  $F_2(x, Q^2)$ . For  $y = 0.735$ , using a method based on the derivative of the cross section with respect to  $\ln y$ , the structure function  $F_L(x, Q^2)$  is extracted with minimum assumptions on the behaviour of  $F_2$ .

In each  $Q^2$  bin a simple parameterisation of the reduced cross section in terms of a power law of  $F_2(x, Q^2) \propto x^{-\lambda}$  and  $R = F_L/(F_2 - F_L)$  describes the data well. The power  $\lambda$  increases approximately logarithmically with  $Q^2$  at  $Q^2 \gtrsim 2 \text{ GeV}^2$ . The parameterisation is consistent with a constant value of  $R(x, Q^2) \simeq 0.5$ , which implies that  $F_L(x, Q^2) \simeq F_2(x, Q^2)/3$  under the assumption of a power law rise of  $F_2$  towards low  $x$ .

The transition region of DIS to photoproduction,  $Q^2 \simeq 1 \text{ GeV}^2$ , cannot be analysed within perturbative QCD. The data therefore are studied here within phenomenological models. The structure function  $F_2(x, Q^2)$  is analysed using a self similarity based ansatz within a fractal model. The fractal  $F_2$  parameterisation, combined with a constant  $R$ , provides a good description of the measured cross section in the full range of phase space covered by the data.

The Colour Dipole Model predicts both structure functions  $F_2$  and  $F_L$  using a single characteristic dipole scattering cross section. Two versions of the CDM, the GBW model and the IIM model, are used in this analysis and are found to generally describe the cross section data well. The description of the data in the GBW model is observed to improve when the contribution of  $F_L$  within this model is formally allowed to be enhanced. The IIM model prediction





Table 18 (Continued)

#	$\gamma_1^{ave}$ %	$\gamma_2^{ave}$ %	$\gamma_3^{ave}$ %	$\gamma_4^{ave}$ %	$\gamma_5^{ave}$ %	$\gamma_6^{ave}$ %	$\gamma_7^{ave}$ %	$\gamma_8^{ave}$ %	$\gamma_9^{ave}$ %	$\gamma_{10}^{ave}$ %	$\gamma_{11}^{ave}$ %	$\gamma_{12}^{ave}$ %	$\gamma_{13}^{ave}$ %	$\gamma_{14}^{ave}$ %	$\gamma_{15}^{ave}$ %	$\gamma_{16}^{ave}$ %	$\gamma_{17}^{ave}$ %	$\gamma_{18}^{ave}$ %	$\gamma_{19}^{ave}$ %	$\gamma_{20}^{ave}$ %	$\gamma_{21}^{ave}$ %	$\gamma_{22}^{ave}$ %	$\gamma_{23}^{ave}$ %	$\gamma_{24}^{ave}$ %	$\gamma_{25}^{ave}$ %	$\gamma_{26}^{ave}$ %
97	-8.46	0.45	0.45	0.25	-0.21	-0.25	0.26	-0.89	1.48	3.17	1.40	0.21	-0.75	-0.57	-1.26	-0.85	2.42	-0.34	0.36	-0.74	-0.34	0.85	0.38	0.41	-1.01	0.02
98	-8.47	-0.38	-0.20	0.03	-0.35	-0.01	0.35	-0.85	1.88	2.98	1.95	-0.16	-1.34	-0.72	-1.28	-0.90	2.75	-0.51	0.31	-0.49	-0.32	1.42	0.76	-0.01	-0.98	0.01
99	-8.47	0.04	0.10	0.80	0.60	-0.57	2.40	0.24	1.00	2.66	0.64	1.12	-2.14	-1.13	-1.21	-0.37	0.66	-1.14	-0.75	1.72	1.15	-0.39	2.18	-0.46	-1.08	0.26
100	-8.47	-0.18	-0.33	0.41	0.06	0.24	1.86	0.51	1.55	4.08	1.34	1.52	1.16	-0.32	-2.45	-1.01	-0.25	0.37	-0.48	0.96	0.46	-1.75	2.10	0.32	-2.32	0.35
101	-8.47	-0.29	-0.52	0.32	-0.40	0.43	1.67	-0.08	-2.43	1.47	1.20	0.91	1.19	0.55	-1.52	-0.51	2.95	-0.05	1.24	0.03	-0.74	-0.26	2.94	1.35	-0.03	0.12
102	-8.47	-0.03	-0.43	0.67	0.14	1.08	3.36	0.94	1.64	4.21	0.60	2.20	-0.18	0.05	-2.05	-0.41	-0.26	0.14	-0.52	0.70	-0.20	-1.09	2.18	0.31	-2.32	0.42
103	-8.47	-0.18	-0.37	0.72	0.48	-0.45	3.39	0.87	-0.43	2.59	1.47	1.43	-1.28	0.33	-2.77	1.08	1.78	0.08	0.34	1.03	-1.51	-0.62	1.96	0.68	-1.20	0.44
104	-8.48	-0.12	0.68	2.99	3.46	-7.43	0.68	5.19	4.35	3.65	-0.92	2.05	-3.06	1.30	-3.22	0.14	3.08	-1.61	0.05	0.10	-0.13	0.73	0.11	0.59	0.44	1.53
105	-8.46	1.80	4.92	-14.97	2.59	-1.94	-2.92	2.30	1.72	14.68	-5.70	1.97	-9.50	0.82	9.43	-2.10	11.20	17.94	-11.17	5.22	0.25	-1.82	-1.08	1.70	2.67	-0.99
106	-8.46	0.50	1.24	-4.03	0.10	0.05	-0.67	-0.67	0.33	3.67	-0.41	1.63	-2.41	-0.96	2.76	1.49	2.55	3.52	-3.39	2.73	0.06	-0.40	-2.26	0.00	0.83	-0.17
107	-8.66	19.06	14.15	5.00	3.27	3.75	-3.04	-2.46	0.80	3.95	1.40	-5.04	1.88	-5.00	-3.91	-0.38	7.23	0.85	2.97	-2.86	-2.95	4.10	-0.70	1.67	-2.10	-1.62
108	-8.46	0.04	0.14	-0.41	-0.13	-0.54	0.28	-0.74	-0.67	2.96	1.41	2.03	-0.01	-1.63	1.27	1.54	0.48	-0.21	-0.63	1.62	-0.07	-0.01	-1.03	0.39	1.29	-0.09
109	-8.51	2.68	2.06	0.99	0.37	-0.45	-0.48	-0.85	0.05	2.70	1.99	-0.99	-0.54	-1.07	-1.83	-1.01	3.54	0.06	1.14	-1.47	-1.32	1.98	0.36	1.11	-2.17	-1.38
110	-8.46	-0.04	0.00	0.10	-0.23	-0.48	0.02	-0.94	1.92	3.66	2.58	0.32	-0.60	-1.15	-1.10	-0.31	1.76	-0.26	0.36	-0.29	-0.74	1.08	0.20	0.90	-1.19	-1.02
111	-8.46	-0.05	-0.01	0.61	0.35	-1.54	0.83	0.12	-1.36	2.69	0.93	1.92	-0.43	-1.04	-0.39	0.65	-0.41	-0.39	-0.19	2.04	0.67	-1.07	1.36	0.55	-1.14	-0.75
112	-8.47	-0.17	-0.13	0.42	0.10	-1.25	0.56	-0.32	-0.92	3.65	1.67	1.70	-0.43	-1.17	-0.75	0.83	0.54	-0.74	-0.12	2.12	0.51	-0.91	1.31	0.70	-1.10	-0.84
113	-8.47	-0.20	-0.40	0.66	-0.05	-0.45	1.66	-0.58	-0.76	2.03	1.70	1.40	0.58	-0.79	-1.28	0.20	-1.27	0.84	0.77	0.67	0.92	-0.84	3.05	1.21	-0.81	-0.89
114	-8.47	-0.10	-0.57	0.25	-0.22	1.30	3.40	-0.59	0.98	3.05	2.16	2.04	0.21	-0.91	-1.49	0.95	-1.13	0.84	0.89	2.09	1.16	-1.42	2.54	0.88	-1.46	-0.95
115	-8.47	-0.30	-0.47	-0.23	-0.72	0.43	1.45	-1.12	-2.73	0.58	1.64	0.76	0.18	0.15	-0.83	0.34	2.86	0.57	2.39	1.24	-0.30	-0.08	1.12	0.90	-1.02	-0.89
116	-8.47	-0.07	-0.26	1.33	1.09	-1.28	3.77	1.55	0.41	4.00	1.27	2.10	-1.76	-0.70	-2.08	-0.30	-1.38	0.41	0.59	1.64	0.85	-0.61	1.06	0.65	-1.22	-0.90
117	-8.48	-0.12	0.86	2.97	3.00	-7.66	-1.74	4.35	5.83	4.88	-1.40	1.72	-3.17	-0.97	0.24	-4.68	-1.40	-1.78	1.56	2.23	-1.66	-0.25	-0.32	0.67	0.69	-0.50

**Table 19** Combined H1 reduced cross section  $\sigma_r^{\text{ave}}$  for  $6.5 \leq Q^2 \leq 12 \text{ GeV}^2$ . The uncertainties are quoted in % relative to  $\sigma_r^{\text{ave}}$ .  $F_L^{\text{th}}$  represents the structure function  $F_L$  used for the CME correction (see (32)) and to calculate the structure function  $F_2$ .  $\delta_{\text{ave,stat}}$  ( $\delta_{\text{ave,uncor}}$ ) represents the statistical (uncorrelated systematic) uncertainty.  $\delta_{\text{ave,tot}}$  is the total uncertainty calculated as a sum of uncorrelated uncertainty and all correlated sources in quadrature. A global normalisation uncertainty of 0.5% is not included in  $\delta_{\text{ave,tot}}$ . CME stands for the centre-of-mass energy of the measurement

#	$Q^2$ GeV <sup>2</sup>	$x$	$y$	$F_L^{\text{th}}$	$\sigma_r^{\text{ave}}$	$F_2$	$\delta_{\text{ave,stat}}$ %	$\delta_{\text{ave,uncor}}$ %	$\delta_{\text{ave,tot}}$ %	CME GeV
118	6.5	$0.803 \times 10^{-4}$	0.800	–	1.083	–	3.11	2.64	4.85	319
119	6.5	$0.951 \times 10^{-4}$	0.675	–	1.053	–	2.95	2.31	4.16	319
120	6.5	$0.130 \times 10^{-3}$	0.494	0.45	1.123	1.211	1.67	2.22	2.97	319
121	6.5	$0.130 \times 10^{-3}$	0.552	0.45	1.124	1.239	1.53	1.73	3.03	301
122	6.5	$0.200 \times 10^{-3}$	0.321	0.41	1.123	1.152	1.25	2.20	2.72	319
123	6.5	$0.200 \times 10^{-3}$	0.359	0.41	1.117	1.155	1.09	1.62	2.24	301
124	6.5	$0.320 \times 10^{-3}$	0.201	0.37	1.006	1.015	0.84	1.16	1.75	319
125	6.5	$0.500 \times 10^{-3}$	0.128	0.34	0.936	0.939	0.86	1.26	1.86	319
126	6.5	$0.800 \times 10^{-3}$	0.080	0.31	0.854	0.855	0.87	1.26	1.91	319
127	6.5	$0.130 \times 10^{-2}$	0.049	0.28	0.758	0.758	0.90	1.28	1.87	319
128	6.5	$0.200 \times 10^{-2}$	0.032	0.26	0.694	0.694	0.92	1.29	1.89	319
129	6.5	$0.398 \times 10^{-2}$	0.016	0.22	0.616	0.617	0.69	1.19	1.76	319
130	6.5	$0.130 \times 10^{-1}$	0.005	0.18	0.482	0.482	0.73	1.80	2.44	319
131	8.5	$0.105 \times 10^{-3}$	0.800	–	1.178	–	3.72	2.80	5.20	319
132	8.5	$0.124 \times 10^{-3}$	0.675	–	1.211	–	2.26	2.28	3.44	319
133	8.5	$0.139 \times 10^{-3}$	0.675	–	1.136	–	2.07	1.82	4.54	301
134	8.5	$0.200 \times 10^{-3}$	0.420	0.46	1.178	1.239	1.52	2.22	2.88	319
135	8.5	$0.200 \times 10^{-3}$	0.469	0.46	1.182	1.261	1.38	1.64	2.59	301
136	8.5	$0.320 \times 10^{-3}$	0.262	0.41	1.112	1.131	0.91	1.25	1.86	319
137	8.5	$0.500 \times 10^{-3}$	0.168	0.37	1.033	1.039	0.95	1.18	1.81	319
138	8.5	$0.800 \times 10^{-3}$	0.105	0.34	0.950	0.953	0.95	1.28	1.90	319
139	8.5	$0.130 \times 10^{-2}$	0.065	0.30	0.842	0.842	0.99	1.30	1.94	319
140	8.5	$0.200 \times 10^{-2}$	0.042	0.28	0.773	0.773	1.00	1.30	1.93	319
141	8.5	$0.320 \times 10^{-2}$	0.026	0.25	0.663	0.663	1.04	1.32	1.99	319
142	8.5	$0.631 \times 10^{-2}$	0.013	0.22	0.604	0.604	0.79	1.24	1.83	319
143	8.5	$0.200 \times 10^{-1}$	0.004	0.17	0.456	0.456	0.88	1.82	2.67	319
144	12.0	$0.800 \times 10^{-3}$	0.148	0.38	1.053	1.058	1.07	1.30	1.99	319
145	12.0	$0.130 \times 10^{-2}$	0.091	0.34	0.923	0.924	1.10	1.30	1.97	319
146	12.0	$0.200 \times 10^{-2}$	0.059	0.31	0.861	0.861	1.11	1.33	2.00	319
147	12.0	$0.320 \times 10^{-2}$	0.037	0.28	0.757	0.757	1.14	1.34	2.02	319
148	12.0	$0.631 \times 10^{-2}$	0.019	0.24	0.646	0.646	0.88	1.24	1.86	319
149	12.0	$0.200 \times 10^{-1}$	0.006	0.19	0.490	0.490	0.93	1.83	2.51	319

on  $F_L$  is similar to the GBW model. Owing to a softer rise of  $F_2$  towards small  $x$ , the IIM ansatz yet is able to describe the cross section data better and no modification on the predicted  $F_L$  is suggested by the data.

For the region  $0.2 \text{ GeV}^2 \leq Q^2 \leq 12 \text{ GeV}^2$ , in which the transition from photoproduction to DIS takes place and the changeover from the non-perturbative to the perturbative QCD regime can be explored, the data as presented in

this paper are the most precise result of the H1 Collaboration.

**Acknowledgements** We are grateful to the HERA machine group whose outstanding efforts have made this experiment possible. We thank the engineers and technicians for their work in constructing and maintaining the H1 detector, our funding agencies for financial support, the DESY technical staff for continual assistance and the DESY directorate for support and for the hospitality which they extend to the non DESY members of the collaboration.



**Table 21** Orthogonal transition matrix  $U_{jk}$  from the original ( $b_{E'_e}$ , etc.) to the diagonalised ( $b_{E'_e}^{\text{ave}}$ ,  $b_{26}^{\text{ave}}$ ) systematic sources for the averaged HI data. The matrix elements are given in %

	NVX			SVX			NVX-97			SVX-95		
	$b_{E'_e}$	$b_{\theta_e}$	$b_{L}$	$b_{E'_e}$	$b_{\theta_e}$	$b_{L}$	$b_{E'_e}$	$b_{\theta_e}$	$b_{L}$	$b_{E'_e}$	$b_{\theta_e}$	$b_{L}$
	$b_{E'_e}^{\text{had}}$	$b_{\text{noise}}$	$b_{E_{\text{SpICal}}^h}$	$b_{E'_e}^{\text{had}}$	$b_{\text{noise}}$	$b_{E_{\text{SpICal}}^h}$	$b_{E'_e}^{\text{had}}$	$b_{\text{noise}}$	$b_{E_{\text{had}}}$	$b_{E'_e}$	$b_{\theta_e}$	$b_{L}$
$\delta_1$	0.0	0.0	0.0	0.0	0.0	0.0	0.0	0.0	0.0	0.0	0.0	0.0
$\delta_2$	0.5	1.3	-1.1	0.5	1.3	-3.2	0.9	-2.6	-10.8	-0.5	0.0	1.9
$\delta_3$	0.6	1.7	0.7	4.3	2.7	-8.3	1.1	0.7	-1.2	2.4	2.2	0.4
$\delta_4$	-1.1	-4.5	14.6	1.2	-7.6	27.0	-5.4	-0.7	2.7	10.6	2.5	2.2
$\delta_5$	-0.3	0.6	14.5	1.9	-1.9	-3.9	-4.9	-9.1	-8.4	26.1	1.8	-21.6
$\delta_6$	4.4	10.2	-29.0	-13.9	4.0	-1.2	6.2	10.7	22.1	-48.5	-9.6	28.9
$\delta_7$	-0.2	6.7	8.0	-27.6	-8.2	4.6	2.3	-27.8	-21.3	10.7	-16.7	-26.1
$\delta_8$	-1.1	3.0	25.2	6.8	-3.7	-4.2	-13.8	27.2	72.9	12.5	8.5	-8.7
$\delta_9$	22.9	24.9	9.6	35.1	5.5	-7.7	14.7	3.3	-4.9	27.5	21.8	-0.8
$\delta_{10}$	-45.6	-44.5	36.1	-10.8	-5.8	-14.4	-20.2	10.0	-16.1	-11.4	-6.7	14.4
$\delta_{11}$	-15.0	-12.7	-1.5	-22.9	-5.5	18.8	5.7	-26.6	33.1	7.4	-10.9	-35.9
$\delta_{12}$	-12.5	-25.6	3.8	5.1	0.2	4.3	11.3	43.0	-23.5	5.9	8.2	11.7
$\delta_{13}$	0.0	-25.9	-29.4	13.0	-12.3	23.3	4.1	42.7	-7.1	-8.2	17.5	-61.3
$\delta_{14}$	11.8	22.2	4.3	-1.7	-2.0	-9.5	-10.3	33.6	-27.6	8.1	3.8	2.2
$\delta_{15}$	-4.7	-51.0	-25.6	49.9	7.0	-17.9	7.0	-37.7	9.3	3.3	18.7	11.7
$\delta_{16}$	-21.6	-7.1	-31.2	-29.5	15.8	12.2	13.0	16.2	11.5	64.6	-5.7	32.4
$\delta_{17}$	-42.7	26.2	-7.8	14.5	9.2	-29.3	-16.2	-1.6	-1.8	18.8	19.5	-10.3
$\delta_{18}$	43.2	-28.0	10.2	-27.1	-8.3	-68.0	6.8	8.2	6.9	12.4	-6.8	-12.4
$\delta_{19}$	28.2	-13.7	44.6	10.9	-19.1	38.3	0.0	-7.1	1.8	8.9	18.4	25.5
$\delta_{20}$	-28.0	20.4	30.4	17.2	31.3	-8.7	17.2	-4.5	0.4	-14.8	-3.8	-17.4
$\delta_{21}$	-4.1	5.8	-6.0	-40.2	-3.3	-3.4	-4.3	-18.8	-3.0	-8.1	81.0	1.7
$\delta_{22}$	6.1	-9.3	-1.9	-14.5	-4.7	7.9	2.4	-2.4	-8.7	-4.6	15.6	-1.6
$\delta_{23}$	-4.0	13.9	-26.0	18.5	-66.4	-6.0	-19.3	-7.5	0.1	11.0	-13.2	6.9
$\delta_{24}$	-13.7	10.0	-0.1	1.6	-35.7	-9.8	9.1	-3.2	-4.9	-3.2	5.1	5.4
$\delta_{25}$	-28.4	7.5	18.0	-3.2	-45.0	-9.8	39.7	3.5	4.8	-3.4	1.5	2.7
$\delta_{26}$	5.8	-7.2	-1.2	-0.3	7.5	8.5	-2.0	-19.7	-20.0	16.0	-18.6	-7.1

**Appendix: Averaging procedure**

The  $\chi^2$  function of (28) is to be minimised with respect to the sets  $m^i$  and  $b_j$ . This determines the averaged measurements and uncertainties,  $\mu^{i,ave}$ ,  $\Delta_{i,ave}$ ,  $\alpha_{j,ave}$  and the matrix  $A'_S$ , used in (29).

The minimum  $\chi^2_{min}$  in (28) is found by solving a system of linear equations obtained by requiring  $\partial\chi^2/\partial m^i = 0$  and  $\partial\chi^2/\partial b_j = 0$  which can be written in matrix form

$$\begin{pmatrix} A_M & A_{SM} \\ (A_{SM})^T & A_S \end{pmatrix} \cdot \begin{pmatrix} M^{ave} \\ B^{ave} \end{pmatrix} = \begin{pmatrix} C_M \\ C_S \end{pmatrix}. \tag{1}$$

Here the vector  $M^{ave}$  corresponds to all measurements and the vector  $B^{ave}$  corresponds to all systematic error sources. The matrix  $A_M$  has a diagonal structure with  $N_M$  diagonal elements

$$A_M^{ii} = \sum_e \frac{w_{i,e}}{\Delta_{i,e}^2}. \tag{2}$$

The other matrices have the following elements

$$\begin{aligned} A_{SM}^{ij} &= - \sum_e \frac{\Gamma_{j,e}^i}{\Delta_{i,e}^2} w_{i,e}; \\ A_S^{ij} &= \delta_{ij} + \sum_e \sum_k \frac{\Gamma_{i,e}^k \Gamma_{j,e}^k}{\Delta_{k,e}^2} w_{k,e}; \\ C_M^i &= \sum_e \frac{\mu_e^i}{\Delta_{i,e}^2} w_{i,e}; \\ C_S^j &= - \sum_e \sum_k \frac{\mu_e^k \Gamma_{j,e}^k}{\Delta_{k,e}^2} w_{k,e}. \end{aligned} \tag{3}$$

Here  $\delta_{ij}$  is the standard Kronecker symbol. Note that the matrix  $A_{SM}$  has the dimension  $N_M \times N_S$  while the matrix  $A_S$  is quadratic with  $N_S \times N_S$  elements.

Using the method of the Schur complement, the solution is found as

$$\begin{aligned} A'_S &= A_S - (A_{SM})^T A_M^{-1} A_{SM}, \\ B^{ave} &= (A'_S)^{-1} (C_S - (A_{SM})^T A_M^{-1} C_M), \\ M^{ave} &= A_M^{-1} [C_M - A_{SM} B^{ave}]. \end{aligned} \tag{4}$$

Given the components of the vector  $B^{ave}$ ,  $\beta_{j,ave} = \alpha_{j,ave}/\Delta\alpha_j$ , the solution for  $\mu^{i,ave}$  can be written in explicit form

$$\mu^{i,ave} = \frac{\sum_e [(\mu_e^i + \sum_j \Gamma_{j,e}^i \beta_{j,ave}) \frac{w_{i,e}}{\Delta_{i,e}^2}]}{\sum_e \frac{w_{i,e}}{\Delta_{i,e}^2}}. \tag{5}$$

The uncorrelated uncertainty squared is determined by the inverse of the elements of the diagonal matrix  $A_M$

$$\Delta_{i,ave}^2 = \frac{1}{\sum_e \frac{w_{i,e}}{\Delta_{i,e}^2}}. \tag{6}$$

Similarly, the contributions from statistical and systematic uncertainties can be calculated

$$\begin{aligned} \Delta_{i,ave,stat}^2 &= \Delta_{i,ave}^4 \sum_e \frac{w_{i,e}}{\Delta_{i,e}^4} \Delta_{i,e,stat}^2, \\ \Delta_{i,ave,unc}^2 &= \Delta_{i,ave}^4 \sum_e \frac{w_{i,e}}{\Delta_{i,e}^4} \Delta_{i,e,unc}^2. \end{aligned} \tag{7}$$

Equations (5) and (6) reproduce the standard formula for a statistically weighted average of several uncorrelated measurements when all shifts of the systematic error sources are set to zero.

The non-diagonal nature of the matrix  $A'_S$  expresses the fact that the original sources of the systematic uncertainties are correlated with each other after averaging. The matrix  $A'_S$  can be decomposed to re-express (27) in terms of diagonalised systematic error sources

$$DD = UA'_S U^{-1}, \quad \Gamma_{ave} = A_{SM} A_M^{-1} D^{-1} U^{-1}. \tag{8}$$

Here  $U$  is an orthogonal matrix composed of the eigenvectors of  $A'_S$ ,  $D$  is a diagonal matrix with corresponding square roots of eigenvalues as diagonal elements and  $\Gamma_{ave}$  represents the sensitivity of the average result to these new sources. Its elements are the  $\Gamma_j^{i,ave}$  in (30).

**References**

1. E.D. Bloom et al., Phys. Rev. Lett. **23**, 930 (1969)
2. D.J. Fox et al., Phys. Rev. Lett. **33**, 1504 (1974)
3. I. Abt et al. (H1 Collaboration), Nucl. Phys. B **407**, 515 (1993)
4. M. Derrick et al. (ZEUS Collaboration), Phys. Lett. B **316**, 412 (1993)
5. C. Adloff et al. (H1 Collaboration), Eur. Phys. J. C **30**, 1 (2003). [hep-ex/0304003](#)
6. S. Chekanov et al. (ZEUS Collaboration), Phys. Rev. D **67**, 012007 (2003). [hep-ex/0208023](#)
7. J. Pumplin et al., J. High Energy Phys. **0207**, 012 (2002). [hep-ph/0201195](#)
8. S. Alekhin, Phys. Rev. D **68**, 014002 (2003). [hep-ph/0211096](#)
9. V.N. Gribov, L.N. Lipatov, Sov. J. Nucl. Phys. **15**, 438 (1972)
10. V.N. Gribov, L.N. Lipatov, Sov. J. Nucl. Phys. **15**, 675 (1972)
11. L.N. Lipatov, Sov. J. Nucl. Phys. **20**, 94 (1975)
12. Y.L. Dokshitzer, Sov. Phys. JETP **46**, 641 (1977)
13. G. Altarelli, G. Parisi, Nucl. Phys. B **126**, 298 (1977)
14. E.A. Kuraev, L.N. Lipatov, V.S. Fadin, Sov. Phys. JETP **44**, 443 (1976)
15. E.A. Kuraev, L.N. Lipatov, V.S. Fadin, Sov. Phys. JETP **45**, 199 (1977)
16. I.I. Balitsky, L.N. Lipatov, Sov. J. Nucl. Phys. **28**, 822 (1978)
17. M. Ciafaloni, Nucl. Phys. B **296**, 49 (1988)
18. S. Catani, F. Fiorani, G. Marchesini, Phys. Lett. B **234**, 339 (1990)

19. S. Catani, F. Fiorani, G. Marchesini, Nucl. Phys. B **336**, 18 (1990)
20. G. Marchesini, Nucl. Phys. B **445**, 49 (1995). [hep-ph/9412327](#)
21. L.V. Gribov, E.M. Levin, M.G. Ryskin, Phys. Rep. **100**, 1 (1983)
22. A.H. Mueller, J.-W. Qiu, Nucl. Phys. B **268**, 427 (1986)
23. I. Balitsky, Nucl. Phys. B **463**, 99 (1996). [hep-ph/9509348](#)
24. Y.V. Kovchegov, Phys. Rev. D **60**, 034008 (1999). [hep-ph/9901281](#)
25. M. Braun, Eur. Phys. J. C **16**, 337 (2000). [hep-ph/0001268](#)
26. E. Iancu, A. Leonidov, L.D. McLerran, Nucl. Phys. A **692**, 583 (2001). [hep-ph/0011241](#)
27. J. Bartels, L.N. Lipatov, G.P. Vacca, Nucl. Phys. B **706**, 391 (2005). [hep-ph/0404110](#)
28. J. Bartels, K. Kutak, Eur. Phys. J. C **53**, 533 (2008). [0710.3060](#)
29. S. Donnachie, G. Dosch, O. Nachtmann, P. Landshoff, *Pomeron Physics and QCD*, Camb. Monogr. Part. Phys. Nucl. Phys. Cosmol., vol. 19 (2002). ISBN 052178039X
30. N.N. Nikolaev, B.G. Zakharov, Z. Phys. C **49**, 607 (1991)
31. B.L. Ioffe, Phys. Lett. B **30**, 123 (1969)
32. V.N. Gribov, Sov. Phys. JETP **30**, 709 (1970)
33. T. Laštovička, Eur. Phys. J. C **24**, 529 (2002). [hep-ph/0203260](#)
34. G. Altarelli, G. Martinelli, Phys. Lett. B **76**, 89 (1978)
35. C. Adloff et al. (H1 Collaboration), Nucl. Phys. B **497**, 3 (1997). [hep-ex/9703012](#)
36. T. Ahmed et al. (H1 Collaboration), Z. Phys. C **66**, 529 (1995)
37. C. Adloff et al. (H1 Collaboration), Eur. Phys. J. C **21**, 33 (2001). [hep-ex/0012053](#)
38. J. Breitweg et al. (ZEUS Collaboration), Phys. Lett. B **487**, 53 (2000). [hep-ex/0005018](#)
39. S. Chekanov et al. (ZEUS Collaboration), Eur. Phys. J. C **21**, 443 (2001). [hep-ex/0105090](#)
40. S. Aid et al. (H1 Collaboration), Z. Phys. C **69**, 27 (1995). [hep-ex/9509001](#)
41. E. Gotsman, E.M. Levin, U. Maor, Eur. Phys. J. C **5**, 303 (1998). [hep-ph/9708275](#)
42. K. Golec-Biernat, M. Wüsthoff, Phys. Rev. D **59**, 014017 (1999). [hep-ph/9807513](#)
43. J.R. Forshaw, G. Kerley, G. Shaw, Phys. Rev. D **60**, 074012 (1999). [hep-ph/9903341](#)
44. J. Bartels, K. Golec-Biernat, H. Kowalski, Phys. Rev. D **66**, 014001 (2002). [hep-ph/0203258](#)
45. E. Iancu, K. Itakura, S. Munier, Phys. Lett. B **590**, 199 (2004). [hep-ph/0310338](#)
46. H. Kowalski, L. Motyka, G. Watt, Phys. Rev. D **74**, 074016 (2006). [hep-ph/0606272](#)
47. A. Blondel, F. Jacquet, in *Proc. ep Facility for Europe, Amsterdam 1979* (DESY 79/48, 1979)
48. U. Bassler, G. Bernardi, Nucl. Instrum. Methods A **361**, 197 (1995). [hep-ex/9412004](#)
49. H. Abramowicz, A. Levy, [hep-ph/9712415](#) (1997)
50. I. Abt et al. (H1 Collaboration), Nucl. Instrum. Methods A **386**, 310 (1997)
51. I. Abt et al. (H1 Collaboration), Nucl. Instrum. Methods A **386**, 348 (1997)
52. R.D. Appuhn et al., H1 backward upgrade with a SPACAL calorimeter: The Hadronic section (DESY, 96-013, 1996)
53. T. Nicholls et al. (H1 SpaCal Group), Nucl. Instrum. Methods A **374**, 149 (1996)
54. R.D. Appuhn et al. (H1 SpaCal Group), Nucl. Instrum. Methods A **382**, 395 (1996)
55. R.D. Appuhn et al. (H1 SpaCal Group), Nucl. Instrum. Methods A **386**, 397 (1997)
56. D. Pitzl et al., Nucl. Instrum. Methods A **454**, 334 (2000). [hep-ex/0002044](#)
57. B. Andrieu et al. (H1 Calorimeter Group), Nucl. Instrum. Methods A **336**, 460 (1993)
58. B. Andrieu et al. (H1 Calorimeter Group), Nucl. Instrum. Methods A **336**, 499 (1993)
59. H. Henschel, R. Lahmann, Nucl. Instrum. Methods A **453**, 93 (2000)
60. W. Eick, et al., Nucl. Instrum. Methods A **386**, 81 (1997)
61. R. Horisberger, D. Pitzl, Nucl. Instrum. Methods A **326**, 92 (1993)
62. W.J. Haynes et al., Nucl. Instrum. Methods A **403**, 313 (1998)
63. B. Schwab, Doctoral thesis, Ruprecht-Karls-Universität Heidelberg, 1996. <http://www-h1.desy.de/psfiles/theses/h1th-236.ps>
64. V. Karimaki, HU-SEFT-1991-10. Helsinki University, 1991
65. S. Glazov, Doctoral thesis, Humboldt-Universität zu Berlin, 1998. DESY-THESIS-1998-005
66. G.A. Schuler, H. Spiesberger, in *Proc. of the Workshop on HERA Physics*, vol. 3, ed. by W. Buchmüller, G. Ingelman (DESY, Hamburg, 1992), p. 1419. DJANGO 1.4
67. A. Kwiatkowski, H. Spiesberger, H.-J. Moehring, Comput. Phys. Commun. **69**, 155 (1992)
68. G. Gustafson, U. Petterson, Nucl. Phys. B **306**, 746 (1988)
69. B. Andersson et al., Z. Phys. C **43**, 625 (1989)
70. L. Lönnblad Comput. Phys. Commun. **71**, 15 (1992), ARIADNE 4.1
71. A. Mücke et al., Comput. Phys. Commun. **124**, 290 (2000). [astro-ph/9903478](#)
72. T. Sjostrand, Comput. Phys. Commun. **82**, 74 (1994), JETSET 7.4
73. R. Engel, Z. Phys. C **66**, 203 (1995)
74. R. Engel, J. Ranft, Phys. Rev. D **54**, 4244 (1996). PHOJET 1.6. [hep-ph/9509373](#)
75. A. Capella et al., Phys. Rep. **236**, 227 (1994)
76. A. Arbuzov et al., Comput. Phys. Commun. **94**, 128 (1996). HECTOR 1.0. [hep-ph/9511434](#)
77. R. Brun et al., GEANT3 User's Guide, CERN, 1987. CERN-DD/EE 84-01
78. G. Grindhammer, M. Rudowicz, S. Peters, Nucl. Instrum. Methods A **290**, 469 (1990)
79. H. Fesefeldt, *The Simulation of Hadronic Showers—Physics and Applications* (RWTH, Aachen, 1985). PITHA 85/02
80. D. Eckstein, Doctoral thesis, Humboldt-Universität zu Berlin, 2002. DESY-THESIS-2002-008
81. T. Laštovička, Doctoral thesis, Humboldt-Universität zu Berlin, 2004. DESY-THESIS-2004-016
82. A. Vargas, Doctoral thesis, Universität Dortmund, 2006. <http://www-h1.desy.de/psfiles/theses/h1th-453.pdf>
83. O. Behrendt, Doctoral thesis, Universität Dortmund, 2006. <http://www-h1.desy.de/psfiles/theses/h1th-452.pdf>
84. V. Blobel, C. Kleinwort, [hep-ex/0208021](#) (2002)
85. V. Lendermann, Doctoral thesis, Universität Dortmund, 2001. DESY-THESIS-2002-004
86. A. Aktas et al. (H1 Collaboration), Phys. Lett. B **598**, 159 (2004)
87. A. Glazov, AIP Conf. Proc. **792**, 237 (2005)
88. C. Adloff et al. (H1 Collaboration), Phys. Lett. B **520**, 183 (2001). [hep-ex/0108035](#)
89. F.D. Aaron et al. (H1 Collaboration), Phys. Lett. B **665**, 139 (2008). [0805.2809](#)
90. J. Bartels, K. Golec-Biernat, K. Peters, Eur. Phys. J. C **17**, 121 (2000). [hep-ph/0003042](#)